

VOLUME 6 ISSUE 1 FEBRUARY 2021



# IJEG

International Journal of Engineering and Geosciences



e-ISSN 2548-0960

## **EDITOR IN CHIEF**

*Prof. Dr. Murat YAKAR*  
Mersin University Engineering Faculty  
Turkey

## **CO-EDITORS**

*Dr. Osman ORHAN*  
Mersin University Engineering Faculty  
Turkey

*Prof. Dr. Ekrem TUŞAT*  
Konya Technical University  
Faculty of Engineering and Natural Sciences  
Turkey

*Prof. Dr. Songnian Li,*  
Ryerson University  
Faculty of Engineering and Architectural Science,  
Canada

*Dr. Ali ULVI*  
Mersin University Engineering Faculty  
Turkey

## **ADVISORY BOARD**

*Prof. Dr. Orhan ALTAN*  
Honorary Member of ISPRS, ICSU EB Member  
Turkey

*Prof. Dr. Naser El SHAMY*  
The University of Calgary Department of Geomatics Engineering,  
Canada

*Prof. Dr. Armin GRUEN*  
ETH Zurich University  
Switzerland

*Prof. Dr. Ferruh YILDIZ*  
Selcuk University Engineering Faculty  
Turkey

*Prof. Dr. Artu ELLMANN*  
Tallinn University of Technology Faculty of Civil Engineering  
Estonia

## **EDITORIAL BOARD**

*Prof. Dr. Alper YILMAZ*  
Environmental and Geodetic Engineering, The Ohio State University,  
USA

*Prof. Dr. Chryssy Potsiou*  
National Technical University of Athens-Rural and Surveying Engineering,  
Greece

*Prof. Dr. Cengiz ALYILMAZ*  
Ataturk University Kazim Karabekir Faculty of Education  
Turkey

*Prof. Dr. Dieter FRITSCH*  
University of Stuttgart Institute for Photogrammetry  
Germany

*Prof. Dr. Edward H. WAITHAKA*  
Jomo Kenyatta University of Agriculture & Technology  
Kenya

*Prof.Dr. Halil SEZEN*  
Environmental and Geodetic Engineering, The Ohio State University  
USA

*Prof.Dr. Huiming TANG*  
China University of Geoscience..., Faculty of Engineering,  
China

*Prof.Dr. Laramie Vance POTTS*  
New Jersey Institute of Technology, Department of Engineering Technology  
USA

*Prof.Dr. Lia MATCHAVARIANI*  
Iv.Javakhishvili Tbilisi State University Faculty of Geography  
Georgia

*Prof.Dr. Məqsəd Hüseyn QOCAMANOV*  
Baku State University Faculty of Geography  
Azerbaijan

*Prof.Dr. Muzaffer KAHVECI*  
Selcuk University Faculty of Engineering  
Turkey

*Prof.Dr. Nikolai PATYKA*  
National University of Life and Environmental Sciences of Ukraine  
Ukraine

*Prof.Dr. Petros PATIAS*  
The Aristotle University of Thessaloniki, Faculty of Rural & Surveying Engineering  
Greece

*Prof.Dr. Pierre GRUSSENMEYER*  
National Institute of Applied Science, Department of civil engineering and surveying  
France

*Prof.Dr. Rey-Jer You*  
National Cheng Kung University, Tainan · Department of Geomatics  
China

*Prof.Dr. Xiaoli DING*  
The Hong Kong Polytechnic University, Faculty of Construction and Environment  
Hong Kong

*Assoc.Prof.Dr. Elena SUKHACHEVA*  
Saint Petersburg State University Institute of Earth Sciences  
Russia

*Assoc.Prof.Dr. Semra ALYILMAZ*  
Ataturk University Kazim Karabekir Faculty of Education  
Turkey

*Assoc.Prof.Dr. Fariz MIKAILSOY*  
Igdir University Faculty of Agriculture  
Turkey

*Assoc.Prof.Dr. Lena HALOUNOVA*  
Czech Technical University Faculty of Civil Engineering  
Czech Republic

*Assoc.Prof.Dr. Medzida MULIC*  
University of Sarajevo Faculty of Civil Engineering  
Bosnia and Herzegovina

*Assoc.Prof.Dr. Michael Ajide OYINLOYE*  
Federal University of Technology, Akure (FUTA)  
Nigeria

*Assoc.Prof.Dr. Mohd Zulkifli bin MOHD YUNUS*  
Universiti Teknologi Malaysia, Faculty of Civil Engineering  
Malaysia

*Assoc.Prof.Dr. Syed Amer MAHMOOD*  
University of the Punjab, Department of Space Science  
Pakistan

*Assist. Prof. Dr. Yelda TURKAN*  
Oregon State University,  
USA

*Dr. G. Sanka N. PERERA*  
Sabaragamuwa University Faculty of Geomatics  
Sri Lanka

*Dr. Hsiu-Wen CHANG*  
National Cheng Kung University, Department of Geomatics  
Taiwan

### **The International Journal of Engineering and Geosciences (IJEG)**

The International Journal of Engineering and Geosciences (IJEG) is a tri-annually published journal. The journal includes a wide scope of information on scientific and technical advances in the geomatics sciences. The International Journal of Engineering and Geosciences aims to publish pure and applied research in geomatics engineering and technologies. IJEG is a double peer-reviewed (blind) OPEN ACCESS JOURNAL that publishes professional level research articles and subject reviews exclusively in English. It allows authors to submit articles online and track his or her progress via its web interface. All manuscripts will undergo a refereeing process; acceptance for publication is based on at least two positive reviews. The journal publishes research and review papers, professional communication, and technical notes. IJEG does not charge for any article submissions or for processing.

CORRESPONDENCE ADDRESS

Journal Contact: [engineeringandgeoscience@gmail.com](mailto:engineeringandgeoscience@gmail.com)

# CONTENTS

*Volume 6 - Issue 1*

## ARTICLES

** INVESTIGATION OF THE EFFECT OF URBANIZATION ON LAND SURFACE TEMPERATURE EXAMPLE OF BURSA Beyzanur Yamak, ZekeriyaYagci, Burhan Baha Bilgilioglu, Resul Comert	1
** AN INVESTIGATION OF THE PERFORMANCES OF POLARIMETRIC TARGET DECOMPOSITIONS USING GB-SAR IMAGING Sevket Demirci, Caner Ozdemir	9
** AUTOMATIC EXTRACTION OF TREES BY USING MULTIPLE RETURN PROPERTIES OF THE LiDAR POINT CLOUD Samed Ozdemir, Zeynep Akbulut, Fevzi Karsli, Hayrettin Acar	20
** DEVELOPING A MOBILE GIS APPLICATION RELATED TO THE COLLECTION OF LAND DATA IN SOIL MAPPING STUDIES Fatih Iscan, Erkan Guler	27
** INTELLIGENT MAPPING OF IRRIGATED AREAS FROM LANDSAT 8 IMAGES USING TRANSFER LEARNING Zouhair Benbahria , Imane Sebari, Hicham Hajji, Mohamed Faouzi Smiej	41
** AN INVESTIGATION OF URBAN DEVELOPMENT WITH GEOGRAPHICAL INFORMATION SYSTEMS: 100-YEAR CHANGE OF SIVAS CITY, TURKEY Sefa Sari, Tarık Türk	51



## Investigation of the effect of urbanization on land surface temperature example of Bursa

Beyzanur Yamak <sup>\*1</sup>, Zekeriya Yagci <sup>1</sup>, Burhan Baha Bilgilioglu <sup>1,2</sup>, Resul Comert <sup>1</sup>

<sup>1</sup>Gumushane University, Faculty of Engineering and Natural Sciences, Geomatics Engineering Department, Gümüşhane, Turkey

<sup>2</sup>Istanbul Technical University, Faculty of Civil Engineering, Geomatics Engineering Department, Istanbul, Turkey

### Keywords

Land surface temperature (LST)  
Urban heat island (UHI)  
Normalized differential  
vegetation index (NDVI)  
Bursa

### ABSTRACT

Today, industrialization and urbanization in large cities cause an increase in the surfaces covered with man-made objects such as concrete and asphalt. The expansion of urban areas and increase in the using materials with high heat storage properties, directly affect the Land Surface Temperature (LST), which shows an increase in the sensible temperature of the region. LST is directly connected to the natural green vegetation of the land and varies widely in large urban areas, these differences related to the temperature is defined as the 'urban heat island'. In this study, it was investigated the temporal variation of land surface temperature due to urbanization. Bursa, which is considered as a study area, has shown a rapid population increase since 1990 and a rapid increase in the number of buildings with the impact of urbanization and industrialisation. To determine the effect of this urbanization and industrialisation on land surface temperature, temporal change analysis of the surface temperature in the Bursa was observed with Landsat satellite images of 1988, 1998, 2008 and 2018. From produced maps, it was observed that the amount of green vegetation in urban areas decreased and as a consequence of this decrease, the surface temperature increased in the urban areas.

## 1. INTRODUCTION

The population of urban areas has uncontrolled rising due to education, health and housing opportunities. Rapid population growth causes changes in land use characteristics and unplanned urbanization in cities. Especially with the increase of residential and industrial areas, the green zone required for the human is decreasing. Urbanization and industrialization increase the heat adversely affects the water cycle in the atmosphere and climate change (Yuksel and Yilmaz 2008). Also, with the increase of urban needs, vegetation and forestry areas decrease, the absorption of solar radiation increases and affect the regional climate. These results lead to the formation of urban heat island (UHI) (Morabito et al. 2016). UHI is the case where a surface area in the city is warmer than in other regions. This climatic discrepancy in cities can be defined as urban heat island (Yuksel and Yilmaz 2008).

Radiation that reaches the Earth is one of the most important factors affecting UHI formation. Different land use/land cover properties in rural and urban areas cause significant temperature differences in these areas. Reflection of the incoming energy from the ground is not the same in rural and urban areas. Because in rural areas, the reflected energy is reflected without any physical obstacles, while in urban areas it is kept between high buildings and occurred significant back-time delays (Cicek and Dogan 2006). It is very important to identify these areas in order to reduce the impact of the heat islands in cities and to make sustainable plans for the future. With the developing satellite technologies, it is possible to determine the urban heat islands with the thermal sensors on the satellite (Orhan et al. 2019). Today many studies are investigating the relationship between urban land use/land cover and urban heat island (Herbei et al. 2012; Patil et al. 2018; Khorrami et al. 2019; Kuşak and Küçükali 2019). When these studies were

### \* Corresponding Author

(beyzanryamak@gmail.com) ORCID ID 0000 – 0002 – 5091 – 9571  
(zekeriya.yagci@gmail.com) ORCID ID 0000 – 0002 – 9800– 8056  
(bilgilioglu16@itu.edu.tr) ORCID ID 0000 – 0001 – 6950 – 4336  
(rcomert@gumushane.edu.tr) ORCID ID 0000– 0003– 0125 – 4646

### Cite this article

Yamak B, Yagci Z, Bilgilioglu B B & Comert R (2021) Investigation of the effect of urbanization on land surface temperature example of Bursa. International Journal of Engineering and Geosciences, 6(1), 1-8.

examined, it was observed that generally similar results were obtained. Especially in urban areas, the UHI value was high but in vegetation and water areas, the UHI value was low (Sekertekin et al. 2016).

In this study, the relationship of urban heat island formation and the urban growth of Bursa city center between 1988 and 2018 was investigated. Within this scope, the land use/land cover (LU/LC) and land surface temperature (LST) maps of the city center have been produced for 10 years periods since 1988. By comparing the generated maps, the relationship between LST and terrain LU/LC was demonstrated. Besides, the Normalized Difference Vegetation Index (NDVI) and Normalized Difference Built-up Index (NDBI) were produced to determine the relationship between LST and urban area and vegetation. Also, the correlation between these indexes and LST was determined.

## 2. STUDY AREA

The main area of the study includes Osmangazi, Yildirim and Nilufer district centers of Bursa. The study area consists of the city center and its surrounding area covering a total area of 630.72 km<sup>2</sup> because urban heat islands are particularly come into existence in urban centers, structured areas and industrially developed areas. The location and boundaries of the study area are shown in Figure 1. Bursa province is a middle scale city when 755.504 people live in there in 1965, then the number increased to 2.150.571 in 2000 and 2.994.521 in 2018 in proportion with the industry. Thus Bursa became the fourth province with the highest population density in Turkey (TUIK 2019). In this respect, it is a very important issue to examine the effects and results of the urbanization of Bursa.

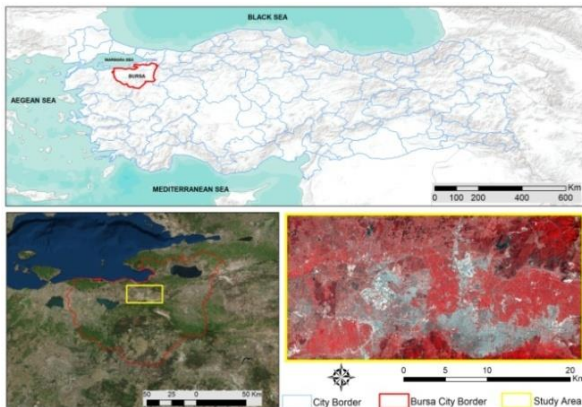


**Figure 1.** Study area: yellow polygon indicates the application area

## 3. DATA and METHODS

### 3.1. Data

Landsat satellite community has been used for the extraction of information about the earth surface for many years. In this study, landsat satellite images were used to create LU/LC and land surface

temperature maps (Aghayev 2018; Orhan et al. 2019). Landsat 5 satellite images for 1988, 1998, 2008 Landsat 8 satellite images for 2018 were obtained from the US Geological Survey (USGS) 'Earth Explorer' website (<https://earthexplorer.usgs.gov/>). When selecting satellite images, we preferred cloudless images considering atmospheric conditions and seasonal effects (Table 1). Spectral bands were used for LU/LC classification and relevant spectral bands and thermal bands were used when generating LST maps. The band characteristics of the satellite images are given in Table 2.

**Table 1.** Details of Landsat satellite images

Number	Satellite	Sensor	Date Acquired
1	Landsat 5	TM	25.07.1988
2	Landsat 5	TM	06.08.1998
3	Landsat 5	TM	17.08.2008
4	Landsat 8	OLI & TIRS	13.08.2018

**Table 2.** Bands and spatial resolutions of satellites images used in analysis

Bands	Resolution (meters)
Blue	30
Green	30
Red	30
Near Infrared	30
SWIR 1	30
SWIR 2	30
Thermal*	30

\*The thermal bands were re-sampled to 30 meters.

### 3.2. Method

The methodology applied within the scope of this study is given below as sub-headings.

#### 3.2.1 Production of land use / Land cover (LU/LC)

Supervised classification method was performed for LU/LC determination. To classify the satellite images of the study area for the specified years, 5 classes were defined as urbanized area, vegetated area, water, cropland and bare soil. According to the defined classes, training data were collected and the classification process was performed using the Maximum Likelihood algorithm. The accuracy of supervised classification results was calculated by the error matrix for each year using 350 control points.

#### 3.2.2 Normalized difference built-up index (NDBI)

Normalized Difference Built-up Index (NDBI) was calculated using Middle Infra-Red (MIR) and Near Infra-Red (NIR) bands spectral reflectance value for determining the settlements of the study area (Herbei et al. 2012). Also, this index has been applied for determining the relationship of the settlement area with the land surface temperature.

Normalized Difference Built-up Index is calculated by dividing the difference of MIR and NIR bands with the sum of bands (Eq. (1)).

$$NDBI = \frac{MIR - NIR}{MIR + NIR} \quad (1)$$

### 3.2.3 Calculation of land surface temperature (LST)

Many algorithms have been used for the purpose of extracting LST from satellite imagery. Some of algorithms is the SplitWindow Algorithm (SWA), Single Channel Algorithm (SCA), Mono-Window Algorithm (MWA) and the Radiative Transfer Equation (RTE) (Ndossi and Advan 2016). In this study, Mono-Window Algorithm (MWA) was used to extract LST (Qin et al. 2001; Wang et al. 2015). The process flow of the methodology is given in Figure 2 (Avdan and Jovanovska 2016). In the study, the thermal band was used to determine the brightness temperature, red and NIR bands were used to calculate Normalized Differential Vegetation Index (NDVI).

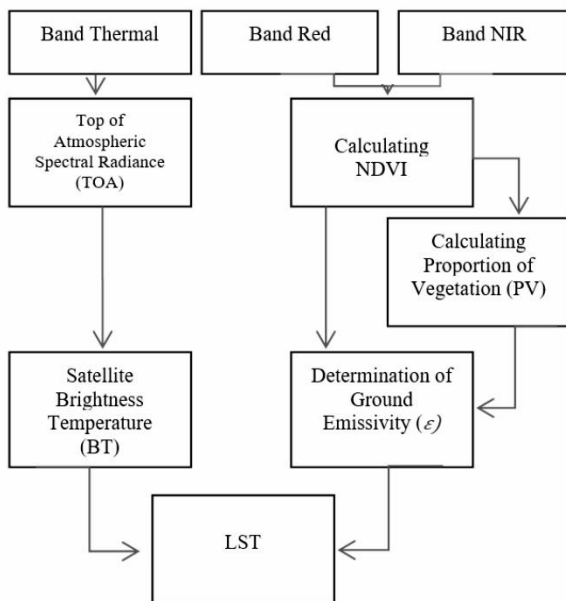


**Figure 2.** Flow chart of the Land Surface Temperature (LST) algorithm

The processing steps and formulas of the LST calculation are as follows.

#### 3.2.3.1 Top of atmospheric spectral radiance calculation (TOA)

The first step of the algorithm is to input the thermal band and calculated spectral radiance formulated from the official site of USGS (Eq.(2)) (Akher and Chattopadhyay 2017).

$$TOA (L) = M_L * Q_{cal} + A_L \quad (2)$$

$M_L$ : Band specific multiplication rescaling factor

$Q_{cal}$ : Radiant value corresponding to the thermal tape

$A_L$ : Resizing factor

#### 3.2.3.2 Conversion of radiance to at-sensor temperature (BT)

Digital numbers (DN) refer to reflection values. After these reflection values are converted to radiance values, the spectral radiance is converted to brightness temperature (BT) using the thermal constants provided in the metadata file of the thermal band data (Eq.(3)) (Akher and Chattopadhyay 2017). Applied values for the images were given in Table 3.

Kelvin transformation is performed to obtain the results in Celsius (approx -273.15).

$$BT = \frac{K_2}{(\ln(K_1 / "TOA") + 1)} - 273.15 \quad (3)$$

where  $K_1$  and  $K_2$ : Band-specific thermal conversion constants.

**Table 3.** Applied metadata values for different sensors

Metadata	Landsat 5 (Band 6)	Landsat 8 (Band 10)
$K_1$	607.76	774.8853
$K_2$	1260.56	1321.0789
$M_L$	0.055375	0.0003342
$A_L$	1.18243	0.1

#### 3.2.3.3 Normalized differential vegetation index (NDVI)

The calculation of the normalized vegetation index was used both in the calculation of emissivity in the LST and the comparison of the existing vegetation areas between the LST (Eq.(4)) (Avdan and Jovanovska 2016).

$$NDVI = \frac{NIR - Red}{NIR + Red} \quad (4)$$

#### 3.2.3.4 Calculating the proportion of vegetation (Pv)

The vegetation rate can be calculated according to the following formula (Eq.(5))(Akher and Chattopadhyay 2017).

$$P_v = ((NDVI - NDVI_{min}) / (NDVI_{max} - NDVI_{min}))^2 \quad (5)$$

#### 3.2.3.5 Calculating land surface emissivity (ε)

Land surface emissivity ( $\epsilon$ ) must be determined to calculate LST (Eq.(6)). Surface emissivity is defined as the relative ability of the surface of a material to emit energy by radiation. The emissivity is also expressed as the ratio of the energy emitted by a given material to the energy emitted by a black body at the same temperature. In short, it is the

efficiency of transmitting thermal energy from the surface to the atmosphere (Jimenez- Munoz et al. 2006).

$$\epsilon_{\lambda} = \epsilon_{v\lambda} + \epsilon_{s\lambda} (1 - P_v) + C_{\lambda} \quad (6)$$

where,  $\epsilon_{v\lambda}$ : Plant emissivity value;  $\epsilon_{s\lambda}$ : Soil emissivity value

### 3.2.3.6 Calculation of Land Surface Temperature (LST)

Equation 7 and Equation 8 are applied to obtain the land surface temperature map (Akher and Chattopadhyay 2017).

$$LST = \frac{BT}{\{1 + [\lambda BT / \rho] * \ln(\epsilon)\}} \quad (7)$$

$$\rho = h \frac{c}{\sigma} = 1.438 \times 10^{-2} \text{ m K} \quad (8)$$

$\sigma$ : Boltzmann constant ( $1.38 \times 10^{-23}$  J/K)

$h$ : Planck's constant ( $6.626 \times 10^{-34}$  Js)

$c$ : Velocity of light ( $2.998 \times 10^8$  m/s)

### 3.2.4 Calculation of urban heat island effect

The following formula (Eq. 9) was used to analyse urban heat island changes in the study area (Ma et al. 2010):

$$UHI: \mu + \frac{\sigma}{2} \quad (9)$$

In the formula,  $\mu$  is the average LST value of the study area and  $\sigma$  is the standard deviation of LST.

## 4. RESULTS and DISCUSSION

### 4.1 LU/LC Classification

The result maps of the classification process for Bursa city center are shown below (Figure 3). For the accuracy assessment of the produced maps, 350 reference points were placed in the study area and the overall accuracy of the classified data was determined for each period. The overall accuracy values of the classified images of 1988, 1998, 2008, 2018 were 85%, 83%, 80% and 86% respectively.

According to the classification results, it has been observed that the urban areas have increased substantially. According to the spatial comparison made after the classification, the urban area in 1988 is 74.18 km<sup>2</sup>; in 2018, it increased approximately 270% and reached 202.44 km<sup>2</sup>. This rise in the urban area increase of the land surface temperature and affect the expansion of the urban heat island.

### 4.2 Land Surface Temperature (LST)

The thermal infrared bands of the Landsat 5 and Landsat 8 satellites were converted to spectral radiance and used as a source for the calculation of the brightness temperature of the surface

temperature land. Following process steps in Figure 2, land surface temperature maps of the study area were produced for the determined years (Figure 4).

Land surface temperature values vary between 20-34 °C in 1988, 17-32 °C in 1998, 22-46 °C in 2008 and 19-42 °C in 2018. In 1988 and 2018, the maximum temperature difference is 8 °C and the minimum temperature difference is 1 °C.

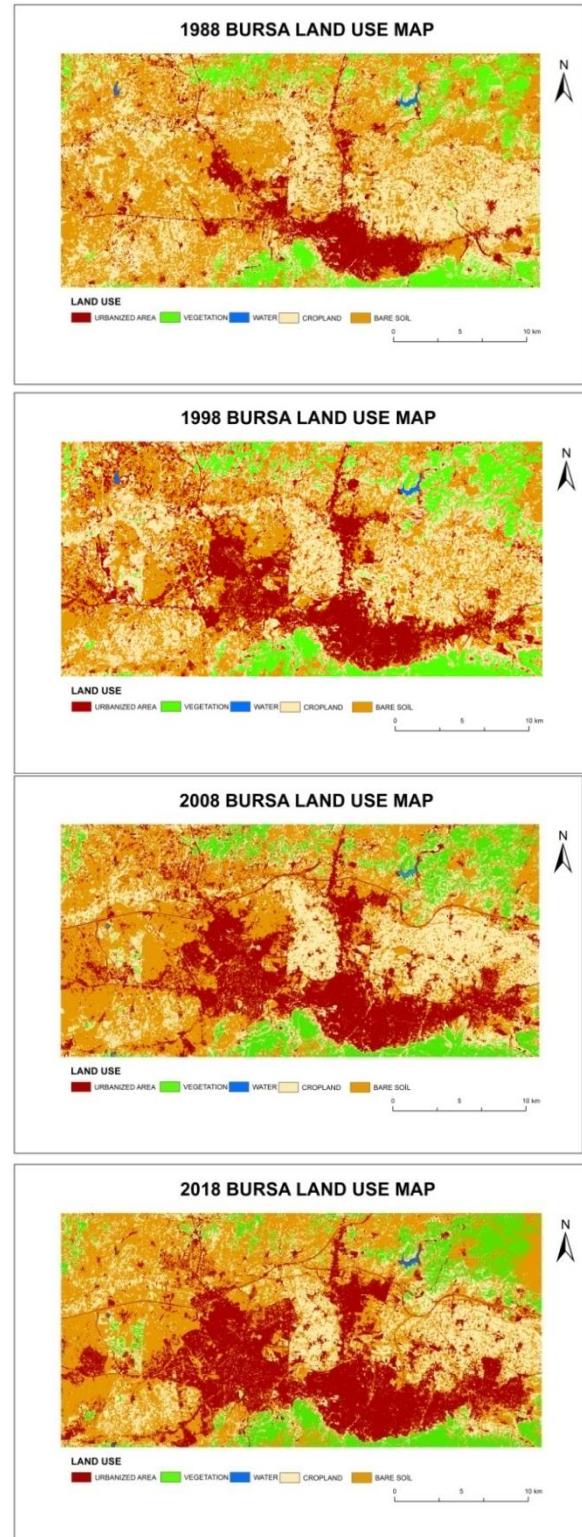


**Figure 3.** LU/LC maps obtained as a result of classification process; (a): 1988, (b): 1998, (c): 2008, (d): 2018

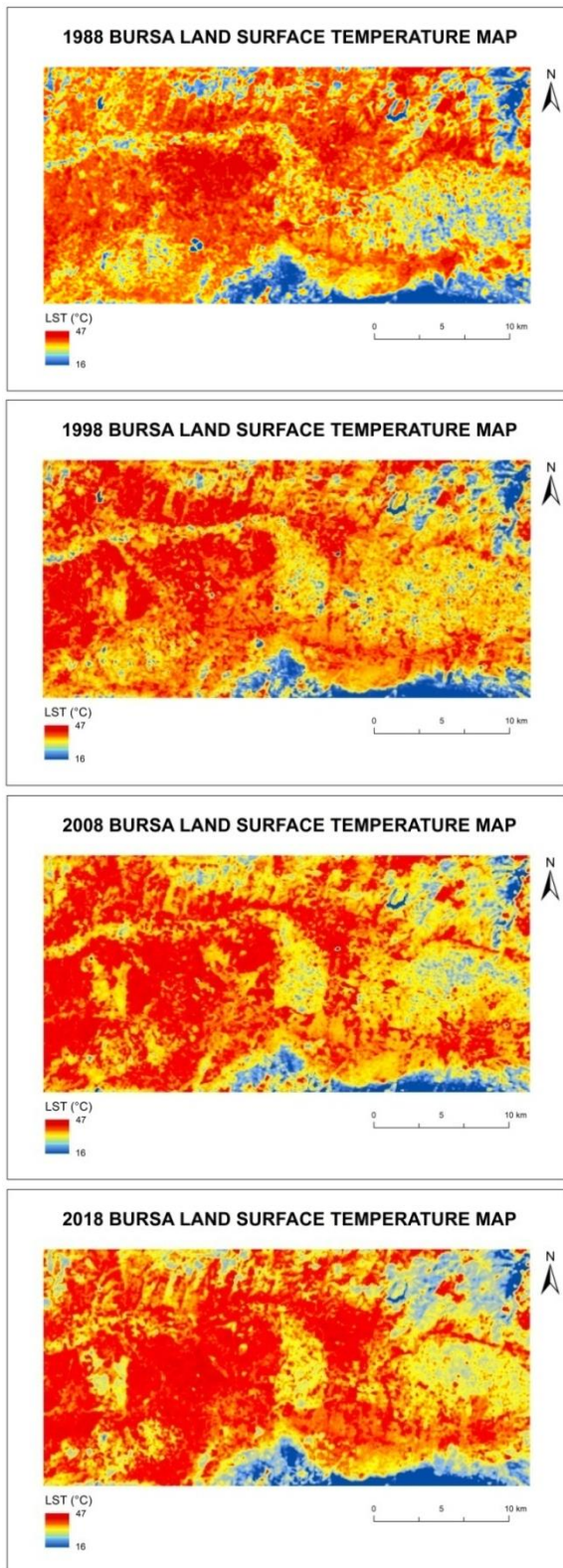


**Figure 4.** LST maps produced by years (a): 1988, (b): 1998, (c): 2008, (d): 2018

To evaluate the accuracy of land surface temperature maps, the nearest temperature data to satellite image acquisition time were obtained at the meteorological station of Bursa, Kestel, Nilufer and

Yildirim from General Directorate of Meteorology (Table 4). Temperature differences are given as absolute values in Table 4. Root mean square errors that were calculated from temperature difference for the land surface temperature maps were calculated as 0.7 (°C) in 1988, 2.7 (°C) in 1998, 2.9 (°C) in 2008 and 0.83 (°C) in 2018.

#### 4.3 Relationship between Land Surface Temperature and Land Cover/Land Use

When the relationship between land surface temperature maps and LU/LC classes is examined, it is observed that the highest value of land surface temperature is in urban areas and the lowest value is in wetlands (Figure 5). Additionally, it was found that the surface temperature of the study area changed depending on the land cover and land use classes.

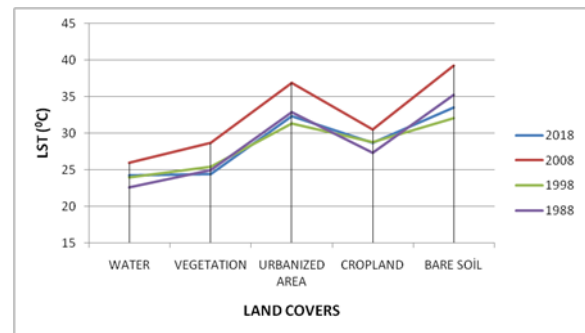


**Figure 5.** Relationship between land surface temperature and land use

#### 4.4 Relationship of Land Surface Temperature with NDBI and NDVI

Correlation analysis was used to investigate the relationship between land surface temperature, NDBI and NDVI. Correlation analysis was applied using randomly selected 100 points to Landsat 5 and Landsat 8 satellite images sensed on 1988, 1998, 2008 and 2018. Figure 6 and Figure 7 clearly show the correlation between land surface temperature with NDBI and NDVI. As a result, NDBI values were higher in areas with high land surface temperatures and NDVI values were higher in areas with lower land surface temperatures. Based on these results, the correlation analysis showed that the surface temperature of the land was in a high negative correlation with NDVI and high positive NDBI. The correlation coefficient between land surface temperature and NDBI was calculated as 0.75648 in 1988, 0.75579 in 1998, 0.82532 in 2008 and 0.78215 in 2018. The correlation coefficient between land surface temperature and NDVI was calculated as -0.72241 in 1988, -0.75256 in 1998, -0.78061 in 2008 and -0.70042 in 2018.

**Table 4.** Difference between land surface temperatures and station temperature values

Station Name	Station Temperature (°C)	Temperature Values Obtained from LST Maps (°C)	Temperature Difference (1°C)	Date
BURSA	33.8	34.5	0.7	25.07.1988/11.00
BURSA	35.2	32.5	2.7	06.08.1998/11.00
BURSA	36.3	39.2	2.9	17.08.2008/12.00
BURSA	31	32	1	13.08.2018/12.00
KESTEL	32.8	32.6	0.2	13.08.2018/12.00
NİLÜFER	31	32	1	13.08.2018/12.00
YILDIRIM	32.8	32.6	0.2	13.08.2018/12.00

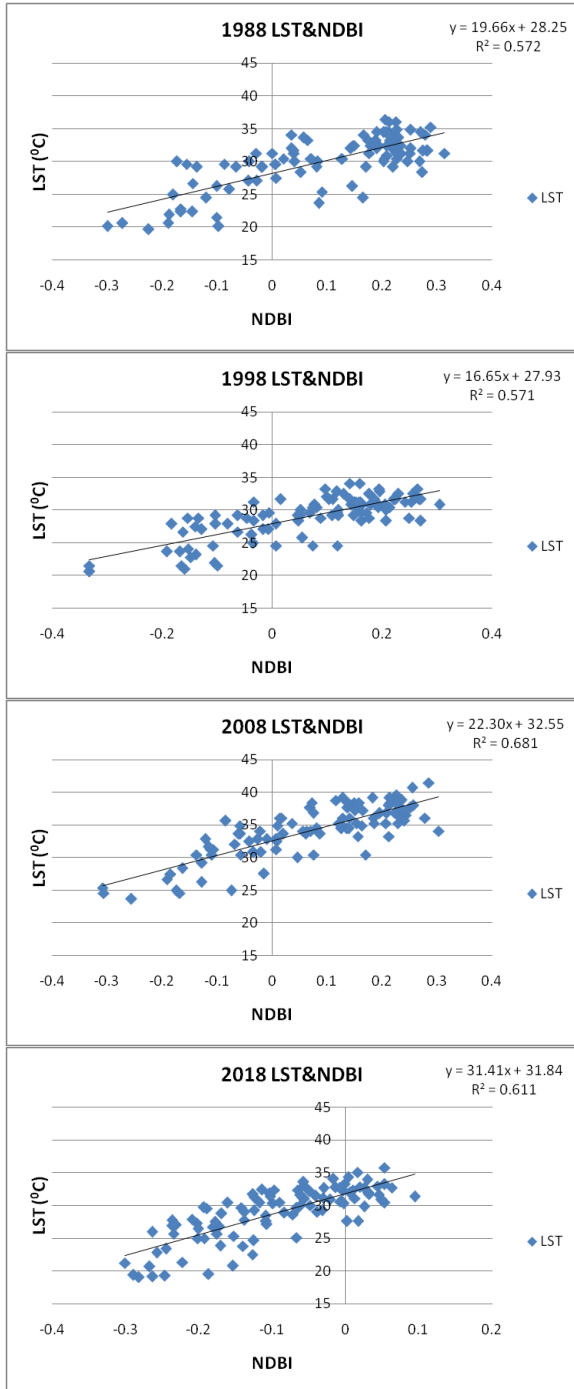


**Figure 6.** The relationship between LST and NDBI for the determined years (a): 1988, (b): 1998, (c): 2008, (d): 2018

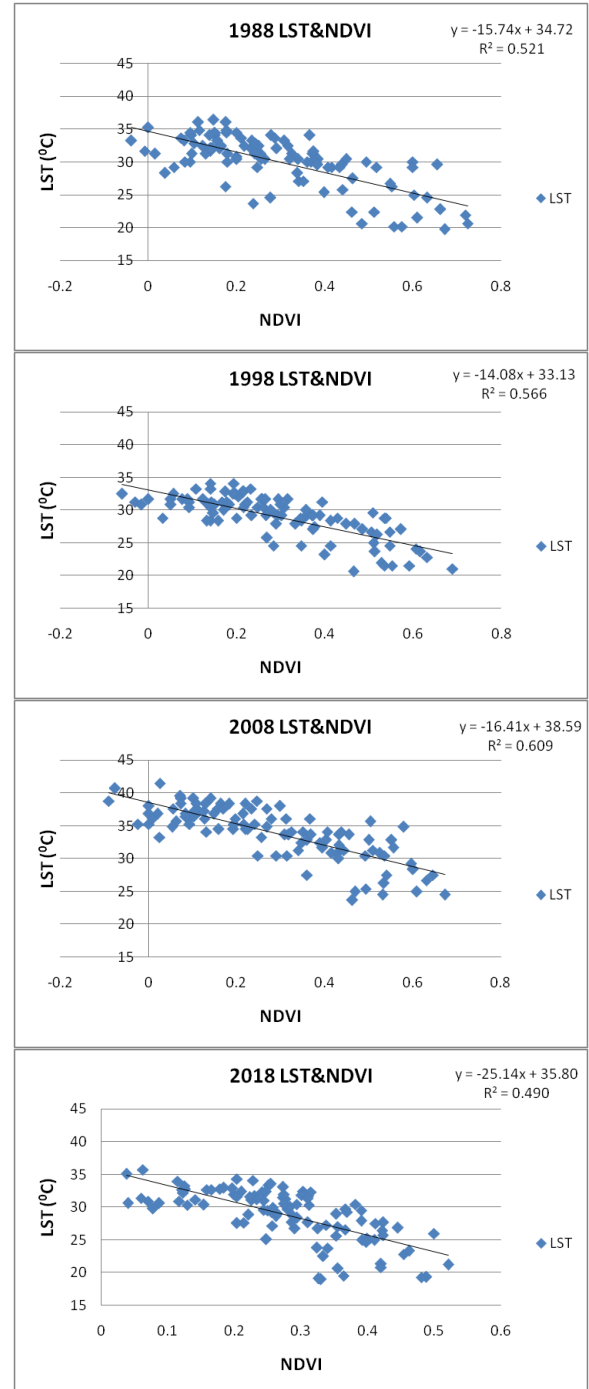


**Figure 7.** The relationship between LST and NDVI for the determined years; (a): 1988, (b): 1998, (c): 2008, (d): 2018

#### 4.5 Calculation of Urban Heat Island Effect

The urban heat island effect of 1988, 1998, 2008 and 2018 was calculated for the study area (Figure 8). When the results are examined, it is determined that the urban heat island effect occurred mostly in the residential and industrial zone. At the same time, these areas where land surface temperature is high. The lowest urban heat island effect was observed in wetland and vegetation areas. Land surface temperature is low in these regions. Based on these observations, it can be said that the density of the residential area and the industrial area increased the surface temperature of the land and revealed the urban heat island concept.

#### 5. CONCLUSION

Landsat 8 and Landsat 5 satellite images were used for long term observation of the study area. Near infra-red, red and thermal bands of Landsat images were used for the extraction of LST maps. Also, LU/LC maps were produced divided into 5 classes as urbanized area, vegetated area, water, cropland and bare soil to make a general evaluation of the study area. When LST maps were evaluated, it was observed that high-temperature values were observed in industrial areas, bare soil and reinforced concrete structures. Besides, low-temperature values have been found in plant areas, forest areas and wetlands. Also, when NDVI and NDBI are compared with LST, it is seen that there is a high positive correlation with NDBI and a high negative correlation with NDVI. It was determined that plant-covered areas could reduce the urban heat island effect because when urban density increased, the urban heat island effect increased. In some areas, there is an average temperature difference of 5-6 °C between the city center and the plant-covered areas, also up to 10 °C temperature differences were observed in urban areas which are changed by the density of urbanization. The reason for this difference is that urban heat island formation reflects its unique climate and temperature value. To reduce the impact of urban heat island effect, reducing the land surface temperature value is an indirect solution. The use of analytical analyses and spatial regression models is important for UHI research and provides a basis for better urban planning. As a result, rising temperatures in urban areas adversely affect human health, social, economic and environmental conditions. Due to low LST values are detected in areas where NDVI is high, conservation and increase of vegetation areas in urban centers can reduce urban heat island effect.

#### Acknowledgments

This article has been selected from the papers presented at the TUFUAB-2019 (10. Turkey National Photogrammetry and Remote Sensing Technical Symposium).

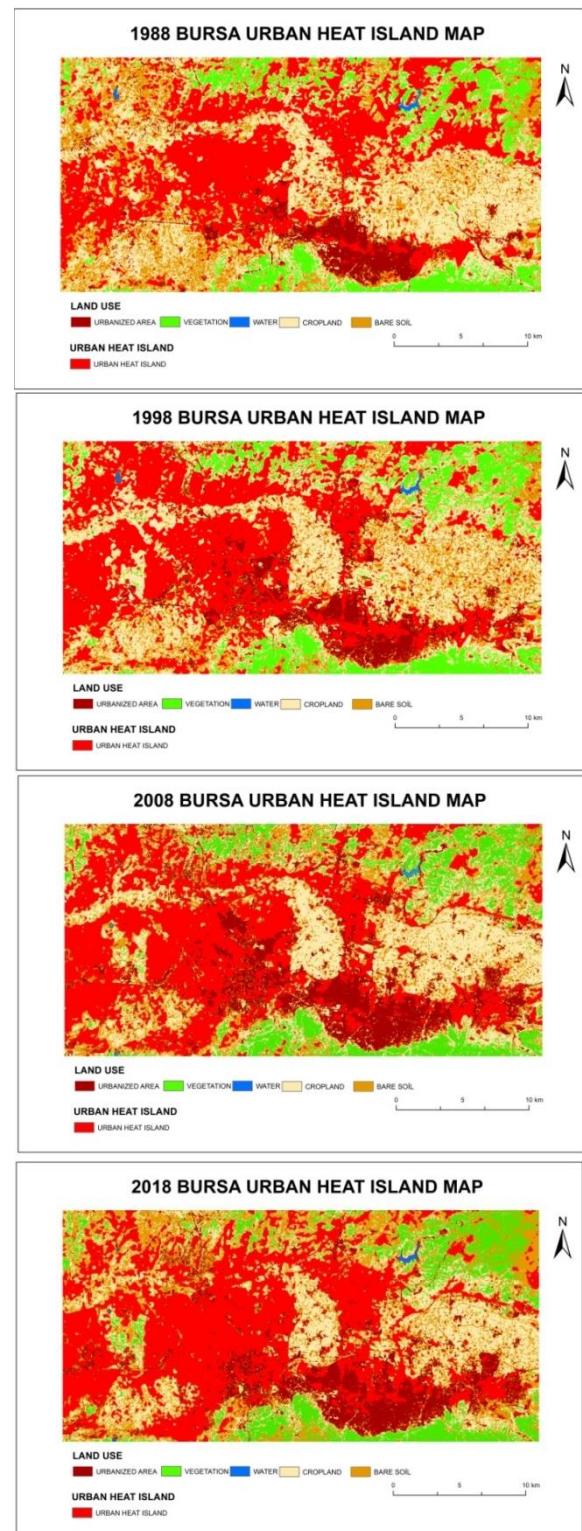


**Figure 8.** Urban heat islands for the determined years: (a): 1988, (b): 1998, (c): 2008, (d): 2018

#### REFERENCES

- Aghayev A (2018). Determining of different inundated land use in Salyan Plain during 2010 the Kura River flood through GIS and remote sensing tools. *International Journal of Engineering and Geosciences*, 3(3), 80-86. DOI: 10.26833/ijeg.412348

- Akher S K & Chattopadhyay S (2017). Impact of urbanization on land surface temperature-A case study of Kolkata New Town. *The International Journal of Engineering Science*, 6(1), 71-81. DOI: 10.9790/1813-0601027181
- Avdan U & Jovanovska G (2016). Algorithm for automated mapping of land surface temperature using LANDSAT 8 Satellite data. *Journal of Sensors*. Doi: 10.1155/2016/1480307
- Cicek I & Dogan U (2006). Detection of urban heat island in Ankara, Turkey. *NuovoCimentodellaSocietaItaliana di Fisica. C, Geophysics and Space Physics*; ISSN 1124-1896; Worldcat; v. 29C (4), 3 (1), 399-409.
- Herbei M V, Dragomir L O & Oncia S (2012). Using satellite images LANDSAT TM for calculating normalized difference indexes for the landscape of Parang Mountains. *RevCAD Journal of Geodesy and Cadastre*, 13, 158-167.
- Jimenez-Munoz J C, Sobrino J A, Gillespie A, Sabol D & Gustafson W T (2006). Improved land surface emissivities over agricultural areas using ASTER NDVI. *Remote Sensing of Environment*, 103(4), 474-487.
- Khorrami B, Gunduz O, Patel N, Ghoulane S & Najjar M (2019). Land surface temperature anomalies in response to changes in forest cover. *International Journal of Engineering and Geosciences*, 4 (3), 149-156. DOI: 10.26833/ijeg.549944
- Kuşak L & Küçükali U F (2019). Outlier detection of land surface temperature: Küçükçekmece Region. *International Journal of Engineering and Geosciences*, 4 (1), 1-7. DOI: 10.26833/ijeg.404426
- Ma Y, Kuang Y & Huang N (2010). Coupling urbanization analyses for studying urban thermal environment and its interplay with biophysical parameters based on TM/ETM+ imagery. *International Journal of Applied Earth Observation and Geoinformation*, 12(2), 110-118. Doi: 10.1016/j.jag.2009.12.002
- Morabito M, Crisci A, Messeri A, Orlandini, Raschi A., Maracchi G & Munafo M (2016). The impact of built-up surfaces on land surface temperatures in Italian urban areas. *Science of the Total Environment*, 551-552, 317-326.
- Ndossi M I & Avdan U (2016). Application of open source coding technologies in the production of land surface temperature (LST) maps from Landsat: a PyQGIS plugin. *Remote sensing*, 8(5), 413. Doi:10.3390/rs8050413
- Orhan O, Dadaser-Celik F & Ekercin S. (2019). Investigating land surface temperature changes using Landsat-5 data and real-time infrared thermometer measurements at Konya Closed Basin in Turkey. *International Journal of Engineering and Geosciences*, 4(1), 16-27. DOI: 10.26833/ijeg.417151
- Patil A S, Panhalkar S S, Bagwan S & Bansode S. (2018). Impact of land use land cover change on land surface temperature using Geoinformatics Techniques. *International Journal of Research and Analytical Reviews (IJRAR)*, 5(4), 550-559.
- Qin Z, Karnieli A & Berliner P (2001). A mono-window algorithm for retrieving land surface temperature from Landsat TM data and its application to the Israel-Egypt border region. *International Journal of Remote Sensing*, 22(18), 3719-3746.
- Sekertekin A, Kutoglu S H & Kaya S (2016). Evaluation of spatio-temporal variability in land surface temperature: A case study of Zonguldak, Turkey. *Environmental Monitoring and Assessment*, 188(1), 30. Doi: 10.1007/s10661-015-5032-2
- TUİK: URL:  
<http://www.tuik.gov.tr/PreHaberBultenleri.do?sessionid=8FJDhyCWQJ1zgWYwrsLL31DbCfbhxRc56SbHK4rTJR1MrBSTvSC1116535747?id=27587> Accessed date: 12 December 2019
- Wang F, Qin Z, Song C, Tu L, Karnieli A & Zhao S (2015). An improved mono-window algorithm for land surface temperature retrieval from Landsat 8 thermal infrared sensor data. *Remote sensing*, 7(4), 4268-4289. Doi: 10.3390/rs70404268
- Yüksel Ü D & Yilmaz O (2008). A study on determining and evaluating summertime urban heat islands in Ankara at regional and local scale utilizing remote sensing and meteorological data. *Journal of the Faculty of Engineering and Architecture of Gazi University*, 23(4), 937-952. (In Turkish)



© Author(s) 2021.

This work is distributed under <https://creativecommons.org/licenses/by-sa/4.0/>



## An investigation of the performances of polarimetric target decompositions using GB-SAR imaging

Şevket Demirci\*<sup>1</sup>, Caner Özdemir<sup>1</sup>

<sup>1</sup>Mersin University, Engineering Faculty, Electrical and Electronics Engineering Department, Mersin, Turkey

### Keywords

SAR  
Polarimetric SAR  
Ground-based SAR  
Target decomposition

### ABSTRACT

Ground-based synthetic aperture radar (GB-SAR) systems are mostly utilized to be practical practices in improved understanding of the complex mechanism of microwave backscattering. They also provide complementary information on evaluating the validity of the polarimetric analysis of air-borne or satellite-borne SAR applications. This study investigates some capabilities of polarimetric L-band GB-SAR imaging by testing its performance against a typical terrain and various kinds of manmade targets. Trihedral corner reflectors are also included in the analyses because of their importance in data calibration. Polarimetric backscattering signatures of different targets are analyzed in terms of qualitative assessment of amplitude images and identification and classification of scattering mechanisms through target decomposition techniques. The findings of these analyses and detailed discussions are presented. Specifically, the entropy/mean-alpha ( $(H/\bar{\alpha})$ ) classification results are shown to be capable of clearly identifying the dominant scattering mechanisms occurring within the investigated scene.

## 1. INTRODUCTION

Active remote sensors supply their own illumination energy to acquire information about the Earth's surface. RADAR (Radio Detection and Ranging) and LIDAR (Light Detection and Ranging) are two typical examples of active sensors which have been widely used in a variety of environmental applications, such as classification of urban and forest areas and production of digital elevation models (DEM) (Moreira et al. 2013; Sevgen 2019; Yilmaz and Uysal 2017; Yilmaz and Erdogan 2018).

Among the radar sensors, synthetic aperture radar (SAR) constitutes one of the essential technologies for microwave remote sensing. Basically, it uses the motion of the platform on which the radar is mounted to generate an image of the Earth's surface. SAR systems operating on aircrafts provide monitoring of large-scale areas with relatively high resolution imagery (Ouchi 2013). On the other hand, ground-based SAR (GB-SAR) systems are better suited for inspection of small-scale areas with a better resolution capability than that of air-

based systems (Cho et al. 2006; Gonzalez et al. 2008; Lee et al. 2007; Lee et al. 2014; Lee et al. 2016; Penner and Long 2017; Cuenca 2017). Interferometric and polarimetric practices can also be effectively exploited within these systems to aid target identification. This type of ground-truth information could also be helpful for research and validation studies. Herein, we carry out such a study by focusing on the assessment of polarimetric GB-SAR imaging of a typical land scene.

In polarimetric SAR (PolSAR), data are collected with different combinations of transmit-receive polarizations. It has well known that radar polarimetry is sensitive to the structure of the target being observed. In principle, the target's reflectivity, shape, symmetric structures can be extracted from the reflected wave's polarization change data. This is, however, a difficult task, since the interaction between microwaves and random media is usually complex, varying as a function of numerous factors such as wavelength, viewing geometry, polarization of the transmitted wave as well as target attributes including roughness, shape, size and orientation. In

\* Corresponding Author

<sup>\*</sup>(sdemirci@mersin.edu.tr) ORCID ID 0000 – 0002 – 3020 – 7067  
(cozdemir@mersin.edu.tr) ORCID ID 0000 – 0003 – 2615 – 4203

Cite this article

Demirci S & Ozdemir C (2021). An investigation of the performances of polarimetric target decompositions using GB-SAR imaging. International Journal of Engineering and Geosciences, 6(1), 09-19

past decades, a great amount of effort has been made to overcome this limitation (Lee and Pottier 2009; van Zyl and Kim 2011; Cloude 2010). This has given rise to development of various polarimetric SAR (PolSAR) systems and methods which have proven the usefulness of PolSAR in various applications especially in image classification and contrast enhancement. Among these, for GB-SAR specific applications, the reader is referred to (Pipia 2009; Pipia et al. 2013; Iglesias et al. 2015a; Iglesias et al. 2015b; Baffelli et al. 2018; Brown et al. 2003; Lim and Koo 2008; Penner and Long 2017; Zhou 2003; Zhou 2004; Minh et al. 2014; Kang et al. 2009; Xing et al. 2013). Nevertheless, it is still an experimental technique in quantitative retrieval of target parameters.

In this context, polarimetric target decomposition techniques remain the most promising tools (Chen et al. 2018). Such techniques decompose the measured backscattering matrix into a combination of simpler (canonical) responses. This provides a better identification of scattering mechanisms and thus an easier interpretation of targets' structural characteristics. To date, many successful applications of several decomposition approaches have been reported for a variety of SAR data (Lee and Pottier 2009; Chen et al. 2018; Chen et al. 2014; Alberga et al. 2004; Cloude 2010). However, it is also obvious that the wide variability and complexity in target scenes and environmental conditions may lead to misinterpretation if ground-truth information is not available. Consequently, the performances of these techniques might be anecdotal, with good performance under certain conditions and poor performance elsewhere.

In our previous study (Demirci et al. 2019), we therefore, tested the potential of the two of the most widely used techniques namely; Pauli and eigenvalue/eigenvector decomposition with data from a fully-controlled GB-SAR experiment. In this paper, we extend this analysis by including Krogager decomposition (Krogager 1990) and Freeman-Durden decomposition (Freeman and Durden 1998), so that comparisons can be made. Also, a different land scene consisting of a series of trees is employed because of the growing interest in vegetation monitoring (Penner and Long 2017; Zhou 2004; Minh et al. 2014; Albinet et al. 2012). The other investigated targets are; a gazebo with waste containers and metal sticks and corner reflectors added on the surface. The relevant images of the mentioned decompositions at L-band are analyzed to recognize the targets' identifiable features over image pixels. The findings of these analyses and discussions are presented.

## 2. THEORY

### 2.1 GB-SAR Imaging Methodology

Fig. 1 shows the geometry for a typical two-dimensional (2D) monostatic GB-SAR imaging.

Monostatic means the same antenna is used as the transmitter (TX) and receiver (RX). The antenna is elevated to a certain height  $h$  and inclined with an incidence angle  $\beta'$  from the vertical direction. With transmission of a single pulse, the scene is illuminated with a range of local incidence angles  $\beta$ . The radar records part of the scattered wave directed backwards to the RX antenna. The process is then repeated by measuring the returned signals at  $\Delta x$  azimuth steps and covering a total synthetic aperture length  $L_{synt}$ . If the reflectivity of the desired imaging area is denoted by  $D(x, y)$ , then  $y$  is normal to the scanning path corresponding to ground-range axis, while  $x$  is parallel to the platform path corresponding to azimuth or cross-range dimension. The range or slant-range  $r$  refers to the true distance from antenna to target.

Assuming a stepped-frequency continuous wave (SFCW) transmission, the received signal at a specific scanning point contains the frequency response of the scene, sampled at discrete frequency steps  $\Delta f$  within a bandwidth  $B$ . The inverse Fourier transform (IFT) of this signal provides the range profile of the illuminated area for that particular viewpoint. The range profile represents a projection of a three-dimensional (3D) target into a one-dimensional (1D) function. Obtaining an estimate of target reflectivity (i.e., imaging) can then be thought as a process of inverting this transform. For such near-field data collections, plane-wave illumination of the entire target is usually not satisfied, thus an image reconstruction algorithm that accounts for the wavefront curvature effects is needed to obtain a focused image.

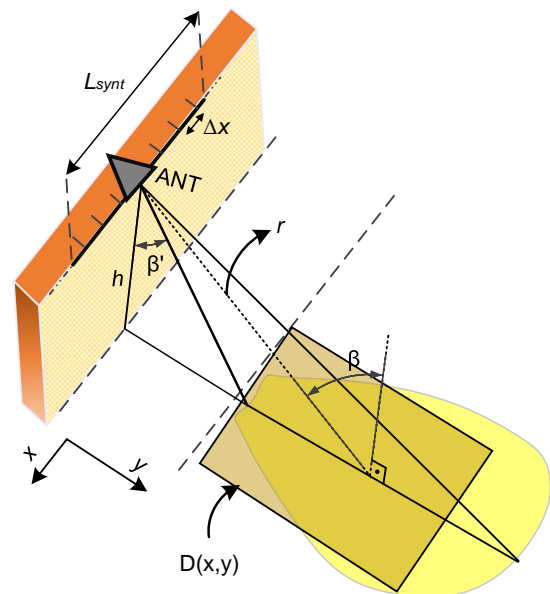


**Figure 1.** The geometry for 2D monostatic GB-SAR imaging

### 2.2 PolSAR Data Characteristics

PolSAR systems operate mostly in linear horizontal (H) and vertical (V) polarization basis,

measuring up to four channels, i.e.,  $HH$ ,  $VV$ ,  $HV$  and  $VH$  with the first and second letters represent transmit and receive polarizations, respectively. The backscattering characteristics of a target can be completely described by a  $2 \times 2$  scattering (Sinclair) matrix  $[S]$

$$[S] = \begin{bmatrix} S_{HH} & S_{HV} \\ S_{VH} & S_{VV} \end{bmatrix} \quad (1)$$

where the elements are the complex scattering amplitudes measured by the corresponding channel of radar. The diagonal and off-diagonal elements are termed as co-pol and cross-pol channels, respectively. In monostatic radars,  $[S]$  becomes symmetric, i.e.,  $S_{HV} = S_{VH} = S_{XX}$  for targets that reciprocity property holds.

Each pixel in a focused SAR image retains this single complex dataset which is dependent only on the target parameters for a fixed viewing geometry and frequency. Many targets of interest in SAR imaging can be broadly categorized into two: deterministic (coherent) and distributed (incoherent). Deterministic targets lead to non-depolarizing scattering process that can well be described by a first-order descriptor, such as the  $[S]$  matrix. Distributed targets, on the other hand, normally give rise to either partially or completely depolarizing scattering process owing to presence of many randomly distributed point scatterers inside a resolution unit. In such cases, second order descriptors, such as coherency  $[T]$  and covariance  $[C]$  matrices are utilized to describe the scattering behavior of each pixel, together with a spatial averaging over adjacent pixels.

### 2.3 Target Decomposition Techniques

Polarimetric target decomposition techniques allow interpretation of the measured polarimetric radar data by separating it into basic (canonical) scattering mechanisms. There are numerous decomposition schemes which mainly fall into two types: coherent decomposition and incoherent decomposition. The former is based on the decomposition of  $[S]$  matrix whereas the latter is based on the decomposition of  $[T]$  or  $[C]$  matrices. Among the popular coherent decompositions are the Pauli decomposition (Lee and Pottier 2009) and the Krogager decomposition (Krogager 1990). As for the incoherent decomposition, it is further rendered into two classes: eigenvector/eigenvalue based decomposition (Cloude and Pottier 1996; Cloude and Pottier 1997) and model-based decomposition (Chen et. al. 2014). The first is based on the eigenvalue analysis of the  $[T]$  matrix and has the capability of incorporating the entire range of scattering mechanisms. The parameters, namely entropy ( $H$ ) and mean-alpha ( $\bar{\alpha}$ ) derived from this decomposition can also be utilized within unsupervised classification algorithms, like the well-known  $H/\bar{\alpha}$  classification (Cloude and Pottier 1997).

The second class of incoherent decomposition makes use of various scattering models to decompose the scattering power contained in  $[T]$  or  $[C]$  matrix. The most typical example is the Freeman-Durden decomposition (Freeman and Durden 1998) which is also the first developed model-based decomposition technique. For a detailed discussion of target decomposition principles and applications, the reader is referred to (Lee and Pottier 2009; Chen et al. 2018).

### 3. MEASUREMENT SETUP and TEST SCENE

To perform stripmap SAR measurements, we constructed a radar system and mounted it onto a wheel platform. The system consists of a vector network analyzer (VNA) that works as a SFCW radar between 0.3 GHz and 8.5 GHz, two Vivaldi type horn antennas in a quasi-monostatic arrangement, a 1 Watt RF amplifier and a computer with a MATLAB [The Mathworks] program that controls and synchronizes positioning and data capturing. The complex data measured for a single-sweep of VNA can be instantaneously imported into MATLAB for post-processing.

With the geometry depicted in Fig. 1, a field experiment was conducted. A terrain near a building in Mersin University was selected and the measurements were carried out on that said building's roof terrace at a height of 15 m above ground. Fig. 2 shows the picture of the investigated scene seen from the radar location. The scene was comprised of a soil surface partly covered with grasses and bushes, a series of trees, a paved road and a gazebo. We also added various metallic objects with different orientations onto surface to determine and validate canonical backscattering mechanisms. The zoomed-out views of these objects, namely; five trihedral corner reflectors (C1 to C5) and four metal sticks (T1 to T4) can be seen in the upper pictures of Fig. 2. C1 to C4 were of triangular type while C5 was of a square type. Trihedral C3 was put within trees and not optically visible throughout the synthetic aperture scan. As for the metal sticks, T1 was aligned horizontally while T2 vertically. The others T3 and T4 were oriented at about  $-45^\circ$  and  $45^\circ$  with respect to line-of-sight (LOS) direction, respectively.

The measurements were made for a frequency span of 1 to 3 GHz sampled at 801 points and a synthetic aperture length of  $L_{synt} = 30$  m sampled with  $\Delta x = 10$  cm steps. The TX and RX antennas were both inclined to have an elevation angle of  $81^\circ$  and operated in quasi-monostatic mode with a spatial separation of 30 cm between each other. In such quasi-monostatic backscattering measurements, reciprocity holds for most targets, whereby cross-pol terms are assumed to be equal, i.e.,  $S_{HV} = S_{VH}$ . Therefore, we collected data in three channels, i.e.,  $S_{HH}$ ,  $S_{VV}$  and  $S_{VH}$ . The following processing steps were taken in imaging: First, windowing with a Hanning smoothing function and a subsequent  $4 \times$  zero padding were applied to the

1D frequency-domain data measured for each sweep of VNA. Second, a 1D IFT was performed to obtain the corresponding range profiles. Finally, the resulted signals were focused via backprojection imaging algorithm, an explanation of which can be found in (Ozdemir et al. 2014) for a similar SAR geometry.

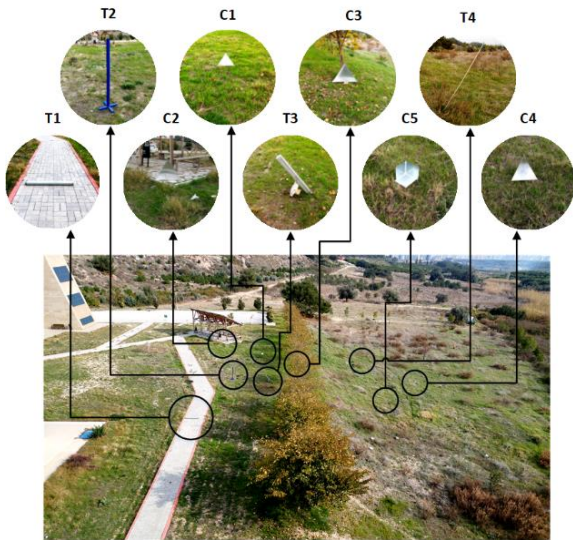


**Figure 2.** Picture of the scene seen from the radar location (down) and zoomed-out views of the manmade targets added on the scene (up)

## 4. RESULTS

### 4.1 Amplitude Images

Fig. 3 shows the reconstructed images in amplitude domain. Canonical objects are marked on the  $|S_{VV}|$  image with squares. Note that, the layout of the terrain and its different sections can be inferred from each image. Many comments can be derived. To begin with let's first consider the  $|S_{VH}|$  result. Theoretically, cross-pol scattering is mostly caused by natural media, complex manmade targets as well as oriented objects. The measured  $|S_{VH}|$  image manifests this fact, since the targets that have complex structures like the trees, bushes, gazebo as well as the tilted sticks T3 and T4 are seen to have cross-pol component because of volume scattering mechanism. Besides,  $VH$  scattering from the vertical cylinder T2, which is not expected, can be attributed to its complex-shaped base, which can be noticed from Fig. 2. Cross-pol amplitudes of the other objects are mostly low and not enough to produce a good contrast level.

Next, examining the co-pol signatures, we find it in the first place that all targets, either natural or manmade, are clearly displayed in each case, with  $|S_{HH}|$  amplitudes being slightly higher than those of  $|S_{VV}|$ . Manmade targets, as expected, show strong non-depolarizing scattering and thus are well localized. Even the trihedral C3 within trees can be detected thanks to the capability of L-band electromagnetic waves in penetrating through tree canopies. As for the terrain targets, co-pol reflection from trees are shown to have larger amplitudes

when compared to cross-pol case. This indicates dominance of odd or even-bounce scattering mechanisms produced from tree tops and trunk-ground interactions. The relatively larger grasses and bushes spread over the area also possess considerable co-pol scattering due to quasi-specular reflections. This is especially visible in  $|S_{HH}|$  image wherein various patches of vegetation can be identified.

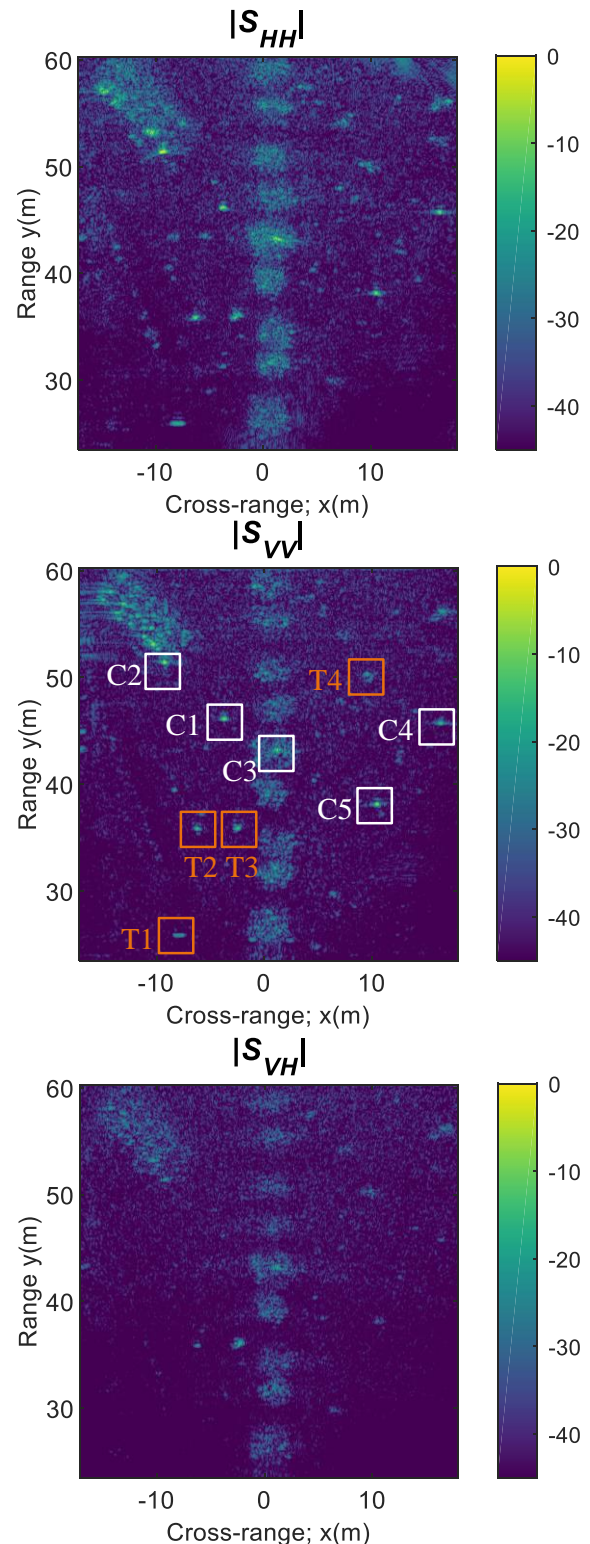


**Figure 3.** Amplitude images of the scattering matrix elements in a dB scale. Locations of the canonical objects are marked on the  $|S_{VV}|$  image

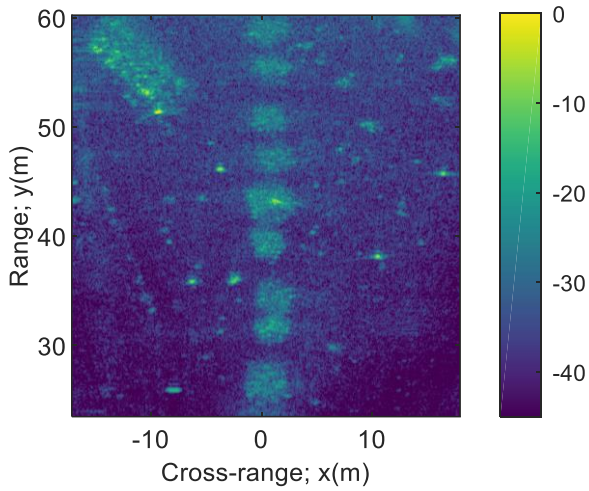


**Figure 4.** Total power image of the scattering matrix elements in a dB scale

For a power domain analysis, the total backscattered power (span) of  $[S]$  defined as

$$\text{span}([S]) = |S_{HH}|^2 + |S_{VV}|^2 + 2|S_{HV}|^2 \quad (2)$$

is calculated and imaged in Fig. 4. Scattering contributions in all channels are summed and thus a better visualization is achieved. All manmade objects including the hidden trihedral C3 and the scatters within the gazebo area are better pronounced as hot spots. Furthermore, various bushes and grasses on surface vegetation become more visible within this image.

#### 4.2 Pauli Decomposition

The direct use of  $S_{HH}$ ,  $S_{VV}$  and  $S_{VH}$  elements, as seen above, is not much able to distinguish between different types of scattering mechanisms, especially between odd- and even-bounce. To overcome this limitation, we utilized decomposition techniques. First, Pauli decomposition was applied by constructing:

$$k_1 = \frac{S_{HH}+S_{VV}}{\sqrt{2}}, k_2 = \frac{S_{HH}-S_{VV}}{\sqrt{2}}, k_3 = \sqrt{2}S_{HV} \quad (3)$$

components which correspond to the amount of contributions of odd-bounce, even-bounce and volume (or dihedral rotated  $45^\circ$ ) scatterings, respectively. The RGB color composite image was then formed by assigning  $|k_1|$ ,  $|k_2|$  and  $|k_3|$  as blue, red and green. Fig. 5 shows the resulted image. The following interpretations can be done by noting that scattering characteristics of a target are largely affected by its size, shape, pattern and orientation.

The ground cover is mainly represented in black due to specular reflections from smooth surfaces. Trees are shown to have mixture of reddish and greenish tones owing to dominant double-bounce and volumetric scatterings. As for the manmade targets, the rear part of the gazebo also exhibits complex scattering characteristics similar to those of trees. Note that  $VH$  (green) component is usually resulted from

complicated structures and targets that have azimuthal orientations relative to radar LOS, both of which hold for this target. The front section, however, has magenta and purple tones implying varying compositions of odd- and even-bounce that may be emerged from the pavement at the bottom, two waste containers, reflector C2 and gazebo's structure pattern (see optical image in Fig. 2).

The perceived color for the reflectors lying on low-density grasses (C1, C4 and C5) is violet. This indicates the presence of even-bounce return in addition to stronger odd-bounce return which can be explained by non-ideal ground conditions. The hidden TCR (C3) is seen to have all of the three scattering mechanisms. Furthermore, the TCR near the gazebo (C2), is in magenta, implying a strong double-bounce scattering, which can be attributed to the nearby step-like pavement. As for the metal sticks, the horizontal cylinder T1 is displayed as red, due to dihedral structure formed by the ground plane. The vertically aligned stick T2 shows a combination of odd and double-bounce scattering, while the T3 and T4 both show predominant volume scattering components because of their azimuthal orientation angles. The results, in general, demonstrate that Pauli components provide more information about the underlying scattering process when compared to raw elements of  $[S]$ .

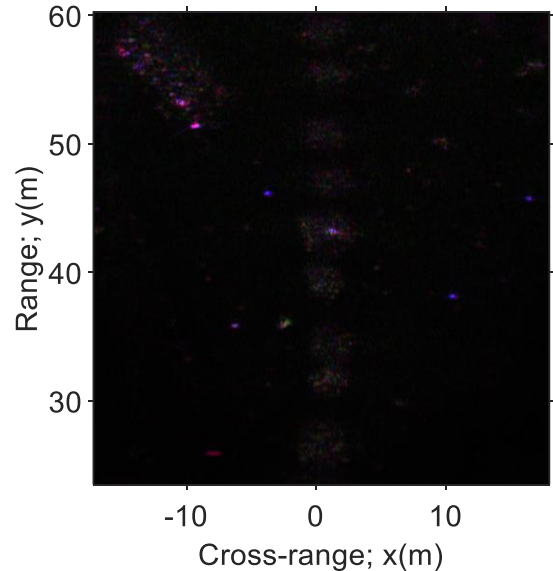


**Figure 5.** Color-coded composite image of the Pauli decomposition: blue,  $|k_1|$ ; red,  $|k_2|$ ; and green,  $|k_3|$

#### 4.3 Krogager Decomposition

Next, Krogager decomposition was utilized as a means of comparison with Pauli decomposition results. This approach, also called as the sphere, diplane, helix, (SDH) decomposition, coherently separates the symmetric  $[S]$  matrix into three fundamental elements such as a sphere (plate), a diplane (dihedral) and a helix. This representation of  $[S]$  in linear polarization basis can be written as (Krogager 1990)

$$[S] = e^{j\varphi} \{ e^{j\varphi_s} k_s [S]_s + k_D [S]_{D(\theta)} + k_H [S]_{H(\theta)} \} \quad (4)$$

where,  $\varphi$  is the absolute phase, phase  $\varphi_s$  is the displacement of sphere to dihedral and helix components,  $\theta$  is the orientation angle, and  $[S]_s$ ,  $[S]_{D(\theta)}$  and  $[S]_{H(\theta)}$  denote the scattering from a sphere, a diplane and a helix with the corresponding weights  $k_s$ ,  $k_D$  and  $k_H$ , respectively. The approach offers an orientation invariant decomposition, but with a disadvantage that the diplane and helix matrices are not independent. But, the sphere and diplane, also the diplane and helix matrices are independent. Noting that helix scattering can be generated by two or more dihedrals, the absence of helix component, therefore, could be an indicative of pure even-bounce scatterer.

Fig. 6 shows the resulted composite RGB image obtained by discarding the phase terms and assigning the amplitudes of  $k_s$ ,  $k_D$  and  $k_H$  as blue, red and green, respectively. The contributions of each of these scattering mechanisms are also presented individually in Fig. 7. We observe from these images that the scene has similar polarimetric scattering features with those of Pauli decomposition. For this case, green color in RGB image denotes helix scattering which appears typically in manmade structures or targets with complex shapes. The overall image is mostly dominated by reddish and blueish pixels, thereby implying a combination of odd- and even-bounce mechanisms. We also see that multiple-bounce returns from the gazebo and trees yield again a mixture of colors caused by their complex structures. The rear sections of the gazebo as well as the some tree sections show helix scattering denoting the presence of two or more even-bounce mechanisms within the resolution cells of these regions. Thus, compared to Pauli decomposition, pure even-bounce mechanisms can be more easily identified in Krogager decomposition by figuring out near red tones. In general, each of these coherent decompositions is shown to enable a simple and quite appropriate identification of elementary scattering mechanisms.

#### 4.4 Freeman-Durden Decomposition

We have used two techniques for the incoherent analysis our polarimetric SAR data; Freeman-Durden decomposition and eigenvalue/eigenvector decomposition. Each can be implemented through decomposition of the coherency matrix  $\langle [T] \rangle$ . For this reason, we first constructed the target scattering vector defined in Pauli basis as  $\vec{k}_p = 1/\sqrt{2} [S_{HH} + S_{VV}, S_{HH} - S_{VV}, 2S_{VH}]^T$ . The averaged coherency matrix  $\langle [T] \rangle$ , where  $\langle \dots \rangle$  stands for spatial averaging, was then obtained from the outer product of  $\vec{k}_p$ , followed by an averaging process over a  $5 \times 5$  window.

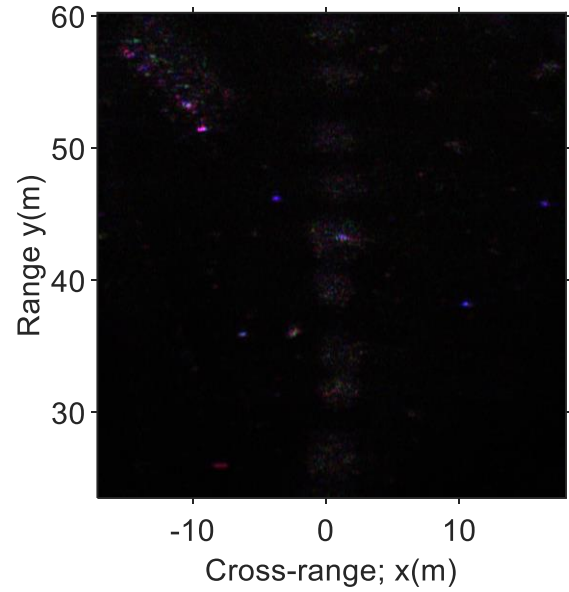


**Figure 6.** Color-coded composite image of the Krogager decomposition: blue,  $|k_s|$ ; red,  $|k_D|$ ; and green,  $|k_H|$ .

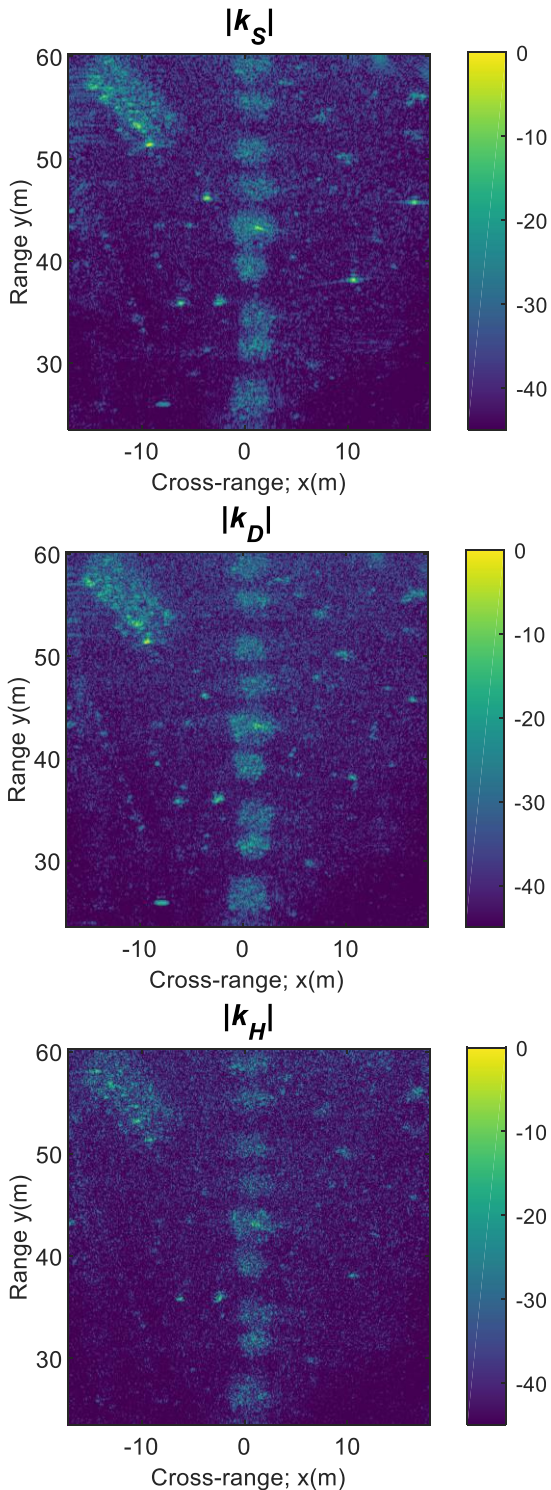
First, Freeman-Durden decomposition (Freeman and Durden 1998) was employed as an illustrative example of model-based decompositions. The technique decomposes the measured coherency matrix into a sum of three independent scattering models such that

$$\langle [T] \rangle = f_s [T]_s + f_D [T]_D + f_V [T]_V \quad (5)$$

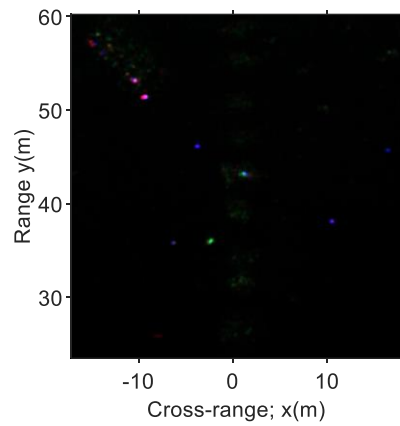
where  $[T]_s$ ,  $[T]_D$  and  $[T]_V$  denote respectively the scattering models for a surface, even- or double-bounce and volume scatters, with corresponding coefficients  $f_s$ ,  $f_D$  and  $f_H$ . These coefficients can be estimated from Eq. (4) from which the scattering power of each component, viz.  $P_s$ ,  $P_D$  and  $P_V$  can be calculated. Finally, a RGB image can be derived to portray these power contributions in a single image.

Fig. 8 shows the composite RGB image obtained after applying Freeman-Durden decomposition on the study site's L-band data. Blue, red and green correspond to  $|P_s|$ ,  $|P_D|$  and  $|P_V|$ . These power contributions are also displayed separately in Fig. 9, to aid interpretation. The signatures of the canonical targets, i.e., CR1, CR4 CR5 and the vertical stick (T2) appear to be almost same as obtained previously. However the gazebo and tree canopy, in this case, are mainly shown in green color arisen from volume scattering. This is reasonable because of these targets' complicated geometric scattering structures. It is also worth pointing out that simple objects within the gazebo area, i.e., two waste containers and the trihedral C2 can now be clearly discerned and separated from the other pixels, with their dominant double-bounce scattering response. The trihedral within the trees (C3) has light green color which indicates the coexistence of odd-bounce and volume scatterings, as expected. On the other hand, the oriented sticks T3 and T4 are also represented in

volume scattering category, revealing the technique’s well-known limitation. More clearly, the decomposition is not able to discriminate between cross-polarized scattering caused by tilted manmade targets and cross-polarized scattering caused by vegetation (or tree) canopies. Nevertheless, it is apparent that Freeman-Durden decomposition provides a better characterization of the observed backscatter when compared to Pauli and Krogager decompositions.



**Figure 7.** Amplitude images of Krogager decomposition components in a dB scale.



**Figure 8.** Freeman decomposition image with RGB color-coding: blue,  $|P_S|$ ; red,  $|P_D|$ ; and green,  $|P_H|$ .

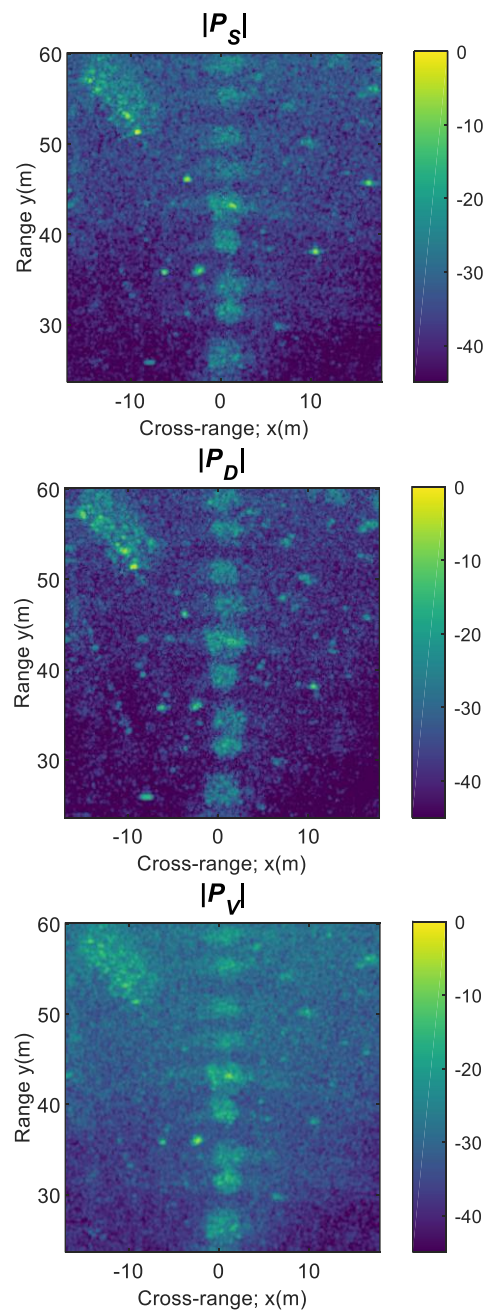


**Figure 9.** Power images of Freeman-Durden decomposition components in a dB scale

#### 4.5 Eigenvalue/Eigenvector Decomposition

Next, the widely-used eigenvalue/eigenvector-based decomposition was utilized. For this purpose, the averaged coherency matrix  $\langle [T] \rangle$  was diagonalised and expanded into incoherent sum of three independent coherency matrices  $[T_i]$  as follows

$$\langle [T] \rangle = [T_1] + [T_2] + [T_3] = \sum_{i=1}^3 \lambda_i \vec{e}_i \cdot \vec{e}_i^+ \quad (6)$$

where  $\lambda_1 \geq \lambda_2 \geq \lambda_3 \geq 0$  are the eigenvalues,  $\vec{e}_1, \vec{e}_2$  and  $\vec{e}_3$  are the unit eigenvectors and the superscript + denotes conjugate transpose operation. Each of the  $[T_i]$  matrices represents a single deterministic scattering process, the strength and type of which are determined by the corresponding eigenvalue and eigenvector, respectively. From these primary parameters, secondary statistical parameters such as polarimetric entropy ( $H$ ), anisotropy ( $A$ ), alpha angle ( $\alpha$ ) and beta angle ( $\beta$ ) can be extracted and plotted for the interpretation of the information provided by the decomposition.

The top image in Fig. 10 shows the estimated entropy map of the investigated scene. Entropy is a measure of the degree of randomness of scattering which takes values between 0 and 1. An entropy of 0 indicates a non-depolarizing (deterministic) scattering while 1 indicates a fully-depolarizing (random) scattering. We observe that entropy is high in most of the tree regions, as expected. In addition, high entropy also occurs over the vegetated areas that are more distant from the radar whereas the nearer areas have low entropy. This can become evident when considering the Rayleigh roughness criterion for surface scattering. More specifically, the illumination of farther targets with lower incidence angles (see Fig. 1) gives rise to more penetration of electromagnetic waves into scatter ensemble, thereby resulting in a depolarized scattering. Concerning the manmade targets, the rear part of the gazebo has high entropy because of random vector scattering from structurally complex targets. The front part, on the other hand, has low entropy, as a result of coherent reflections. Besides, the two waste containers and the trihedral C2 within that area, have nearly minimum  $H$  values, so are showing a nondepolarizing mechanism. This is also observed to be true for the other reflectors, except the concealed one. Lastly, the sticks exhibit weakly depolarizing behavior as evident from low to moderate  $H$  values.

The type of scattering process, as mentioned, is associated with the eigenvector information. The mean-alpha angle  $\bar{\alpha}$  is an average representation of this information and mainly used for the prediction of the dominant scattering mechanism present in the target. It ranges from  $0^\circ$  to  $90^\circ$  with values; in general,  $0^\circ \leq \bar{\alpha} \leq 30^\circ$ ,  $40^\circ \leq \bar{\alpha} \leq 50^\circ$  and  $60^\circ \leq \bar{\alpha} \leq 90^\circ$  are regarded as surface, dipole and dihedral scatterings, respectively. The middle image in Fig. 10

shows the spatial distribution of  $\bar{\alpha}$  values for the investigated scene. Targets that cause double-bounce mechanisms can be recognized as greenish to yellowish colors. Various parts of the trees and gazebo, and the horizontal cylinder present such expected mechanism. The tilted stick (T3) with  $\bar{\alpha}$  around  $65^\circ$ , however, also has double-bounce scattering, rather than dipole scattering. Note that  $\alpha$  parameter is independent from the orientation of the target about the radar LOS. Thus, these double-bounce returns are supposed to be originated from the bottom of the target, where a stone was used as a support material. Finally, the terrain with low vegetation and the reflectors have  $\bar{\alpha}$  values below  $30^\circ$  indicating a dominance of anisotropic surface or single-bounce mechanism.

Another parameter that can be obtained is the  $\beta$  angle which describes the orientation of a target about the LOS. The bottom image in Fig. 10 shows this map of the scene whereby all the targets that have orientations in azimuth direction, namely, the two  $45^\circ$  oriented sticks, the gazebo structure, the trees and various bushes can be readily distinguished.

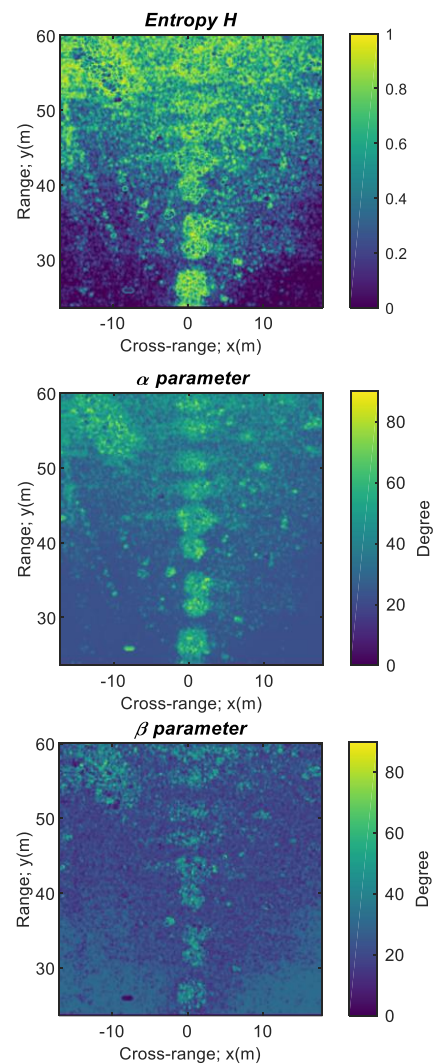


**Figure 10.** Entropy,  $\bar{\alpha}$  and  $\bar{\beta}$  angle maps for the test site, obtained after application of eigenvalue/eigenvector decomposition

#### 4.6 $H/\bar{\alpha}$ classification

The entropy ( $H$ ) and mean alpha ( $\bar{\alpha}$ ) values can be used in pairs for classification of random scattering mechanisms. The  $H/\bar{\alpha}$  classification scheme proposed in (Cloude and Pottier 1997) for L-band is based on the subdivision of the  $H/\bar{\alpha}$  plane into 9 scattering classes (8 usable) whose partitioning and descriptions are illustrated in Fig. 11(a). The result of applying this classification scheme is shown in Fig. 11(b) where the assigned color of each class is also given on the right.

Pixels belonging to the trees, plants and gazebo are mostly classified into Z3. This reflects moderately random multiple-bounce mechanisms mainly associated with trunk-ground interactions. Besides, there are also pixels classified as Z4 which indicates medium entropy dipole-like scattering due to secondary scattering processes. Both of these mechanisms are also seen for the gazebo area. However, the waste containers and the trihedral can be distinguished from this structure, with low-entropy dipole (Z7) and surface-like (Z8) scatterings. The TCR targets are correctly classified as Z8. Even the hidden TCR can be discerned from its blue color. Concerning the other targets, the oriented stick T3 is recognized to have each type scattering classes of Z3, Z6 and Z7, which can be again attributed to its base support. Lastly, the horizontal cylinder as well as some plants along the pave road are classified as Z6 showing a deterministic dihedral scattering.

#### 5. CONCLUSION

We presented a proof-of-concept type study for the employment of polarimetric GB-SAR imaging technology. An experimental assessment of the polarimetric L-band backscattering of a typical terrain and man-made targets was made through GB-SAR data. The measurement set-up and the polarimetric analysis techniques were explained. The coherent and incoherent decompositions of backscattering data provided satisfactorily efficient means to interpret the dominant scattering mechanisms occurring within the scene.

#### ACKNOWLEDGMENT

The authors are grateful to Mersin Technology Development Zone (Technoscope) for providing laboratory facilities for the conducted experiments.

#### REFERENCE

- Alberga V, Krogager E, Chandra M & Wanielik G (2004). Potential of coherent decompositions in SAR polarimetry and interferometry. 2004 IEEE International Geoscience and Remote Sensing Symposium, Anchorage, AK, USA.
- Albinet C, Borderies P, Koleck T, Rocca F, Tebaldini S, Villard L, Toan T L, Hamadi A & Minh D H T (2012). TropiSCAT: A ground based

The authors are thankful to Dr. Betul Yilmaz, Hakan Isiker and Serhat Gokkan, for their valuable help during the experiments.

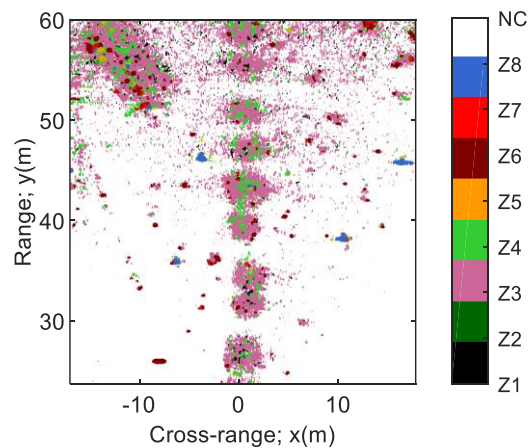
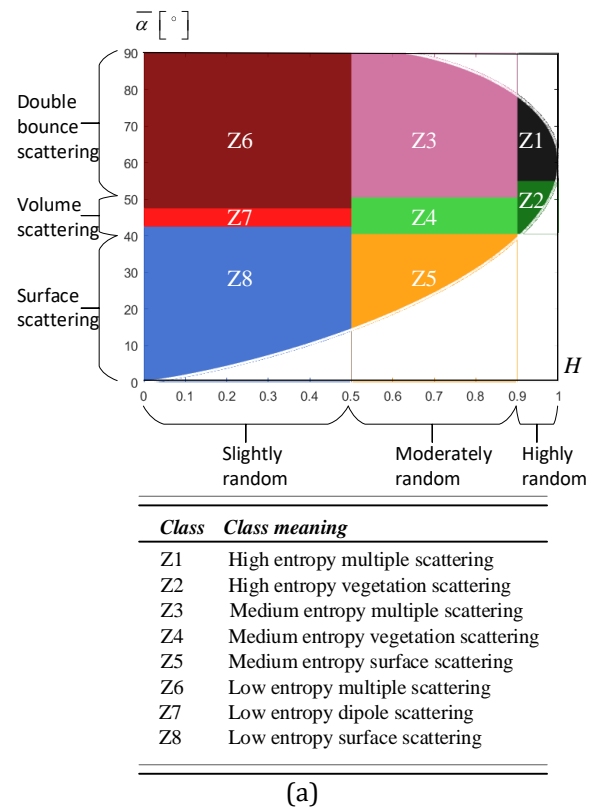


**Figure 11.** (a)  $H/\bar{\alpha}$  plane with classes (Z1-Z8) and their partitioning and descriptions. (b)  $H/\bar{\alpha}$  classification result for the test scene (NC means not-classified)

polarimetric scatterometer experiment in tropical forests. IEEE Journal of Selected Topics in Applied Earth Observations and Remote Sensing (JSTARS), 5(3), 1060-1066.

Baffelli S, Frey O, Werner C & Hajnsek I (2018). Polarimetric calibration of the Ku Band advanced polarimetric radar interferometer

- (KAPRI). *IEEE Transactions on Geoscience and Remote Sensing*, 56(4), 2295–2311.
- Brown S C M, Quegan S, Morrison K, Bennett J C & Cookmartin G (2003). High-resolution measurements of scattering in wheat canopies-implications for crop parameter retrieval. *IEEE Transactions on Geoscience and Remote Sensing*, 41(7), 1602–1610.
- Chen S W, Li Y Z, Wang X S, Xiao S P & Sato M (2014). Modeling and interpretation of scattering mechanisms in polarimetric synthetic aperture radar: Advances and perspectives. *IEEE Signal Processing Magazine*, 31, 79–89.
- Chen S W, Wang X S, Xiao S P & Sato M (2018). Advanced polarimetric target decomposition. In: *Target scattering mechanism in polarimetric synthetic aperture radar*. Singapore: Springer.
- Cho B L, Kong Y K, Park H G & Kim Y S (2006). Automobile-based SAR/InSAR system for ground experiments. *IEEE Geoscience and Remote Sensing Letters*, 3(3), 401-405.
- Cloude S R & Pottier E (1996). A review of target decomposition theorems in radar polarimetry. *IEEE Transactions on Geoscience and Remote Sensing*, 34(2), 498–518.
- Cloude S R & Pottier E (1997). An entropy based classification scheme for land applications of polarimetric SAR. *IEEE Transactions on Geoscience and Remote Sensing*, 35(1), 68–78.
- Cloude S R (2010). *Polarisation application in remote sensing*. Oxford: Oxford Univ. Press.
- Cuenca L M (2017). Contribution to ground-based and UAV SAR systems for Earth observation. Ph. D. dissertation, Universitat Politècnica de Catalunya, Barcelona, Spain.
- Demirci S, Yilmaz B, Isiker H, Gokkan S & Ozdemir C (2019). Characterization of natural and manmade targets from L-band ground-based polarimetric synthetic aperture radar data. *Journal of Applied Remote Sensing*, 13(4), doi: 10.1117/1.JRS.13.044512.
- Freeman A & Durden S L (1998). A three-component scattering model for polarimetric SAR data. *IEEE Transactions on Geoscience and Remote Sensing*, 36(3), 963–973.
- Gonzalez-Partida J T, Almorox-Gonzalez P, Burgos-Garcia M & Dorta-Naranjo B P (2008). SAR system for UAV operation with motion error compensation beyond the resolution cell. *Sensors*, 8(5), 3384-3405. DOI: 10.3390/s8053384
- Iglesias R, Aguasca A, Fabregas X, Mallorqui J J, Monells D & Lopez C (2015a). Ground-based polarimetric SAR interferometry for the monitoring of terrain displacement phenomena–Part I: Theoretical description. *IEEE Journal of Selected Topics in Applied Earth Observations and Remote Sensing*, 8(3), 980-993.
- Iglesias R, Aguasca A, Fabregas X, Mallorqui J J, Monells D & Lopez C (2015b). Ground-based polarimetric SAR interferometry for the monitoring of terrain displacement phenomena–Part II: applications. *IEEE Journal of Selected Topics in Applied Earth Observations and Remote Sensing*. 8(3), 994-1007.
- Kang M K, Kim K E, Lee H, Cho S J & Lee J H (2009). Preliminary results of polarimetric characteristics for C-band quad-polarization GB-SAR images using H/A/alpha polarimetric decomposition theorem. *Korean Journal of Remote Sensing*, 25(6), 531-546.
- Krogager E (1990). New decomposition of the radar target scattering matrix. *Electronics Letters*, 26, 1525–1527.
- Lee H, Cho S J, Sung N H & Kim J H (2007). Development of a GB-SAR (II): Focusing algorithms. *Korean Journal of Remote Sensing*, 23(4), 247–256.
- Lee H, Ji Y & Han H (2016). Experiments on a ground-based tomographic synthetic aperture radar. *Remote Sensing*, 8(8), 1-11. DOI: 10.3390/rs8080667
- Lee H, Lee J -H, Kim K -E, Sung N -H & Cho S -J (2014). Development of a truck-mounted arc-scanning synthetic aperture radar. *IEEE Transaction on Geoscience and Remote Sensing*, 52(5), 2773-2779.
- Lee J & Pottier E (2009). *Polarimetric radar imaging: From basics to applications*. Boca Raton: Taylor & Francis.
- Lim K S & Koo V C (2008). Design and construction of wideband VNA ground-based radar system with real and synthetic aperture measurement capabilities. *Progress in Electromagnetics Research, PIER*, 86, 259–275.
- Minh D H T, Tebaldini S, Rocca F, Toan T L, Borderies P, Koleck T, Albinet C, Hamadi A & Villard L (2014). Vertical structure of P-Band temporal decorrelation at the Paracou forest: Results from TropiScat. *IEEE Geoscience and Remote Sensing Letters*, 11(8), 1438–1442.
- Moreira A, Prats-Iraola P, Younis M, Krieger G, Hajnsek I & Papathanassiou K (2013). A tutorial on synthetic aperture radar. *IEEE Geoscience and Remote Sensing Magazine*, 1(1), 6-43. DOI: 10.1109/MGRS.2013.2248301
- Ouchi K (2013). Recent trend and advance of synthetic aperture radar with selected topics. *Remote Sensing*, 5(2), 716-807. DOI: 10.3390/rs5020716
- Ozdemir C, Demirci S, Yigit E & Yilmaz B (2014). A review on migration methods in B-Scan ground penetrating radar imaging. *Mathematical Problems in Engineering*, 1-16. DOI: 10.1155/2014/280738
- Penner J F & Long D G (2017). Ground-based 3D radar imaging of trees using a 2D synthetic aperture. *Electronics*, 6(11), 1-13. DOI: 10.3390/electronics6010011
- Pipia L (2009). Polarimetric differential SAR interferometry with ground-based sensors.

- Ph.D. dissertation, Universitat Politecnica de Catalunya, Barcelona, Spain.
- Pipia L, Fabregas X, Aguasca A & Lopez-Martinez C (2013). Polarimetric temporal analysis of urban environments with a ground-based SAR. *IEEE Transactions on Geoscience and Remote Sensing*, 51(4), 2343–2360.
- Sevgen S C (2019). Airborne LIDAR data classification in complex urban area using random forest: A case study of Bergama, Turkey. *International Journal of Engineering and Geosciences*, 4(1), 45-51. DOI: 10.26833/ijeg.440828
- The MathWorks, Inc. MATLAB, Release 2018. Natick, Massachusetts, United States.
- Van Zyl J J & Kim Y (2011). Synthetic aperture radar polarimetry. Hoboken, NJ: John Wiley & Sons, Inc.
- Xing S, Li Y, Dai D & Wang X (2013). Three-dimensional reconstruction of man-made objects using polarimetric tomographic SAR. *IEEE Transactions on Geoscience and Remote Sensing*, 51(6), 3694–3705.
- Yilmaz A & Erdogan M (2018). Designing high resolution countrywide DEM for Turkey. *International Journal of Engineering and Geosciences*, 3(3), 98-107. DOI: 10.26833/ijeg.384822
- Yilmaz M & Uysal M (2017). Comparing uniform and random data reduction methods for DTM accuracy. *International Journal of Engineering and Geosciences*, 2(1), 9-16. DOI: 10.26833/ijeg.286003
- Zhou Z S (2003). Application of a ground-based polarimetric SAR system for environmental study. Ph.D. dissertation, The Graduate School of Engineering, Tohoku University, Sendai, Japan.
- Zhou Z S (2004). Development of a ground-based polarimetric broadband SAR system for noninvasive ground-truth validation in vegetation monitoring. *IEEE Transactions on Geoscience and Remote Sensing*, 42(9), 1803–1810.



© Author(s) 2021.

This work is distributed under <https://creativecommons.org/licenses/by-sa/4.0/>



## Automatic extraction of trees by using multiple return properties of the lidar point cloud

Samed Ozdemir <sup>\*1</sup>, Zeynep Akbulut <sup>1</sup>, Fevzi Karsli <sup>2</sup>, Hayrettin Acar <sup>2</sup>

<sup>1</sup>Gümüşhane University, Engineering and Natural Sciences Faculty, Department of Geomatics Engineering, Gümüşhane, Turkey

<sup>2</sup>Karadeniz Technical University, Engineering Faculty, Department of Geomatics Engineering, Trabzon, Turkey

### Keywords

Automatic  
Tree Extraction  
LiDAR  
Multiple Return

### ABSTRACT

Airborne laser scanning has been a valuable tool for forestry applications since it began to be used commercially. Thanks to the high 3D resolution provided by the Light Detection and Ranging (LiDAR) point cloud, it has provided great convenience in complex 3D modeling processes needed for forestry applications such as forest inventory, forest management, determination of carbon stocks and the characterization of biodiversity. LiDAR data provides a new dimension in forestry applications with its high 3D resolution and multiple return characteristics. The extraction of woodland areas from the LiDAR point cloud has great importance for automating the determination of tree heights, species and stand frequency which will be used for generating canopy height models (CHM). In this study, woodland areas in the urban scene were automatically extracted by using the multiple return properties of the LiDAR point cloud. The proposed approach consists of three major steps namely pre-processing, parameter calculation and k-d tree search for trees which were implemented in MATLAB. In the first step, multiple return points have been identified from the LiDAR point cloud, which will be then used to determine possible tree locations. Then, by using Density-Based Spatial Clustering of Applications with Noise (DBSCAN) algorithm, neighborhood relations among the multi return points which were extracted from the initial point cloud data, were formed and a rule-based filter was applied by taking advantage of neighborhood relations. In addition, the initial point cloud was filtered with the Cloth Simulation Filtering (CSF) algorithm to separate ground and non-ground points where non-ground points used to extract trees. In the second step, non-vegetation points were removed by applying a threshold based on the change of curvature and planarity parameters, which are derived from the filtered non-ground point cloud. In the last step, in order to extract trees, a k-d tree structure was created from the filtered non-ground points to find nearest neighbors of each multi return point within a given diameter in the k-d tree structure. In order to evaluate the accuracy of the approach, the extracted boundaries were compared with the manually digitized woodland boundaries from the true orthophoto of the study area using correctness, completeness and quality metrics.

## 1. INTRODUCTION

Remote sensing data has become a reliable source for determining forest parameters due to the broad data coverage, data accessibility and advanced image processing techniques, both at the individual tree level and at the tree community level (Chen and Zhu 2013; Mielcarek et al. 2018). However, 2D systems do not provide important structural and geometric information such as the internal structure of the trees and canopy characteristics. Therefore,

there is a need for 3D information including detailed geometric and structural information about the trees (Liu et al. 2019; Ramiya et al. 2019). Nowadays, LiDAR data is actively being used in many different kinds of forestry applications thanks to the characteristic trait of LiDAR signals' penetration capability of tree canopies (Liu et al. 2013; Vêga et al. 2014). Penetration capability of LiDAR signals provides accurate information about the tree structures and the ground beneath the trees

### \* Corresponding Author

(samed.ozdemir@gumushane.edu.tr) ORCID ID 0000 - 0001 - 7217 - 899X  
(zeynepakbulut@gumushane.edu.tr) ORCID ID 0000 - 0001 - 9801 - 1506  
(fkarsli@ktu.edu.tr) ORCID ID 0000 - 0002 - 0411 - 3315  
(h\_acar@ktu.edu.tr) ORCID ID 0000-0002-2954-7734  
Research Article / DOI: 10.26833/ijeg.668352

### Cite this article

Ozdemir S, Akbulut Z, Karsli F & Acar H (2021). Automatic extraction of trees by using multiple return properties of the lidar point cloud. International Journal of Engineering and Geosciences, 6(1), 20-26

(Reutebuch et al. 2003; Vége et al. 2014; Mielcarek et al. 2018; Liu et al. 2019; Ramiya et al. 2019). This property makes LiDAR a powerful tool for monitoring, assessment and segmentation of forest areas, tree canopies and individual trees due to its speed, coverage and 3D information (Vége et al. 2014; Beland et al. 2019; Liu et al. 2019; Ramiya et al. 2019).

Mapping and monitoring of urban woodland areas have vital importance due to the effects of urban woodland areas on local micro-climate, air quality and ecosystem. It is also a known fact that urban green spaces improve health, wellbeing, and quality of life for urban residents (Haq 2011; Gupta et al. 2018; Ramiya et al. 2019). Successful results have been obtained in many studies using LiDAR point cloud data for forestry applications. Widely used methods for forestry applications can be categorized into three groups, which are raster-based, point cloud based and hybrid methods. Raster-based methods work by locating each canopy over the local maxima via the canopy height model (CHM) (Popescu 2007). Point-based methods allow the determination of each canopy by using local geometry and structural features amongst the points within a local neighborhood (Zhen et al. 2016; Ramiya et al. 2019). There are a few things to consider here. Raster-based methods reduce the complexity of computations and increase performance while losing the geometric and structural information from the point cloud. On the other hand, although point-based methods are computationally expensive, they retain the structural and geometric properties of the canopy and make the most of this information. In the hybrid method, canopies are located from 2D CHMs by using local maxima based on image processing techniques and tree points are extracted from the point cloud using this location information (Lindberg et al. 2014; Liu et al. 2019).

In the last two decades LiDAR technology used for measuring the tree canopy by using both terrestrial and airborne LiDAR data (Hyyppä et al. 2001; Van der Zande et al. 2006; Koch et al. 2006). Moreover, new methodologies developed by merging LiDAR point cloud data with remotely sensed images to extract trees (Dogon-Yaro et al. 2016; Hartling et al. 2019). However, most of the studies focused on trees in forested areas (Liu et al. 2013). Trees located in an urban environment also as important as trees in forested areas because they are closely related to the residents of the urban environment (Liu et al. 2013). Secord and Zakhor (2007) proposed an approach for automatic detection of trees using LiDAR and aerial imagery using Support Vector Machines (SVM). Despite obtaining good results, collecting a huge number of training data required to train SVM algorithm is not suitable for most applications. Besides, aerial imagery must be precisely registered with the LiDAR data to obtain the desired accuracy. Liu et al. (2013) used only LiDAR data to extract individual tree

crowns in urban areas by using multiple return properties to segment trees with a surface growing algorithm. The proposed algorithm extracted 85% of the trees located in the test areas. Gupta et al. (2018) used multi return information of LiDAR point cloud to identify individual tree canopies by voxelizing the point cloud data and applying a connected component analysis. The proposed method achieved approximately 90% percent accuracy in a high-resolution urban LiDAR dataset. Ramiya et al. (2019) used supervoxels and geometric information of LiDAR point cloud such as pointedness, curviness and surfacedness parameters to classify individual tree crowns using random forest classification. Their approach achieved 99% accuracy with high-resolution LiDAR point cloud data in an urban environment.

In this paper, a new approach proposed to extract tree canopies by using multiple return properties of LiDAR data in urban areas. The proposed approach consists of three steps that were implemented in MATLAB. In the first step, the LiDAR point cloud was filtered with the CSF algorithm to detect ground and non-ground points. Then, the multi return points were extracted from the point cloud and clustered with the DBSCAN algorithm to create neighborhood relations and filter out possible outlier points. In the second step, change of curvature and planarity parameters were calculated from the filtered non-ground points to distinguish trees from the non-vegetation objects such as buildings. In the last step, a k-d tree structure created from the remaining points, which were filtered with the previously mentioned parameters. Finally, a range search was initialized in the k-d tree structure by using the multiple return points and the tree points were extracted. Accuracy assessment of the proposed approach was evaluated with the correctness, completeness and quality metrics.

## 2. STUDY AREA and DATASET METHOD

The study areas were selected from the ISPRS's Vaihingen dataset (Cramer 2010) which includes LiDAR point cloud and an orthophoto of the region. In the benchmark dataset, LiDAR data has an average density of 8 points/m<sup>2</sup> and up to four returns recorded for each signal. The orthophoto has 9 cm ground sampling distance and three channels (NIR, green and blue). The study areas that are shown in (Figure 1) comprises of trees with varying density, size, shape and height. Also, some single and small trees can be found along with landscaping for both of the study areas. Study areas specifically selected for study area 1, there are three multi-story buildings with heights approximately 20 meters and none of the building's roofs obstructed by trees. For study area 2, all of the buildings are detached and some building's roofs are partially obstructed by a nearby tree. The study areas were chosen considering the complex relationships of buildings and trees in an urban scene.

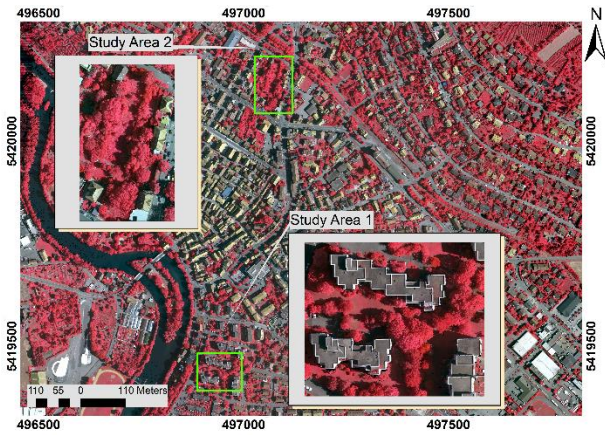


**Figure 1.** Study areas

### 3. METHODOLOGY

In order to extract trees, a three steps methodology namely; pre-processing, parameter calculation and k-d tree search for trees were implemented in MATLAB. All of the steps are explained in detail in the following sections.

#### 3.1 Pre-Processing

Pre-processing contains clustering and filtering steps, which are described in detail in the sub-sections.

##### 3.1.1 Clustering

Firstly, multiple return points were extracted from the initial LiDAR point cloud, which were later used to search for trees. These points were then separated into different clusters with the DBSCAN algorithm according to the maximum distance and minimum neighboring point parameters. The maximum distance parameter determines if a point is close to any other points in a cluster. In addition, the minimum neighboring point's parameter determines if the cluster has enough points to be considered as a cluster. If a cluster fulfills these two conditions, they will be labeled with a cluster number and the DBSCAN algorithm seeks for other clusters in the remaining points (Ester et al. 1996). The maximum distance and minimum neighbor number parameters were selected as 3 m and 5 points, respectively. Points that meet these conditions clustered together and labeled with a cluster number otherwise points marked as noise and were removed from the multi return point cloud.

##### 3.1.2 Filtering

In order to avoid errors that may arise from ground points and the points close to the ground such as LiDAR returns from vehicles and low vegetation, point cloud must be filtered with an appropriate filtering algorithm. In this study, CSF algorithm (Zhang et al. 2016) was used for LiDAR point cloud filtering. CSF algorithm based on the simulation of a cloth model. Cloth simulation is a

term used in 3D computer graphics. The cloth can be modeled as a grid structure in which every grid node has mass and interconnections. The cloth model's grid nodes' interconnections are modeled as virtual springs which are governed by Hooke's law. Several modifications have been made to the algorithm to make the simulation run on LiDAR point clouds. First, the movement of grid nodes constrained in the vertical direction to detect collisions by comparing height values of grid node and terrain. Second, when a node reaches the ground, this node is set as unmovable. Third, cloth model simulation simplified by omitting collision forces operating on grid nodes (Zhang et al. 2016).

To detect ground points, firstly, CSF method turns point cloud upside down and fits a cloth model to this point cloud with the given cloth parameters as shown in Figure 2. Then, the cloth model's nodes interact with the corresponding points in the point cloud to find a suitable location. After the cloth simulation ends, ground points can be detected with the final shape of the cloth model by measuring distances between the cloth model and points (Figure 2).

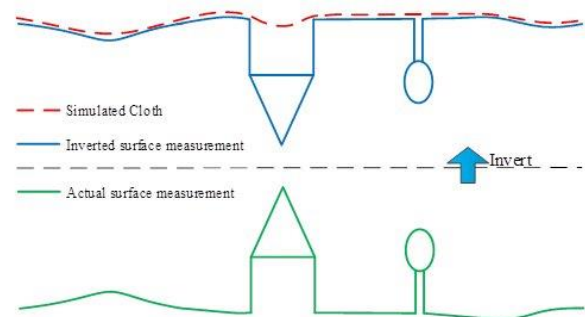


**Figure 2.** Overview of the CSF algorithm (Zhang et al. 2016)

Ground and non-ground point classes were obtained with the CSF algorithm. After the filtering process, non-ground points still have low-lying points (vehicles, low vegetation, etc.) which should be cleared to improve the final result of the study. Therefore, a Digital Terrain Model (DTM) was generated from the ground points and this surface elevated by two meters. Then, the obtained surface was applied to the non-ground points to clear the points under the surface. Thus, low objects such as vehicles and low vegetation were removed from the non-ground points (Figure 3).

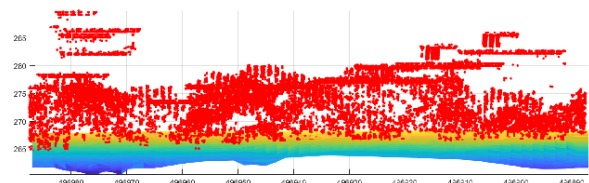


**Figure 3.** First study area: non-ground LiDAR points shown in red above the elevated ground surface

### 3.2 Parameter Calculation

Depending on the flight path and scan angle of the LiDAR instrument, trees and building edges can cause multi return points. Multi return LiDAR points from the buildings must be eliminated in order to search the LiDAR point cloud for neighbors of multi return points. To remove the multi return points from the buildings, we used planarity (Eq. 1) and change of curvature (Eq. 2) parameters (Pauly et al. 2003; Weinmann et al. 2015; Sevgen 2018) which was calculated from the filtered non-ground points (Figure 4). These eigenvalues contain valuable information about the local surface variation. 3D structure tensor of 3D covariance matrix of the 3D point cloud represents a symmetric positive semidefinite matrix which has three nonnegative eigenvalues and corresponding eigenvectors. Therefore, this information can be used to acquire local features around a 3D point (Weinmann 2016).

$$\text{Planarity} = \frac{e_2 - e_3}{e_1} \quad (1)$$

$$\text{Change of Curvature} = \frac{e_3}{\sum_{i=1}^3 e_i} \quad (2)$$

Where  $e_i$  denotes the eigenvalues of the covariance matrix of neighboring points with the subscript numbers representing the first, second and third eigenvalues in  $e_1 \geq e_2 \geq e_3$  order.

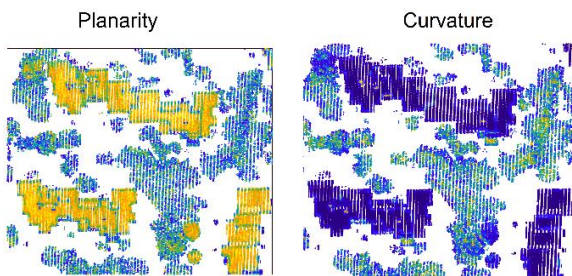


**Figure 4.** Calculated planarity and change of curvature parameters for study area 1. Blue color represents the value of 0 and yellow color represents the value of 1 for the calculated parameters.

A simple threshold-based method was employed in order to detect and remove the multi return building points from the point cloud using planarity and change of curvature parameters. Firstly, the change of curvature and planarity parameters were normalized between 0 to 1 value. A new parameter was calculated dividing planarity by the change of curvature parameter which was then used for thresholding. The threshold value was determined by Otsu's threshold method proposed by Otsu N. (1979) which selects a threshold value to maximize the variance between high and low parameter values. Points having a higher value from the calculated threshold and their neighboring multi-return points within a 1 m search radius were

removed from the point cloud. Detected multi-return points belonging to possible trees are shown in Figure 5.

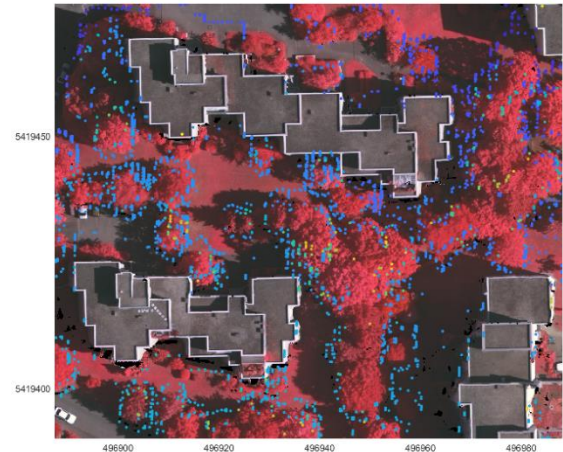


**Figure 5.** Possible multi-return tree points for the study area 1

### 3.3 K-D Tree Search for Tree Points

In the point cloud, which was filtered according to the change of curvature and planarity parameters; it was ensured that the neighborhoods of multi return points can be found quickly using the k-d tree structure. The K-d tree structure is a widely used method for database searches, statistics and computer vision. The K-d tree method is a binary tree method developed by Bentley, J. L. (1975). This method allows quick search within a large data set by splitting a given data set into many sub-segments with hyperplanes. These sub-segments are called leaf nodes which are indicated with a pointer. For a given point, K-d tree method quickly searches the data set using pointers to identify the leaf node closest to the given point. In the tree structure, all the neighbors with a diameter of 5 meters were determined using the multi return points produced in the data preprocessing stage. Points with less than or equal to 3 points in the neighborhood were discarded and the remaining points were recorded as tree points is shown in Figure 6 and Figure 7.

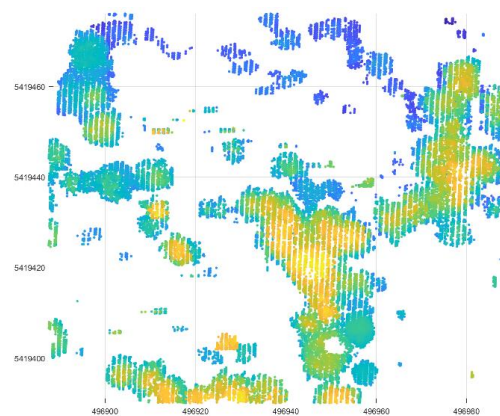


**Figure 6.** K-d tree search results for tree identification from multi-return points for study area 1

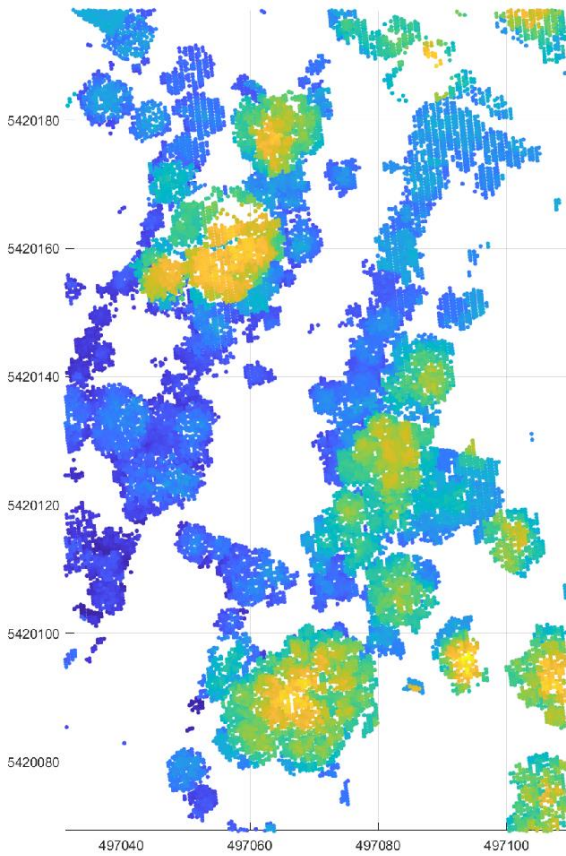


**Figure 7.** K-d tree search results for tree identification from multi-return points for study area 2

#### 4. RESULTS and DISCUSSION

The proposed approach was evaluated in two urban study areas with various types of tree structures and stand types. Extracted tree boundaries were compared with the manually digitized reference tree boundaries. For the two study areas, accuracy assessment was evaluated with the correctness, completeness and quality metrics by the following equations (3, 4, 5). Accuracy assessment results are shown in Table 1.

$$Completeness = \frac{\|TP\|}{\|TP\| + \|FN\|} \quad (3)$$

$$Correctness = \frac{\|TP\|}{\|TP\| + \|FP\|} \quad (4)$$

$$Quality = \frac{\|TP\|}{\|TP\| + \|FN\| + \|FP\|} \quad (5)$$

Where, TP refers to an entity classified as an object that also corresponds to an object in the reference is classified as a true positive, FN (false negative) refers to an entity corresponds to an object in the reference that is classified as background, FP (false positive) refers to an entity classified as an object that does not correspond to an object in the reference and TN (true negative) refers to an entity belongs to the background both in the classification

and in the reference data (Rutzinger et al. 2009, Karsli et al. 2016, Akbulut et al. 2018). Reference data was created from the LiDAR point cloud by manually selecting tree points. Then, collected tree points were used to create a binary reference raster by mapping every point to a raster cell. After creating a reference raster, void pixels caused by point spacing were filled with a dilation operation using a circular structuring element.

**Table 1.** Accuracy assessment results for study areas

	Correctness	Completeness	Quality
Area 1	0.9157	0.8794	0.8135
Area 2	0.9456	0.8569	0.8167

For both of the two test areas, the proposed approach extracted trees with reasonable accuracy. Especially, large tree canopies consisting of multiple trees and single trees with relatively wide canopy and height, extracted with reasonable accuracy as shown in Figure 8.

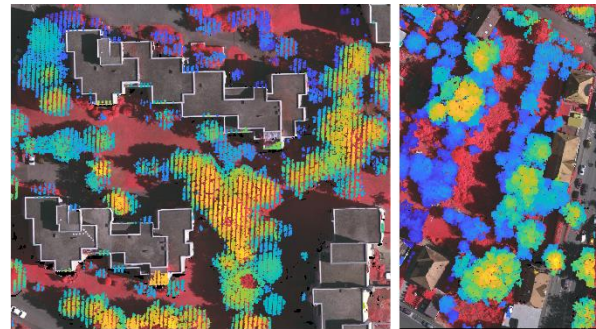


**Figure 8.** Tree extraction results were obtained with the proposed approach. The left image shows tree extraction results for study area 1, and the right image shows tree extraction results for study area 2.

However, single trees with low height and thin canopies were not extracted because most of the above ground objects lower than two meters were filtered. Also, some of the building roofs intertwined with the trees were complicated the tree extraction process, which can be seen in results for study area 2 in Figure.8. Moreover, high buildings have LiDAR returns from the building's walls and this situation creates some problems for the parameter calculation step that results in misidentified tree points. Overall, the proposed approach was achieved over 90% correctness, 85% completeness, and 81% quality, which can be improved in later studies. The accuracy assessment results acquired with the proposed approach compared with the results from Liu et al. (2013) and Gupta et al. (2018). Liu et al. (2013) assessed the accuracy of their approach on two test areas and acquired 92% and 94% correctness, 87% and 85% completeness. Gupta et al. (2018) acquired 88% correctness and 89% completeness for a single test area. In the light of these comparisons, the proposed approach performed reasonably well with some minor flaws.

## 5. CONCLUSION

Promising results have been achieved in the Vaihingen data set with the proposed approach. The dense tree clusters with multiple trees were determined with reasonably high accuracy. The determination of individual trees was achieved with an appreciable success considering the canopy structure and height of the tree. The proposed approach may give different results when the trees and buildings are adjacent to each other. The reasons for this are that the parameters obtained from the point cloud depend on the changes in the neighborhood distance and LiDAR returns from the building walls. The proposed approach will be improved by addressing the aforementioned problems in future studies.

## REFERENCES

- Akbulut Z, Özdemir S, Acar H, Dihkan M & Karlı F (2018). Automatic extraction of building boundaries from high-resolution images with active contour segmentation. *International Journal of Engineering and Geosciences*, 3(1), 36-42.
- Beland M, Parker G, Sparrow B, Harding D, Chasmer L, Phinn S, Antonarakis A & Strahler A (2019). On promoting the use of lidar systems in forest ecosystem research. *Forest Ecology and Management*, 450, 117484. DOI: 10.1016/j.foreco.2019.117484
- Bentley J L (1975). Multidimensional binary search trees used for associative searching. *Communications of the ACM*, 18(9), 509-517. DOI: 10.1145/361002.361007
- Chen Y & Zhu X (2013). An integrated GIS tool for automatic forest inventory estimates of *Pinus radiata* from LiDAR data. *GIScience & remote sensing*, 50(6), 667-689. DOI: 10.1080/15481603.2013.866783
- Cramer M (2010). The DGPf-test on digital airborne camera evaluation-overview and test design. *Photogrammetrie-Fernerkundung-Geoinformation*, 2010(2), 73-82. DOI: 10.1127/1432-8364/2010/0041
- Dogon-Yaro M A, Kumar P, Rahman A A & Buyuksalih G (2016). Extraction of urban trees from integrated airborne based digital image and LiDAR point cloud datasets-initial results. *The International Archives of the Photogrammetry, Remote Sensing and Spatial Information Sciences*, 42, 81.
- Ester M, Kriegel H P, Sander J & Xu X (1996, August). A density-based algorithm for discovering clusters in large spatial databases with noise. In *Kdd*, 96(34), 226-231.
- Gupta A, Byrne J, Moloney D, Watson S & Yin H (2018). Automatic Tree Annotation in LiDAR Data. In *Proceedings of the 4th International Conference on Geographical Information Systems Theory, Applications and Management*, 36-41.
- Haq S M A (2011). Urban green spaces and an integrative approach to sustainable environment. *Journal of Environmental Protection*, 2(05), 601-608.
- Hartling S, Sagan V, Sidike P, Maimaitijiang M & Carron J (2019). Urban Tree Species Classification Using a WorldView-2/3 and LiDAR Data Fusion Approach and Deep Learning. *Sensors*, 19(6), 1284. DOI: 10.3390/s19061284
- Hyypä, J, Schardt M, Haggrén H, Koch B, Lohr U, Scherrer H U et al. (2001). HIGH-SCAN: The first European-wide attempt to derive single-tree information from laser scanner data. *The Photogrammetric Journal of Finland*, 17(2), 58-68.
- Karsli F, Dihkan M, Acar H & Ozturk A (2016). Automatic building extraction from very high-resolution image and LiDAR data with SVM algorithm. *Arabian Journal of Geosciences*, 9(14), 635. DOI: 10.1007/s12517-016-2664-7
- Koch B, Heyder U & Weinacker H (2006). Detection of individual tree crowns in airborne lidar data. *Photogrammetric Engineering & Remote Sensing*, 72(4), 357-363.
- Lindberg E, Eysn L, Hollaus M, Holmgren J & Pfeifer N (2014). Delineation of tree crowns and tree species classification from full-waveform airborne laser scanning data using 3-D ellipsoidal clustering. *IEEE Journal of Selected Topics in Applied Earth Observations and Remote Sensing*, 7(7), 3174-3181.
- Liu J, Shen J, Zhao R & Xu S (2013). Extraction of individual tree crowns from airborne LiDAR data in human settlements. *Mathematical and Computer Modelling*, 58(3-4), 524-535.
- Liu L, Lim S, Shen X & Yebra M (2019). A hybrid method for segmenting individual trees from airborne lidar data. *Computers and Electronics in Agriculture*, 163, 104871.
- Mielcarek M, Stereńczak K & Khosravipour A (2018). Testing and evaluating different LiDAR-derived canopy height model generation methods for tree height estimation. *International Journal of Applied Earth Observation and Geoinformation*, 71, 132-143.
- Otsu N (1979). A threshold selection method from gray-level histograms. *IEEE transactions on systems, man, and cybernetics*, 9(1), 62-66.
- Pauly M, Keiser R & Gross M (2003). Multi-scale feature extraction on point-sampled surfaces. In *Computer graphics forum*, 22(3), 281-289.
- Popescu S C (2007). Estimating biomass of individual pine trees using airborne lidar. *Biomass and Bioenergy*, 31(9), 646-655.
- Ramiya A M, Nidamanuri R R & Krishnan R (2019). Individual tree detection from airborne laser scanning data based on supervoxels and local convexity. *Remote Sensing Applications: Society and Environment*, 15, 100242.

- Reutebuch S E, McGaughey R J, Andersen H E & Carson W W (2003). Accuracy of a high-resolution lidar terrain model under a conifer forest canopy. *Canadian Journal of Remote Sensing*, 29(5), 527-535.
- Rutzinger M, Rottensteiner F & Pfeifer N (2009). A comparison of evaluation techniques for building extraction from airborne laser scanning. *IEEE Journal of Selected Topics in Applied Earth Observations and Remote Sensing*, 2(1), 11-20.
- Secord J & Zakhor A (2007). Tree detection in urban regions using aerial LiDAR and image data. *IEEE Geoscience and Remote Sensing Letters*, 4(2), 196-200.
- Sevgen S C (2018). Airborne lidar data classification in complex urban area using random forest: A case study of Bergama, Turkey. *International Journal of Engineering and Geosciences*, 4(1), 45-51. DOI: 10.26833/ijeg.440828
- Van der Zande D, Hoet W, Jonckheere I, van Aardt J & Coppin P (2006). Influence of measurement set-up of ground-based LiDAR for derivation of tree structure. *Agricultural and Forest Meteorology*, 141(2-4), 147-160. DOI: 10.1016/j.agrformet.2006.09.007
- Véga C, Hamrouni A, El Mokhtari S, Morel J, Bock J, Renaud J P & Durrieu S (2014). PTrees: A point-based approach to forest tree extraction from LiDAR data. *International Journal of Applied Earth Observation and Geoinformation*, 33, 98-108. DOI: 10.1016/j.jag.2014.05.001
- Weinmann M (2016). *Reconstruction and analysis of 3D scenes*. Springer.
- Weinmann M, Mallet C, Hinz S & Jutzi B (2015). Efficient interpretation of 3D point clouds by assessing feature relevance. *AVN–Allg Vermessung-Nachr*, 10(2015), 308-315.
- Zhang W, Qi J, Wan P, Wang H, Xie D, Wang X & Yan G (2016). An easy-to-use airborne LiDAR data filtering method based on cloth simulation. *Remote Sensing*, 8(6), 501. DOI: 10.3390/rs8060501
- Zhen Z, Quackenbush L J & Zhang L (2016). Trends in automatic individual tree crown detection and delineation—Evolution of LiDAR data. *Remote Sensing*, 8(4), 333. DOI: 10.3390/rs8040333



© Author(s) 2021.

This work is distributed under <https://creativecommons.org/licenses/by-sa/4.0/>



## Developing a mobile GIS application related to the collection of land data in soil mapping studies

Fatih Iscan <sup>\*1</sup>, Erkan Guler <sup>2</sup>

<sup>1</sup>Konya Technical University, Faculty of Engineering and Natural Sciences, Department of Geomatics Engineering, Konya, Turkey

<sup>2</sup>Republic of Turkey Ministry of Agriculture and Forestry, Ankara, Turkey

### Keywords

GIS  
Mobile GIS  
Soil  
Digital Soil Mapping

### ABSTRACT

Soil is the one of the most important natural resources having direct and indirect effects on human life, foremost on food supply. Moreover, two of the most important sources used in many sectors such as agriculture, forestry, environment, planning, related to the conservation of soil, are soil maps and soil reports. There is a need for proper and up-to-date soil maps produced with support of technology to achieve sustainable management of land and soil successfully. In order to facilitate the collection of soil data on site in a correct, fast and reliable way in soil survey and mapping studies, and therefore to produce soil maps with high accuracy, a mobile GIS application called "Soil Data System" was developed in this study to work in mobile devices which are driven by Android 5.0 and above. The developed application was tested in "Abadan Erosion Control Project" implementation area, which is located in the boundaries of Ankara, Turkey and was completed in 2016 within the General Directorate of Forestry of The Republic of Turkey, and various findings were obtained after comparing the application with classical soil survey and mapping studies. As a result of the analyzes, it was observed that Soil Data System contributed positively to soil mapping process in many aspects such as accuracy, transparency and time.

## 1. INTRODUCTION

The soil covering the world like a thin carpet is an important natural resource that is the source of life on Earth. The soil, which is composed of air, water, minerals and organic materials, hosts many life forms and directly or indirectly provides the food needs of living beings. Despite all these important functions, unfortunately, soil is not considered as a renewable natural resource (URL 1). Under suitable environmental and climatic conditions, it takes 200 to 400 years for a soil layer of 1 cm to be formed, but the amount of organic matter in the soil is around 3000 years (URL 2).

Housing and food security pressures, improper agricultural practices and unplanned urbanization threaten the soil that plays an important role in providing food to people through agriculture.

Because of this threat, countries aim to use land in the most efficient and efficient way by implementing sustainable land and soil management practices in the main sectors such as agriculture, forestry, reconstruction and environment (FAO 2018).

One of the most important sources used in applications and projects developed to ensure the accurate and sustainable use of land is soil maps (Güler et al. 2016). Soil mapping and related reports produced at the result of soil survey and mapping studies are used effectively in agricultural implementations, forestry activities, zoning plans, environmental management, land planning and management and different engineering branches.

The only soil map covering the whole of Turkey is "Turkish Great Soil Groups" map, which was produced by the General Directorate of Soil and Water in 1965 and until today several updates and

\* Corresponding Author

(fiscan@ktun.edu.tr) ORCID ID 0000 - 0002 - 0669 - 5830  
(erkan\_guler@yahoo.com) ORCID ID 0000 - 0002 - 1865 - 7348

Cite this article

Iskan F & Guler E (2021). Developing a mobile GIS application related to the collection of land data in soil mapping studies. International Journal of Engineering and Geosciences– 2021, 6(1), 27-39

improvement work has been made on. The map of the Turkish Great Soil Groups, which has been used by public institutions and the private sector for many years, has become out of date despite revisions made over the years (Tanrıku 2017). For this reason, many institutions and organizations, especially the public sector, carry out soil mapping studies with their own budgets in order to produce more accurate soil maps and use them in their projects. As most of these soil maps and reports produced by different institutions are not in certain standards and are not stored digitally, data sharing is also very troublesome; thus, it becomes difficult to avoid duplication and to stop wasting resources.

Soil maps are produced by using the characteristics of the soil taken from the plot through the relevant field studies and the sensitivity and accuracy of the soil data collected from the plot directly affect the last product, the soil map. However, in many soil-mapping studies, the data to be used in soil mapping production is not collected or cannot be collected from the plot with sufficient accuracy and sensitivity. For this reason, soil maps that do not reflect the current situation in the field are produced and have negative effects on the projects and works in terms of time, cost and accuracy.

The most important step of soil mapping and survey studies is undoubtedly the field studies. Since field studies are costly and time-consuming process, institutions, organizations and companies try to reach the most accurate data with minimum cost. In particular, some critical problems encountered in soil mapping studies where control is difficult and personnel experience is very important, can be listed as follows.

- ✓ In some field studies, moving the location determined for the profile to different places and collection of the data of different soil types because of not using or misusing the hand GPS.
- ✓ Inaccurate collection of data of soil profiles by unskilled personnel (such as soil moisture, lime and clay layers).
- ✓ Problems caused by the transportation and security of equipment and documents (GPS, camera, printed maps, survey reports, etc.) provided to the field personnel for use in the field (such as time and data loss).
- ✓ Inaccurate or incomplete entry of profile information in the field.
- ✓ Not photographing the profile points according to a certain standard and/or not matching with the correct profiles.
- ✓ Not being able to control the field study simultaneously by the project manager at the office.
- ✓ Not being able to share the data saved in the reports and tables in paper medium with different users and some data losses over time.

Although the advances have been made in the production of soil by means of remote sensing, autonomous soil profile analysis tools and drone techniques in recent years to prevent the problems encountered in soil mapping studies, the soil maps produced with these new techniques and methods don't have the desired accuracy and sensitivity or they increase costs very much.

However, mobile devices such as smartphones, tablet computers, and developing internet infrastructure attract users, especially in the field of faster and more accurate data collection and managing field operations simultaneously. Geographical information systems give opportunity to analyze these data collected from the field in a fast and reliable manner and to produce thematic maps and result reports. The use of GIS and mobile technologies, especially in natural resource mapping, is financially advantageous too (Delibaş et al. 2015).

Today, geographic information systems, remote sensing and web-based mobile applications have been used frequently in many fields such as agriculture, environment and planning (Zelt and Dugan 1993; Tomko 2003; Sood et al. 2015; Marti et al. 2012; Eymen 2019; Dogan and Yakar 2018; Khorrami et al. 2019; Orhan et al. 2019). Geographic Information Systems and mobile data collection systems are used in more and more projects every day in the field of conventional land mapping, especially in the creation of land inventory, the establishment of a soil information system, the mapping of natural resources, and the reduction of cost and time (Weber et al. 2008; Solmaz 2010; Giardino et al. 2010; Lwin and Murayama 2011; Xiaolina et al. 2012; Abdelfattah and Kumar 2014; Sahu et al. 2015; Olyazadeh et al. 2017; Ernst et al. 2019; Iscan and Ilgaz 2017).

In this study, a web based mobile GIS application called Soil Data System, which helps the accurate and transparent collection of soil data from the field in soil mapping and survey studies, and also enables managers to monitor and manage all field studies has been developed.

## 2. MATERIAL and METHOD

### 2.1. Introduction of Study Area

The Abadan Erosion Control Project, which was completed in 2016 within the General Directorate of Forestry of the Republic of Turkey, was selected as the study area. The Abadan Erosion Control Project is a study carried out in 355 ha area within the Abadan neighborhood of the Pursaklar district of Ankara Province in Turkey (Figure 1). The satellite view and the ground view of Abadan Erosion Control implementation area is given in Figure 2 and Figure 3. During the field study phase of the project, 38 soil profile points were opened in the field for the soil mapping and survey section and the related soil reports were filled.

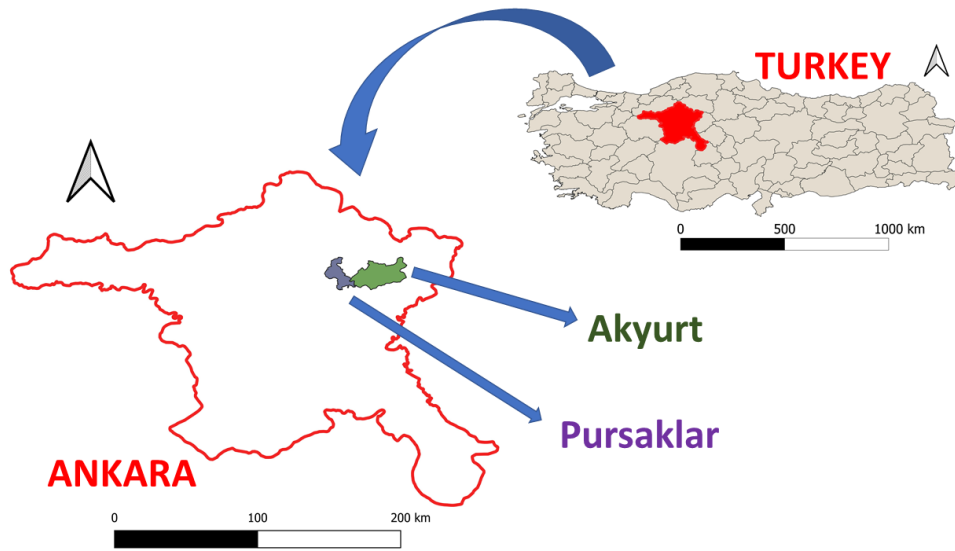


**Figure 1.** Study area

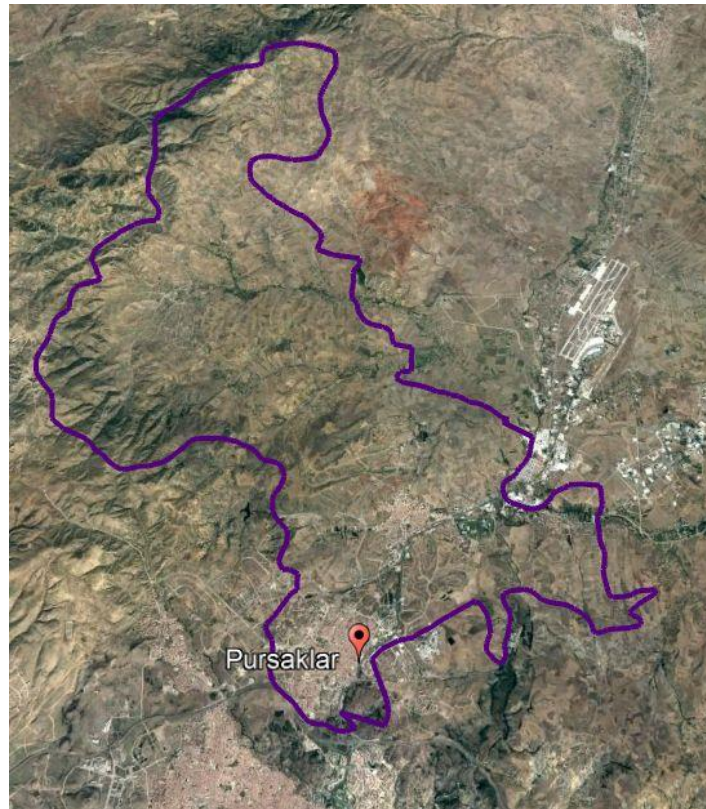


**Figure 2.** Satellite view of Abadan project area



**Figure 3.** Ground view of Abadan project area

## 2.2. Soil Map Production Process

During the soil mapping process, soil samples named as probes or profiles, the locations of which are determined on the map during the preparation phase, are opened in the field at field study and relevant data are collected. The physical and chemical information of soil is obtained from the profile points opened on the ground for use in soil map production. The physical properties of the soil are obtained by observation and some field test kits during the field study and processed in the reports or tables, while the chemical properties are obtained after analysis of the samples taken from the field in the laboratories. Depending on the intended use of the soil map, all profile points can be sampled and sent to the laboratory for analysis, as well as only some amount of soil sample representing the site can be collected and sent to the laboratory. Soil maps are produced in the light of the physical data collected from the field and the results obtained from the soil laboratory.

Although soil maps are produced on the same principle in general, they may differ according to their usage area. Soil analyzes and soil depth sought in a soil map to be used in agriculture are different from those properties required in a soil map to be used in forestry. Although the techniques and technologies used differ, the general lines of the production process of conventional soil maps conducted in particular in agriculture and forestry consists of the following steps;

- ✓ Before the field study, the locations of the profile points to be examined and sampled through the computer or print map are determined in the office. Profile frequency and distribution are determined according to the quality of the study to be performed. The coordinates of these profile points are printed and filed or simply entered into the hand GPS. In the absence of hand GPS, the planned profile points are marked on the map (usually with a 1/25000 scaled topographic map).
- ✓ The number of personnel is determined according to the number and intensity of the profile and the personnel is informed about the site; soil survey reports, maps, cameras (if any) and hand GPS (if any) are delivered to enter the information of profile points.
- ✓ Field personnel go to the field and reach the profile points to which they are responsible, with the help of hand GPS or map. It enters the information about the profile points manually into the study reports and collects the soil samples to be sent to the laboratory for analysis. If the profile points that the coordinates of which are determined in the

office coincide with an unsuitable location in the field such as rivers, buildings and rocky areas, the field personnel shift the position of the profile point on the ground and process the coordinates of the new location on the survey report. The staff also records additional information to be used during the production of the soil map (such as the change boundaries of the soil pattern).

- ✓ After the field study, physical properties of profile points opened in the field are obtained from survey reports and chemical properties are obtained from analysis reports of soil samples sent to the laboratory. Soil map is produced in the light of observation and experience of the personnel in the field and of this information.

## 2.3 Soil Data System

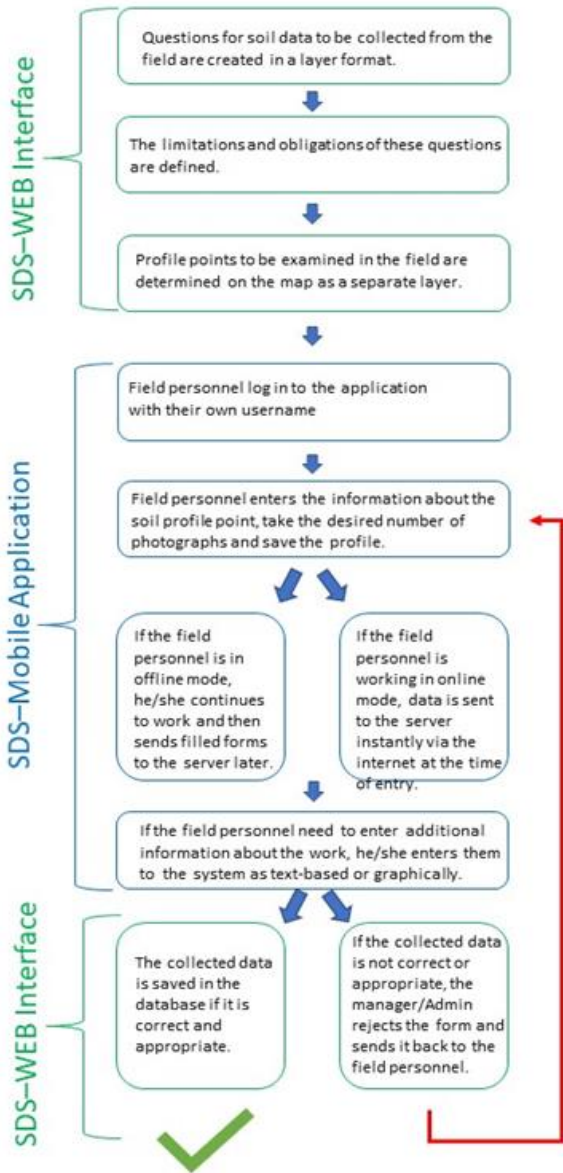
Soil Data System consists of a mobile application operated by Android and a web interface that is integrated with this application. While the mobile application was developed with a focus on the quality of the data collected from the plot, the web interface was designed mostly as admin panel and geoportal (Flowchart 1).

### 2.3.1 Web interface

The Web interface developed within the scope of the study enables project managers to coordinate the field studies conducted for soil mapping and also the authorized users to display via free base maps such as “Bing”, “OpenStreetMap”, “Here” and “Yandex” the field data collected from the plot. All users logging in to the web interface can act within their authority and display maps. For example, a normal user can only see work in a zone where he or she is allowed, or even view land data within his authority while a user with an admin role can create new user accounts and set privileges, while (Figure 4).

Users with administrative authority can create questionnaires of soil data to be collected in the plot via web interface and identify other details such as type of questions, data entry methods on the mobile device (numerical, multiple choice, text based, etc.), sections required to be filled and minimum and maximum number of photos to be taken per profile (Figure 5).

When field teams are online the project manager can monitor on the Web interface simultaneously and intermittently where each staff located is and what data are they collecting. Therefore, the web interface is an important tool for planning and managing soil and land works (Figure 6).



Flowchart 1. Soil data system

### 2.3.2 Mobile application

The Mobile Application was developed on the Android to make it more accessible for users and the development steps to be relatively more practical (Figure 7). The application is designed to work on all mobile devices, such as smartphones and tablets computers, computers with integrated GPS and camera (for photo capture), compatible with Android 5.0 and above.

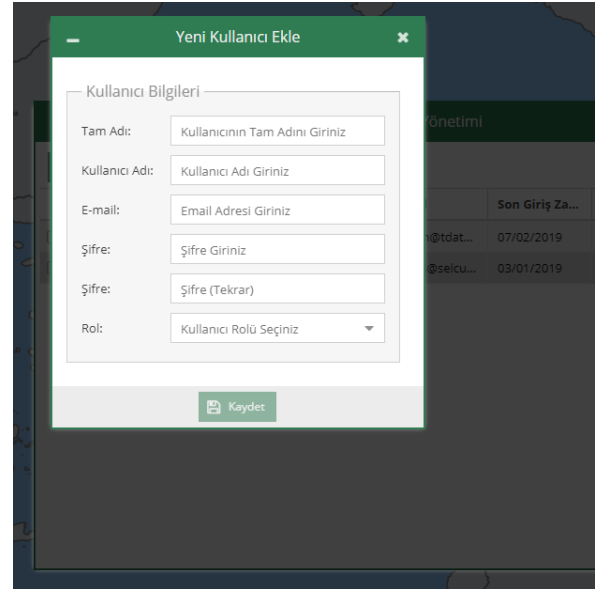


Figure 4. Web interface user creation window

Görünen Ad	Kolon Adı	Tip	Tanım	Benzersiz	Zorunlu	Etiket
Iskelet_Hacim	iskithcim	Çoktan Seçmeli	Iskelet	Hayır	Evet	Hayır
Struktur	struktur	Text		Hayır	Evet	Hayır
Kirec_%	kirec	Çoktan Seçmeli	Kirec	Hayır	Evet	Hayır
Ph	ph__	Double Precision		Hayır	Hayır	Hayır
Kok_Dagilisi	kokdagili	Çoktan Seçmeli	Kok_Dagilisi	Hayır	Evet	Hayır
Arazi_Yuzey_sekli	ays	Çoktan Seçmeli	Arazi_Yuzey_Sekli	Hayır	Hayır	Hayır
Toprak_Derinaligi(M)	td	Çoktan Seçmeli	Toprak_derinaligi(M)	Hayır	Hayır	Hayır
Toprak_derinalik(F)	toprakf	Çoktan Seçmeli	Toprak_Derinaligi(F)	Hayır	Hayır	Hayır
Toprak_Suyu	ts	Çoktan Seçmeli	Toprak_Suyu	Hayır	Hayır	Hayır
Drenaj	drenaj	Çoktan Seçmeli	Drenaj	Hayır	Hayır	Hayır
Humus_Turu	humusturu	Çoktan Seçmeli	Humus_Turu	Hayır	Hayır	Hayır

Figure 5. Web interface - Creation of data fields

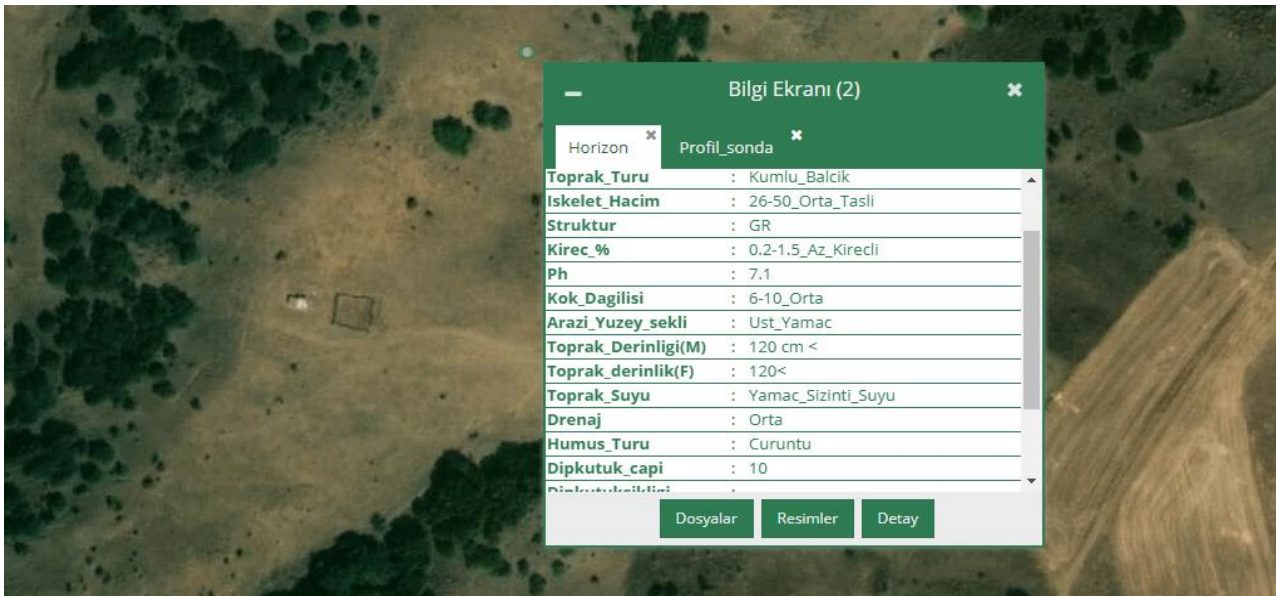


Figure 6. Web interface - Monitoring of collected soil profile data

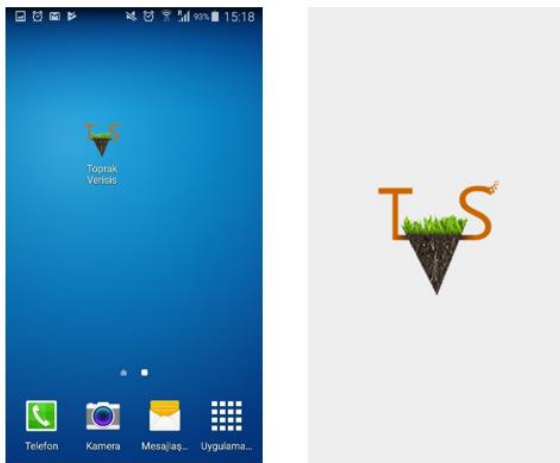


Figure 7. Soil data system – Mobile application short cut and login screen

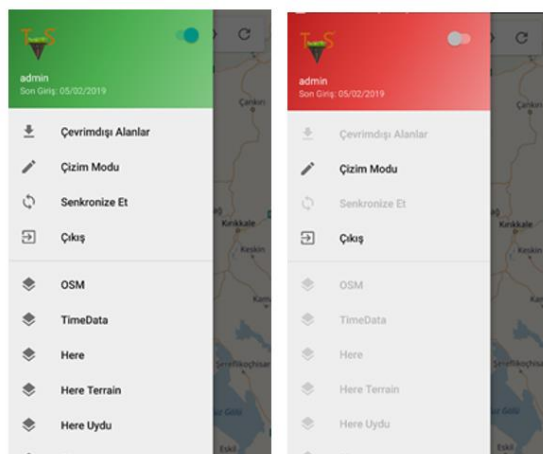


Figure 8. Mobile application online offline mod

During data collection, the mobile application automatically records the coordinates of the profile points with the GPS property of the used mobile device and does not allow the user to interfere. The mobile application can be used online or offline during the fieldwork (Figure 8). When working

online, the collected data are simultaneously transferred to the web interface. In this context, if it is necessary to make changes in the previously formed questionnaires related to the data to be collected from the plot during the field study, the administrator can make the relevant change through the web interface and send it to the mobile application. When the users in the field log off and log in again the system, they can see the updated version of the modified questionnaire that has been sent to the mobile device via the application. In this way, field staff can make necessary corrections related to soil data to be collected while in the field without interrupting the field study.

If the necessity of taking photos during the field work is defined through the web interface, the field staff takes the required amount of photos through the mobile application and these photos are automatically matched with the related questionnaires and transferred to the database and thus to the web interface.

The mobile application supports free map platforms such as “Bing”, “OpenStreetMap”, “Here” and “Yandex” to provide convenience to the users in the field and offers them as a base for users (Figure 9).

In addition to collecting text-based and numerical soil data through the mobile application, users can also create geometric objects such as points, lines and areas on their mobile devices and add feature data to them. The capability, which gives the developed application a mobile GIS feature, enables the more accurate production of soil maps, which are the final product, more accurately, and also helps to add different details such as social problem areas or protected areas related to the study area to the study geometrically (Figure 10).

Since data entry techniques, methods, restrictions and authorities to be made through the mobile application are defined over the Web interface, the user cannot change such settings

through the Mobile application. However, users can enter the web interface and make transactions with

the web browser of mobile devices in the frame of their authority.

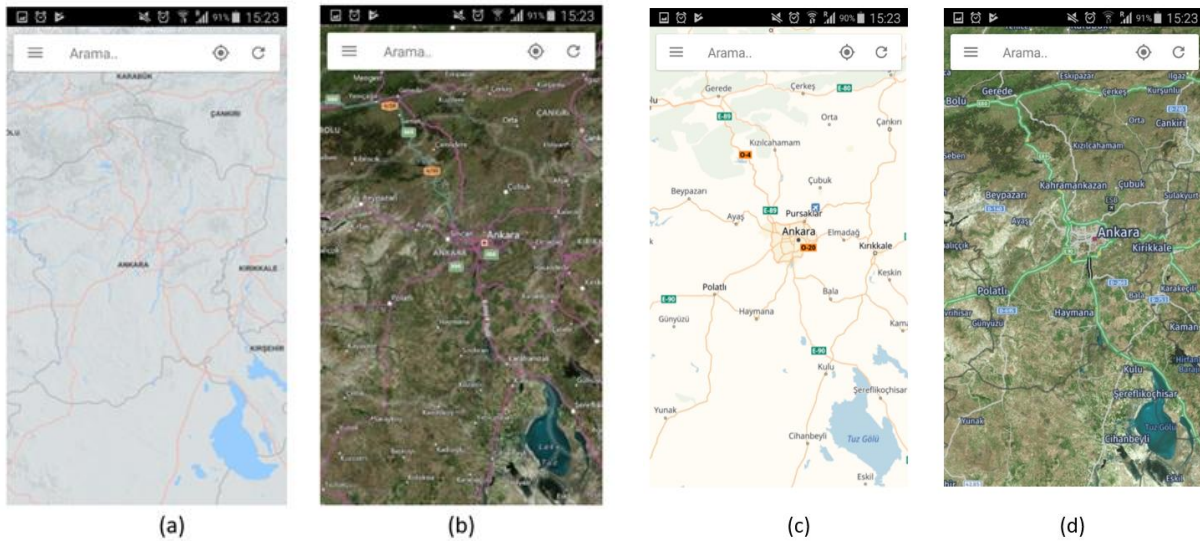


**Figure 9.** Base maps of mobile application (a) Open street map (b) Yandex satellite (c) Yandex map (d) Bing satellite

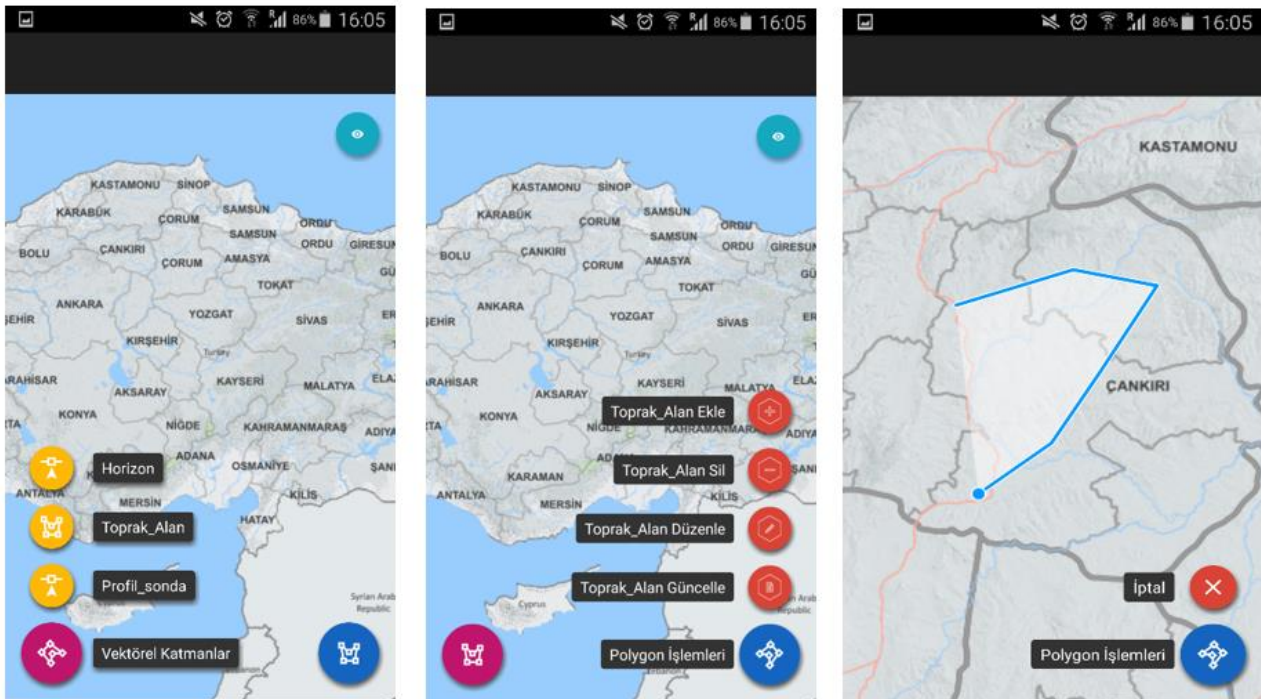


**Figure 10.** Drawing mod of mobile application

### 3. FINDINGS and DISCUSSION

In order to test the Soil Data System which was developed in order to contribute to the soil mapping and survey studies, firstly the copies of the soil survey reports and soil map of the “Abadan Erosion Control Project” were obtained from the project file. The account was created and authorized for the field personnel through the web interface of the Soil Data System. In addition, the questions in soil survey reports of the project were created through the Web interface and the authority and constraints of the

questions were defined. Two interrelated layers were produced in order to facilitate subsequent analysis. (Profil\_sonda and horizon) An independent layer (Toprak Alan) has been created to draw fields and make annotation on the mobile device in the field (Figure 11). Before and during the study, the fieldwork team was contacted for the “Abadan Erosion Control Project” and detailed information was obtained about the field study carried out previously for the project (encountered difficulties, how they are solved, working time, etc.).



**Figure 11.** Soil data system – Layer window

Within the scope of the field study, the profile points opened previously were visited and the profile information was read from the soil survey reports on the paper and entered into the system via mobile device (Figure 12). Since the purpose of this application study is not to test the accuracy of soil profile information but the operation and efficiency of the system, the accuracy of profile and horizon information has not been taken into consideration. Since the time taken for opening the profile point, performing field tests and interpretation would be the same in both methods it was not added to the comparison while entering the profile and horizon information.

In order to compare the soil data entry times of the system developed with the classical method, data entry for each profile was made in two ways. At each profile point, data entry was made with the help of the system developed on the mobile device, and then data entry was made by the conventional method, in other words manually filling the soil survey reports, reading and recording the profile coordinates via hand GPS and taking photographs with a camera. In the field study conducted within the scope of the application study, it took an average of 30 seconds for each soil layer (horizon) to be entered into the Soil Data System via the mobile device. Therefore, it takes 60 seconds for the information of a soil profile with 2 horizons to be entered into the system via mobile device. This time includes photo shooting time too. In order to reapply the conventional soil survey and mapping studies, each soil horizon (layer) information was manually entered into the survey reports in the paper environment and as a result of this process it was observed that the input time of soil data of a horizon was 65 seconds on average. 1 photograph was taken for each horizon and the number and date of the photograph were recorded in a different book for later matching, with an average duration of 30 seconds per horizon. Consequently, the recording time of a profile with two horizons with two photographs was 190

seconds on average. The times obtained in this study are optimal and may vary according to the ability, capability and working conditions of the field personnel.

Due to the previously defined mandatory fields and restrictions through the web interface, there was no information field, in a word, soil data that was forgotten when entering data with the mobile application. Minimum 2, maximum 3 photo rule per profile determined in the office via web interface worked effectively in mobile application, photographs of all profiles were taken and transferred to the system automatically.

The location information (coordinates) of the profile points were received by the GPS feature of the used device and transferred to the server automatically associating to the relevant profile without allowing user intervention. When the user opens a new data entry form at each profile point, the system records the current location information (Figure 13).

Unlike conventional field studies, only mobile devices were used in this field study and documents, equipment such as files, stationery materials, cameras and hand GPS were not required to be carried. This equipment, documents and tools were only used to simulate the classical soil mapping work. Although mobile internet can be used due to mobile phones in the area where the field study is conducted, a part of the study was conducted in offline mode and at the end of the study, all the soil data collected in offline mode was sent to the server at once. The offline mode also has a significant positive contribution to the battery life of the mobile device. During the field study, a staff member with the authority of the manager in the office added 2 additional questions for the purpose of testing, and when the field personnel logged off the application for a few seconds and logged in again, field personnel observed that these new questions were successfully transferred to the device. During the fieldwork, the base maps were successfully loaded when the application was online and the nearby settlements and road information were tracked smoothly through the application, especially for transition to the site, possible emergencies and return. Finally, in the field study, the outer boundary of the project area was drawn by using the location information over the mobile device and some test-purpose information was recorded as attribute information. This area formed on the field was created in "shape file" format and transferred to the map portal automatically. The test-purpose line and point objects have been successfully created in the field and it is seen that all objects in the field can be produced with point, area and line objects when necessary.



**Figure 12.** Profile points on site

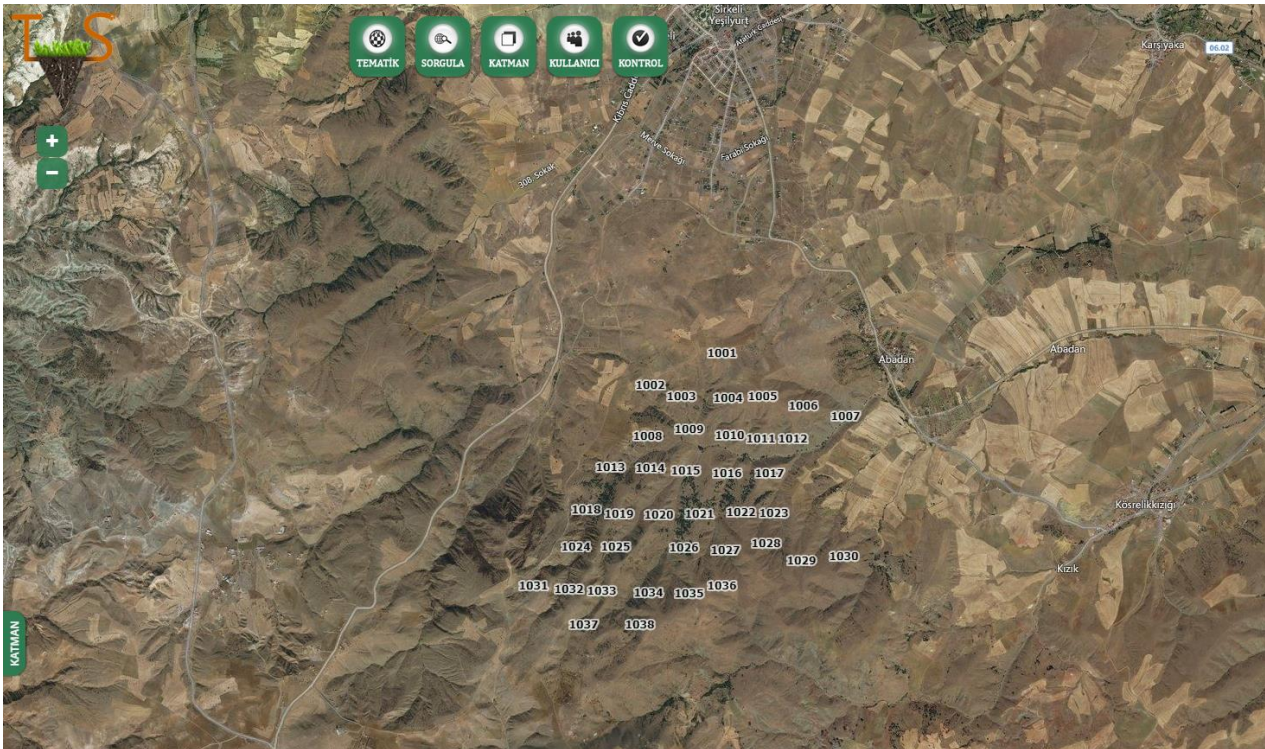


**Figure 13.** Profile points entered into the system via mobile application

According to the findings obtained as a result of the comparison of conventional soil survey and mapping studies with the developed mobile system; first of all, the system gives project managers a serious control opportunity, while providing practicality and rapid mobilization to the field personnel. Since the actual position of the profile points is obtained by the own GPS feature of the device, it could be assured that all profile points were opened in previously planned places since it does not allow external intervention. When the position of the profile point has to be shifted due to field conditions, the new position of the profile point was

automatically saved in the system. In conventional soil mapping studies, field personnel often collect these coordinates from the site, since they have the coordinates of the profile points on the survey reports and the control engineers have no time and opportunity to go to each profile point on the site.

In conventional soil mapping studies, the control engineers or project managers have to accept coordinates of profile point because most of the time they don't have time to go and check all the profile points.

This developed system brings a serious solution to this problem. In particular, the studies carried out

by staying connected to the Internet during the work can be monitored simultaneously by the project manager or control engineer, thus correcting errors or deficiencies during fieldwork.

In the system, which was developed in place of the equipment and devices such as paper/printed maps, soil survey reports and charts, cameras, hand GPS used in conventional soil mapping studies, only one mobile device (smart phone) and mobile power supply (Power bank) were used. These equipment and devices used in conventional soil mapping work lay a serious burden and responsibility on field personnel in the later hours of field work. In particular, if the soil surveys and report on the paper environment where the profile information is entered cannot be brought to the office environment in full, it is necessary to go back to the field in order to complete the soil mapping study. While moving back to the field has a very negative impact on morale and motivation for the whole team, it is also a waste of time and cost. Through the Soil Data System, all data is transmitted to the server and thus to the control engineer or project manager without any burden on the user wherever there is internet access (mobile internet or WIFI),

The mobile application of the Soil Data System requires an Internet connection for a few seconds at the first login only to withdraw the user's authorization and identification from the server. After logging in the application with the user name and password, can be worked offline (in offline mode) until the end of the operation. This feature has been added to the application by considering the fact that many regions where soil surveys are conducted are in forested and agricultural areas away from the city centers. Another advantage of offline operation is the capability to use the battery of the mobile device more economically. In the studies that are more sensitive and project manager guidance is required, field staff may be asked to work online and field data sent to the server while the staff is in the field will be reviewed simultaneously by the control engineer or project manager and if necessary, some soil profile surveys may be required to be redone.

In many soil mapping and survey studies, it is not obligatory to take photographs of the pits of the soil profiles and their surroundings. In the studies that photograph is obligatory, photographs are taken with cameras or mobile phones, which can lead to transfer, storage and photo-profile matching problems. Thanks to the application developed, it is possible to make photo of the profiles obligatory and define the upper and lower limitation for the number of obligatory photographs per horizon. The taken images are encoded by the software and assigned to the corresponding profile automatically. In this way, there will be no need to carry out operations such as matching or naming images with profiles and each profile in the system will be kept with its own photographs. The project manager or control engineer may define some rules over the system depending on the type or region of the work

performed (4 pieces for north, south, east and west directions, 2 for each horizon to see the general structure of the area, etc.). These profile photographs can be displayed on the map along with other soil features.

Soil maps are produced with the profile data opened in the field and analysis reports from some samples and observations made in the field and generally strengthened with experience. Profile information and analysis reports are documented in a way, even on paper, but it is not easy to graphically document the observation in the field. With the help of the mobile application developed, it is possible to produce the information to be used as vector in soil map production such as pattern changes on the surface of the field, topographic ridges and geological changes, and attribute information of these graphical data can be entered if desired. In the field study, the field personnel drew a draft soil map during the study, entered various attribute data and sent it to the main server over the internet along with the other data. These data are not permanent and are only produced to support the soil map production process and can be exported in "shape file" or "Kml" format if desired.

When comparing the soil map of Abadan Erosion Control Project produced with the classical methods and the mobile application of the Soil Data System and the draft map drawn in the field by hand, the project boundaries overlap to a great extent, which in turn contributes greatly to the soil map production process in terms of accuracy and speed (Figure 14 and Figure 15).

In addition to the many advantages of the Soil Data System, it can be shown that the charging of the mobile device used as a disadvantage is not sufficient for field works. Today, there are also mobile devices with very strong battery capacity, but the cost of these devices is considerably high. In order to eliminate this disadvantage, backup power supplies (power bank), which are also included in the fieldwork, can be used. However, the device's backup battery or a backup mobile device with the Mobile application installed may be available. Since the data resides on the main server, closing and opening the mobile application in the field or continuing to collect data with another mobile device with the same user name does not affect the operation. The fact that the Soil Data System is completely electronic can be considered as a disadvantage. It may be complicated to use, especially for middle-aged and older users. Project managers may solve this problem by optimizing the system according to the skills of the personnel they own or by providing the necessary training.

According to the data obtained at the end of the application study, it took about 3 times longer to record the data of a soil profile point with 2 horizons, including 2 photo shoots (one photo per horizon) than the Soil Data System mobile application in the classical method. In the classical method, the data is manually entered into the soil survey reports on

paper and then the data must be re-entered into the related software during the map production process and the photographs taken per profile should be transferred to the computer, considering all these

processes, the time taken to transfer the data collected from the field to a digital medium is much longer.

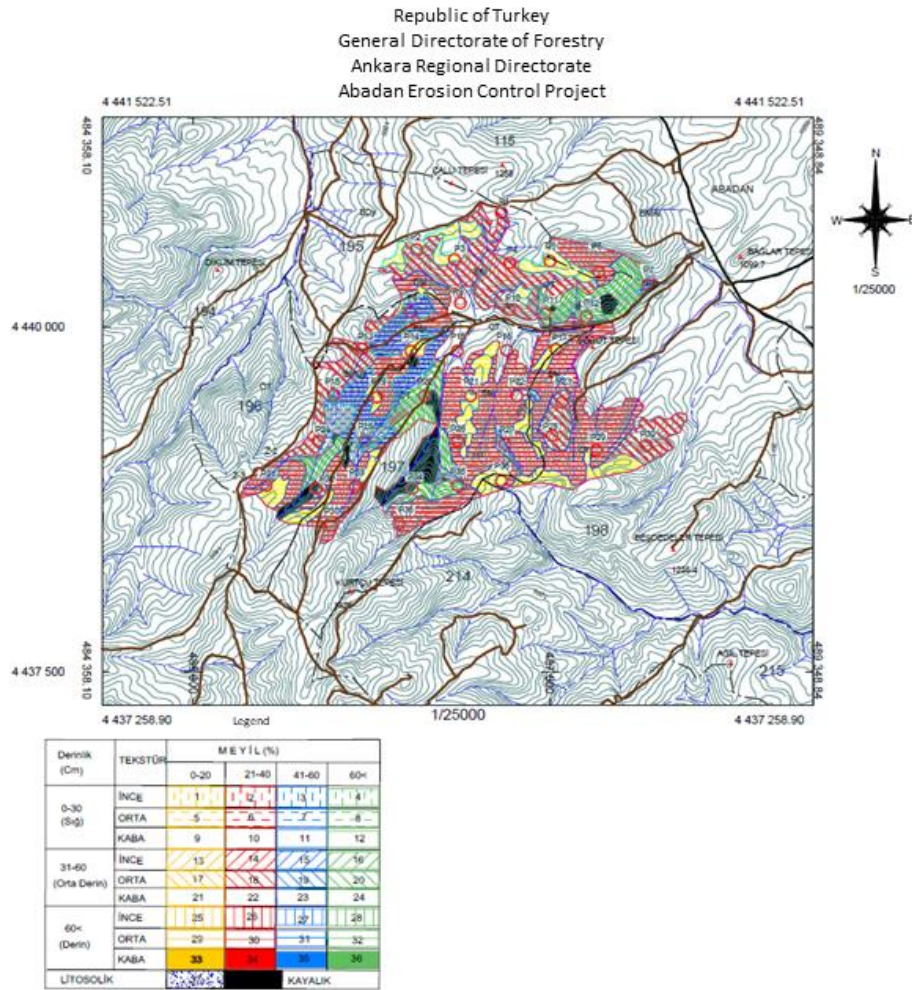


Figure 14. Soil map produced by classical methods

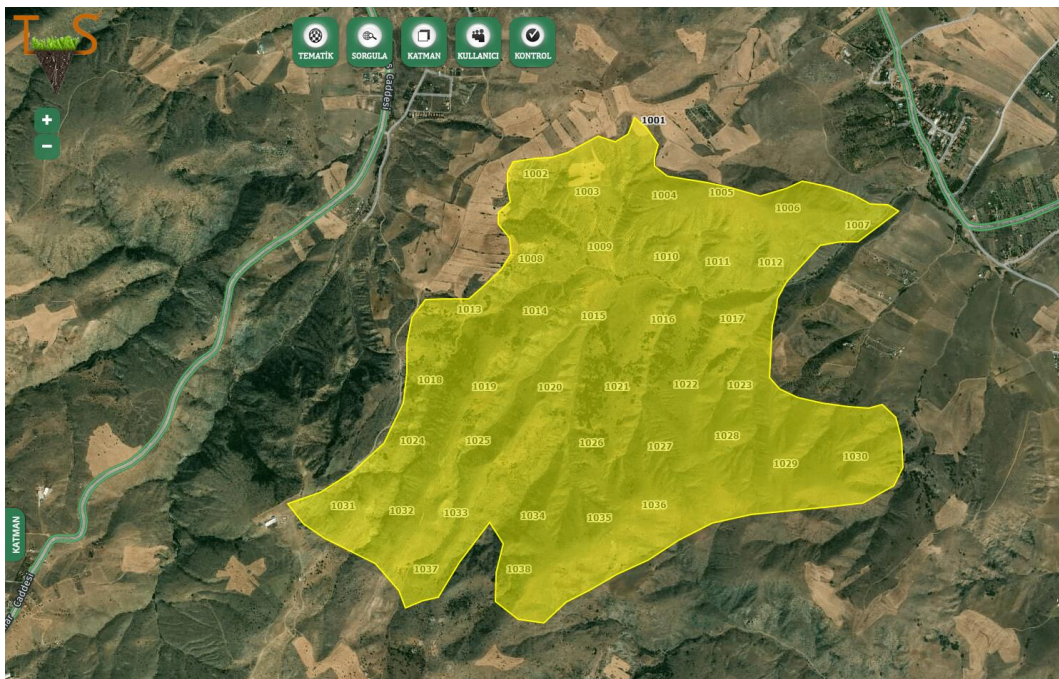


Figure 15. Project area created in the field via mobile application

#### 4. CONCLUSION and PROPOSALS

Soil Data System has been developed with the aim of increasing the accuracy of soil data collected from the field in soil survey and mapping studies, ensuring coordination in field surveys conducted for soil survey studies and supporting the production of highly accurate soil maps as a result product. With the results of analysis of these systems and laboratories, the final soil map can be produced faster and more economically. Soil Data System also provides the opportunity to make more systematic and organized soil mapping studies in the field.

Today, the age range of mobile device usage, especially on smart phones, has widened due to the reasons such as ease of internet access, connection speeds, the introduction of mobile devices for almost every segment, the desire of people to access information without losing their mobility and increasing the power of social media. Since this mobile equipment owned by the Soil Data System users is developed in accordance with the internet connection and mobile application habits, the adaptation time of the users to the system is very short, which makes a positive contribution to conducting the soil survey and mapping studies carried out in a more effective manner.

The Soil Data System has been developed in the Android operating system, which is used on more mobile devices and can be accessed relatively easily by users. In order to reach more users, it is useful to adapt the system to other mobile platforms such as IOS and Windows Mobile that have considerable users. In addition, the installation of the mobile application of the system to the application markets of these platforms (Google Playstore, Appstore etc.) to be presented to users and updates to the software to be delivered to users through these mobile markets will be positive in terms of accessibility of the Soil Data System.

It is very important that this system, which is closely related to current technological developments, does not lose its actuality. In this context, continuous monitoring of hardware innovations and updates in mobile operating systems and adapting the developments to the benefit of the users will enable the Soil Data System to remain up to date and continue to contribute to soil survey and mapping studies.

Soil Data System; will contribute positively to the rapid, transparent and accurate production of soil maps that will provide base and support to many projects such as protection of biodiversity and increase of forest asset especially food safety, which is carried out and will be carried out for the purpose of conservation, efficient use and transportation of the soil to the future. In addition, it could also be an important model for the data sharing problem among institution with GIS compliant standard soil data production.

#### ACKNOWLEDMENT

This paper is supported by Selcuk University Coordinating Office of Scientific Research, Project Nr. 17201123.

#### REFERENCES

- Abdelfattah M A & Kumar A T (2015). A web-based GIS enabled soil information system for the United Arab Emirates and its applicability in agricultural land use planning. *Arabian Journal of Geosciences*, 8, 1813-1827.
- Delibaş L, Bagdatlı M C & Danisman A, (2015). Determined appropriate area of walnut analyzing properties of some soils using Geographic Information Systems (GIS): The case of Central Village Tekirdag Province, Gümüşhane University Journal of Science and Technology Institute, 5 (1): 50-59, (in Turkish)
- Dogan Y & Yakar M (2018). Gis and three-dimensional modeling for cultural heritages. *International Journal of Engineering and Geosciences*, 3(2), 50-55. DOI: 10.26833/ijeg.378257
- Ernst F, Erdogan S & Bayram Y (2019). Human Resource Management Using Geographic Information Systems (Gis): An Example from Turkish Land Registry Directorates, *International Journal of Engineering and Geosciences*, 4(2), 71-77. DOI: 10.26833/ijeg.450571
- Eymen A (2019). Determination of potentially irrigable agricultural lands using remote sensing and geographic information system: case study of Yamula Basin, *International Journal of Environmental Science and Technology*, 16(1), 5101-5106.
- FAO (2018). *The Future of Food and Agriculture - Alternative Pathways to 2050*. Rome: Food and Agriculture Organization of the United Nations
- Giardino M, Perotti L, Carletti R & Russo S (2010). Creation and test of a mobile GIS application to support field data collection and mapping activities on geomorphosites. *Mapping geoheritage*, 35, 115-127.
- Güler E, Doğan A & Orhan C, (2016). *Soil Information Systems in Republic of Turkey* Ministry of Forestry and Water Affairs, EuroSoil International Congress, 17-22 July, İstanbul.
- Iscan F & Ilgaz A (2017). Analysis of Geographic/Urban Information System Web Presentations of Local Governments in Turkey, *International Journal of Engineering and Geosciences*, 2(3), 75-83. DOI: 10.26833/ijeg.317088
- Khorrami B, Gunduz O, Patel N, Ghoulane S & Najari M (2019). Land surface temperature anomalies in response to changes in forest cover. *International Journal of Engineering and Geosciences*, 4(3), 149-156. DOI: 10.26833/ijeg.549944

- Lwin K K & Murayama Y (2011). Web-Based GIS System for Real-Time field data collection using a personal mobile phone. *Journal of Geographic Information System*, 3(4), 382-389. DOI:10.4236/jgis.2011.34037
- Marti G I, Rodriguez E L, Benedito M, Trilles S, Beltran A, Diaz L & Huerta J (2012). Mobile Application for Noise Pollution Monitoring through Gamification Techniques. *International Conference on Entertainment Computing - ICEC 2012*, 562-571, 26-29 September, Germany.
- Olyazadeh R, Rieux S K, Jaboyedoff M, Derron M H & Devkota S (2017). An offline-online Web-GIS Android application for fast data acquisition of landslide hazard and risk. *Natural Hazards and Earth System Sciences*, 17(4) 549-561. DOI:10.5194/nhess-17-549-2017
- Orhan O, Dadaser-Celik F & Ekercin S (2019). Investigating Land Surface Temperature Changes Using Landsat-5 Data And Real-Time Infrared Thermometer Measurements At Konya Closed Basin In Turkey. *International Journal of Engineering and Geosciences*, 4(1), 16-27. DOI: 10.26833/ijeg.417151
- Sahu N., Reddy G P O, Kumar N, Ngaraju M.S.S., (2015). High resolution remote sensing, GPS and GIS in soil resource mapping and characterization-A Review. *Agricultural Reviews*, 36(1), 14-25.
- Solmaz İ M (2010), Development of new methods for detailed soil mapping on sloping lands using geographic information systems and remote sensing techniques. PhD Thesis, Cukurova University, Graduate School of Natural and Applied Science, Adana (in Turkish)
- Sood K, Singh S, Rana R S, Rana A, Kalia V & Kaushal A (2015). Application of GIS in precision agriculture. National seminar on "Precision farming technologies for high Himalayas" 04-05 October, India.
- Tanrikulu M (2017). Soil survey-mapping studies in Turkey and Harvey Oakes. *Akademik Bakış*, 64, 664-678. (in Turkish).
- Tomko M (2003). Spatial databases for Mobile GIS Applications, Master Degree Thesis, Slovak University of Technology, Bratislava
- URL 1. Soil: A Nearly Non-Renewable Resource, <http://sciencenetlinks.com/daily-content/4/19/>, Access Date: 20.10.2019
- URL 2. Soil Formation, [http://www.eniscuola.net/wp-content/uploads/2011/01/pdf\\_soil\\_2.pdf](http://www.eniscuola.net/wp-content/uploads/2011/01/pdf_soil_2.pdf), Access Date: 18.10.2019
- Weber E, Hasenack H, Flores C A, Pötter R O & Fasolo P J (2008). GIS as a Support to soil mapping in Southern Brazil. *Digital Soil Mapping with Limited Data*, 103-112, Springer, Amsterdam.
- Xiaolina L, Linnan Y, Lin P, Wengfeng L & Limin Z (2012). County Soil Fertility Information Management System Based on Embedded GIS. *Procedia Engineering*, 29, 2388-2392.
- Zelt R B & Dugan T J (1993). Simulation and Mapping of Soil-Water Conditions in the Great Plains, *Water Resources Bulletin*, 29(6), 939-948.



© Author(s) 2021.

This work is distributed under <https://creativecommons.org/licenses/by-sa/4.0/>



## Intelligent mapping of irrigated areas from Landsat 8 images using transfer learning

Zouhair Benbahria <sup>\*1</sup>, Imane Sebari <sup>2</sup>, Hicham Hajji <sup>2</sup>, Mohamed Faouzi Smiej <sup>1</sup>

<sup>1</sup>Royal Center for Remote Sensing, Rabat, Morocco

<sup>2</sup>School of Geomatics Sciences and Surveying Engineering, IAV Hassan II, Rabat, Morocco

### Keywords

Irrigated areas mapping  
Landsat 8  
Deep learning  
UNet  
ResNet50

### ABSTRACT

The lack of reliable and up-to-date data in developing countries is a major obstacle to sustainable development. In Morocco, where groundwater withdrawals by farmers are very intensive and informal, maps describing and monitoring the extension of irrigated areas are scarce and labor-intensive to obtain. In this paper a novel transfer learning algorithm is proposed to map irrigated areas at different stages of an agricultural cycle from Landsat 8 images. The results obtained displays satisfactory performance over traditional machine learning algorithms. On a small dataset, we initially tested three well known deep learning architectures (SegNet, DenseNet and Unet). The results obtained were not satisfactory. So, to get high performance, we rely on a transfer learning architecture combining UNet with ResNet50 backbone (trained on 2012 ILSVRC ImageNet dataset) as a baseline after a phase where different configurations were tested. In the first part of this study, we compared the use of three optimization methods: Adam and two variants of Stochastic Gradient Descent (SGD) associated with two techniques (Cyclical Learning Rate and Warm Restart) to find the optimal learning rate and then test the impact of data augmentation on the overall accuracies. Data augmentation had improved the overall accuracy for the three methods. Adam based method from 94% to 97% with mean IoU of 0,79 (for all land cover classes) and 0,86 for irrigated areas class. For SGD based methods, the overall accuracy had increased from 91% to 94% with mean IoU of 0,75 (for all land cover classes) and 0,82 for irrigated areas class. As we are interested in having irrigated areas maps at different key periods of the agricultural cycle, we also explored, in the second part of this study, the temporal generalization of the best model.

## 1. INTRODUCTION

Deep learning (DL) is significantly impacting areas of research, including computer vision, image processing, and remote sensing (Ball et al., 2018) thanks to the increased availability of data and computational resources (Zhu et al. 2017).

Generally, traditional deep networks (DN) are trained using large datasets of imagery. However, in remote sensing the ones available are typically very limited (Ball et al. 2018). In such low to medium learning datasets contexts, some architectures like

UNet and SegNet networks are frequently privileged (Younis and Keedwell 2019).

Fortunately, open high-resolution satellite imagery, such as from USGS and Copernicus, is becoming increasingly available. Such imagery can be used to extract useful insights to inform policy decisions in water resources management and feed datasets for training new deep learning architectures.

In this paper, we examine one of the different approaches used to address the lack of training data which are: 1) Unsupervised learning 2) Generative

### \* Corresponding Author

(benbahria@crts.gov.ma) ORCID ID 0000 - 0003 - 4326 - 1369  
(imane.sebari@gmail.com) ORCID ID 0000 - 0002 - 6754 - 8404  
(hajjihi@gmail.com) ORCID ID 0000 - 0001 - 9026 - 8980  
(smiej@crts.gov.ma) ORCID ID 0000 - 0002 - 1644 - 5819

### Cite this article

Benbahria Z, Sebari I, Hajji H & Smiej M F (2021). Intelligent mapping of irrigated areas from Landsat 8 images using transfer learning. International Journal of Engineering and Geosciences, 6(1), 40-50

adversarial networks (GANs) 3) Transfer learning (Ball et al. 2018) which is still an active research area in remote sensing according to Tuia et al. (2016).

The goal of the next sections is to provide a brief overview of some existing architectures based on DN and the specific objectives of this study.

### 1.1 Deep Learning Approaches for Semantic Image Segmentation

DL architectures have been successfully applied to pixel-based classification of high-resolution satellite images outperforming standard image classifiers. It has been shown that it can achieve far better classification performances (Zhu et al. 2017; Liu et al. 2018).

Despite the lack of training data, Deep networks have proven to outperform at extracting mid- and high-level abstract and discriminative semantic features from images. Recent studies indicate that the feature representations learned by CNNs are greatly effective in semantic segmentation (Long et al. 2015; Khryashchev et al. 2018).

LeNet-5 is the reference structure of a CNN. It was developed by (LeCun et al. 1998). It consists of two convolutional layers followed by three fully connected layers.

Semantic image segmentation is defined as the task of clustering parts of image together which belong to the same object class (Thoma 2016).

So, to produce a land cover map, well known and deep architectures as SegNet, DenseNet and UNet can be used. The latter has received a lot of interest initially for the segmentation of biomedical images using a reduced dataset but then for a lot of applications in remote sensing (Igloukov et al. 2017; Feng et al. 2019).

UNet architecture (Ronneberger et al. 2015) is like a convolutional autoencoder. It uses skips

connections (Figure 1) to reinject the features maps of the encoder part into the decoding phase and also transposed convolutions to reconstruct the original image resolution. These approaches use CNN's pretrained convolutional layers for classification, including VGG-16, as the encoder. The advantage of these symmetric approaches is that they can generate predictions at the same spatial resolution as the input image.

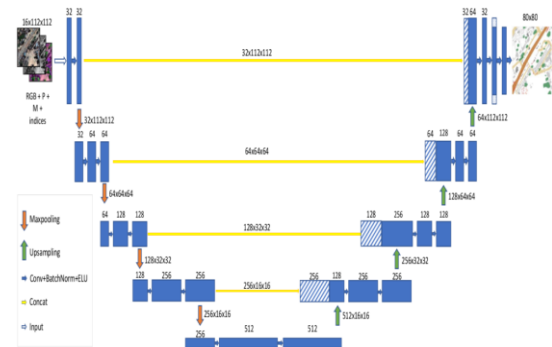


**Figure 1.** Customized UNet architecture for satellite image segmentation (Vooban 2017)

In addition, given the better performance of the ResNet and DenseNet models in object recognition, researchers also tried to adapt these architectures for semantic segmentation. Thanks to the increase in GPU computing capacities (Wu et al. 2016) proposed a first approach for ResNet.

Recent research works have shown that deeper architectures, such as deep residual networks ResNets (He et al. 2016) can gain accuracy from increasing the depth of the network. These residual networks 1) are substantially deeper (Table 1) 2) have fewer parameters 3) are easier to optimize, and 4) can gain accuracy from considerably increased depth (Bilinski and Prisacariu 2018).

**Table 1.** ResNet (50 and 152 layers) architectures for ImageNet (He et al. 2016)

Layer name	Output size	50-Layer	152-layer
Con1	112*112	7x7, 64, stride 2 3 x 3 max pool, stride 2	
Conv2.x	56*56	$\begin{pmatrix} 1 \times 1, & 64 \\ 3 \times 3, & 64 \end{pmatrix} \times 3$	$\begin{pmatrix} 1 \times 1, & 64 \\ 3 \times 3, & 64 \end{pmatrix} \times 3$
Conv3.x	28*28	$\begin{pmatrix} 1 \times 1, & 128 \\ 3 \times 3, & 128 \end{pmatrix} \times 4$	$\begin{pmatrix} 1 \times 1, & 128 \\ 3 \times 3, & 128 \end{pmatrix} \times 8$
Conv4.x	14*14	$\begin{pmatrix} 1 \times 1, & 256 \\ 3 \times 3, & 256 \end{pmatrix} \times 6$	$\begin{pmatrix} 1 \times 1, & 256 \\ 3 \times 3, & 256 \end{pmatrix} \times 36$
Conv5.x	7*7	$\begin{pmatrix} 1 \times 1, & 512 \\ 3 \times 3, & 512 \end{pmatrix} \times 3$	$\begin{pmatrix} 1 \times 1, & 512 \\ 3 \times 3, & 512 \end{pmatrix} \times 3$
FLOPs	1*1 3.8*10 <sup>9</sup>	Average pool, 1000-d fc, softmax 7.6*10 <sup>9</sup>	11.3*10 <sup>9</sup>

Also, a fully convolutional version of the DenseNet (Jégou et al. 2017) has also been proposed for semantic segmentation by combining an encoder-decoder approach with UNet inspired activation passing.

In SegNet, (Badrinarayanan et al. 2017) the authors proposed a convolutional encoder-decoder architecture for image segmentation. Similar to the deconvolution network. It consists of an encoder network, which is topologically identical to the 13

convolutional layers in the VGG16 network, and a corresponding decoder network followed by a pixel-wise classification layer.

Fully convolutional network (FCN) approaches for semantic segmentation of remotely sensed images have become much more popular. FCNs infer a pixel prediction for the entire image in a single pass, avoiding as well the problem of the classification per patch. This drastically reduces computation times without requiring unsupervised pre-segmentation.

Generally, deep learning methods using FCN have emerged in few years as the new state of the art for many remote sensing image interpretation tasks (Liu et al. 2019) and UAV images as well (Figure 2).

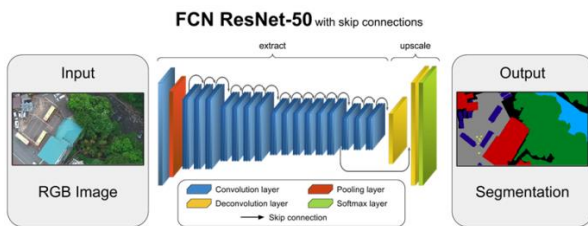


**Figure 2.** UAV image segmentation using ResNet 50 architecture

## 1.2 Related Works

The first applications of FCN on optical aerial data appear many years ago (Paisitkriangkrai et al. 2015; Sherrah 2016). Since (Mnih 2013) where authors tried using FCN for the extraction of roads and buildings in aerial images from image patches, these approaches have been successfully used on many Very High-Resolution satellite data (Lagrange et al. 2015).

In (Papadomanolaki et al. 2016), the authors used Convolutional Neural Networks (CNN) for the classification of SAT-4/SAT-6 dataset given by US National Agriculture Imagery Program. They compared different deep architectures (AlexNet, VGG, etc).

Some researches (Xu et al. 2018; Iglovikov et al. 2017) start from UNet based and adapted architectures to extract buildings, urban patterns and other land cover classes from satellite images.

Also, in (Audebert et al. 2016; Audebert et al. 2017) the authors train variants of the SegNet architecture on remotely sensed imagery over an urban area. The goal was to study different strategies to have an accurate semantic segmentation.

For hyperspectral image (HSI), Lin et al. (2013) introduced, for the first time, the concept of deep learning in a new framework of spectral-spatial feature extraction.

(Pirotti et al. 2016), by using mainly ESA and USGS free images, benchmarked 9 machine learning algorithms (Random Forest, SVM and Neural Networks...etc.). These models were tested for accuracy and speed in training and classification of land-cover classes in a Sentinel-2 dataset.

Research on semantic segmentation includes some works that deal with training data scarcity as in our paper. (Acquarelli et al. 2018) proposed, in the case of lacking training data, a convolutional neural network with a single hidden layer that can achieve state-of-the-art performance by using three tricks: a spectral-locality-aware regularization term, smoothing and label-based data augmentation.

(Vooban 2017; Jiang 2017) used only 25 labelled satellite images for training. While (Younis and Keedwell 2019) modified the structure of SegNet architecture (Figure 3) and train it using 6 RGB images. The results of this study were also promising.

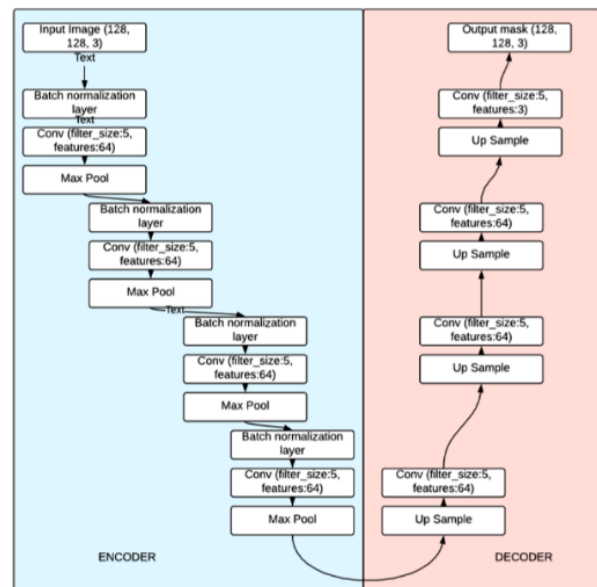


**Figure 3.** SegNet adapted architecture to semantically segment satellite data (Younis and Keedwel 2019)

As we mention before, transfer learning can be used as solution to fine-tune pretrained networks based on a small training dataset. This is possible thanks to transfer learning which seeks to learn from one area to another (Tuia et al. 2016). It can improve the learning process of a target predictive function from a knowledge-based source predictive function (Pan and Yang 2010).

Working on new target domain, two options for transfer learning can be explored (Ghazi et al. 2017). Using completely a pre-trained network to learn new features or fine-tune its weights.

Generally, most remote sensing-based transfer learning works are focused on updating the weights of a DL solution from another context to the current task based on available training data.

In (Yang et al. 2016) the authors used dual CNNs and transfer learning as inputs to a fully connected layer for classification. Lower and middle layers were trained on external dataset whereas the top layers were trained on the available training samples.

(Othman et al. 2016) used transfer learning architecture trained on the ILSVRC-12 dataset. The

trained system was next applied to the UC Merced Land Use and Banja-Luka datasets.

The nature of used mapping approaches by machine learning made it necessary to invest a lot of effort in training the models. In (Wurm et al. 2019) the study seeks to analyze transfer learning capabilities of FCNs to slum mapping in various satellite images. A model trained on very high-resolution optical satellite imagery from QuickBird is transferred to Sentinel-2 and TerraSAR-X data.

Recently, advanced methods based on domain-specific transfer learning are proposed for semantic segmentation of remote sensing data. Panboonyuen et al. (2019) proposed a novel CNN called global convolutional network (GCN) which can capture different resolutions by extracting multi-scale features from different stages of the network.

In summary, automated land cover mapping based on satellite image is a great source of information for many fields such as land management, forestry, agriculture and so on. In Morocco, where groundwater withdrawals by farmers are very numerous and informal, the need for information on the location of irrigated areas rises up as a strategic objective.

Studies on the use of remote sensing for mapping irrigated areas in Morocco are uncommon. In (Merdas et al. 2015) we used low-resolution data (MODIS) and a time series of NDVIs to map irrigated areas using a pixel-based approach (86.29% of well-classified pixels). This study was based on previous studies (Ozdogan et al. 2010). In (Benbahria et al. 2018), a new automatic mapping framework was proposed based on Landsat 8 (L8) time series images and using pixelwise classification Random Forest algorithm.

(Zhang et al. 2018) tested an approach based on well-known image classification convolutional neural networks to automatically detect only center pivot irrigation systems from Landsat 5 TM images.

Our main objective, in this paper, is to evaluate recent Transfer Learning approaches and Semantic Segmentation to monitor the extension of irrigated areas at different stages of an agricultural cycle.

As a preliminary step, we experimented known deep learning architectures as SegNet, DenseNet and UNet with our train dataset and then a transfer learning architecture combining UNet with ResNet50 as backbone. Three specific objectives are set:

- ✓ To compare the use of three optimization methods (Adam and two variants of Stochastic Gradient Descent (SGD)).
- ✓ To evaluate the impact of data augmentation on the overall accuracies of the three methods.
- ✓ To assess the temporal generalization of the model to imagery collected at different times and under different atmospheric conditions (in the same agricultural cycle).

## 2. STUDY AREA and DATA

### 2.1 Study Area

Experiments are conducted in Gharb site which is located in the north-west of Morocco (Figure 4). It currently counts 190 000 ha irrigated area. About 80 % of the rains are concentrated between November and April. The dry period is usually between June and September.

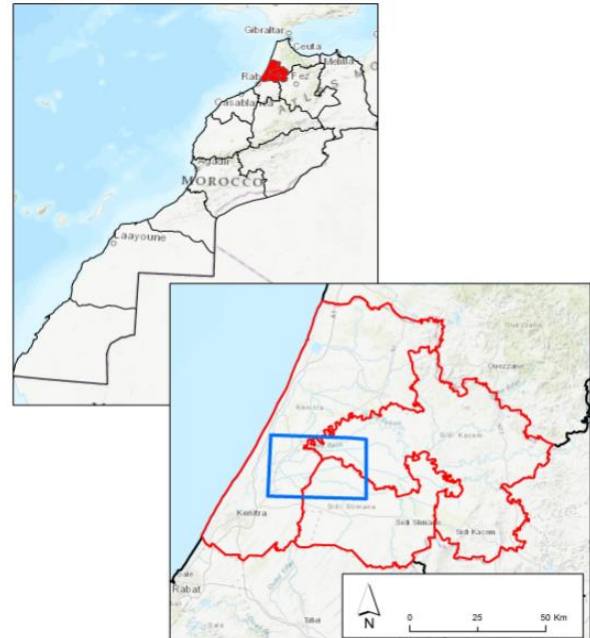


**Figure 4.** Study area localization (blue rectangle) (© Open Street Map).

### 2.2 Used Data

Three L8 cloud free scenes (October 2015, May and August 2016) were acquired and pre-processed. The choice is based on three key periods in the agricultural cycle (Autumn, Spring and Summer).

In addition to RGB (R = NIR, G = R, B = G) L8 images, ground truth data are collected and used for learning and validation.

For collecting reference data, Corine Land Cover (CLC) based classification scheme is used by adapting it to the Moroccan context. Seven (7) classes were selected (Table 2) to appear in the final land cover maps.

**Table 2.** Classification scheme for Gharb region

Code	Land cover
0	Impervious
1	Forest
2	Water
3	Arable land
4	Irrigated land
5	Greenhouse
6	Orchard

The training image dataset includes 50 images (128x128 pixels each with 3 channels (NIR, R, G))

with corresponding ground truth masks. The ground truth was collected by photointerpretation of the images and existing recent data (Ortho-images SPOT6 and 7 with 1.5m resolution and Google Earth).

For testing the models, initially three datasets of ten manually labelled images were prepared and then augmented to make tests on 100 images for each period of the agricultural cycle.

### 3. METHODOLOGY

#### 3.1 Data Preparation

L8 images were pre-processed through the following steps: 1) Converting DN of bands (B3 = Green, B4=Red, B5=NIR and B8=Panchromatic) into reflectance (ToC) by applying DOS atmospheric correction, 2) Apply a Pan-sharpening using Brovey Transform (Johnson et al. 2012), and 3) Stacking the three pansharpened bands (B3, B4 and B5).

From the first image, we extracted well distributed 50 patches (128x128 pixels each with 3 channels (NIR, R, G)) covering all land cover classes. These patches were photo-interpreted and the vector results were converted to raster masks. Finally, all the generated images were resized to 224x224 to be suited for the training and validation of the experimented DL architecture (UNet with ResNet50 as backbone).

#### 3.2 Evaluating Deep Learning Architectures for Irrigated Areas Mapping

Although it has not been designed specifically for satellite images, UNet architecture is increasingly applicable in remote sensing. As we will explain later, we use this structure as a base reference but combined with ResNet.

In this paper, due to the limited training dataset, we tested a UNet based transfer learning architecture (Yakubovskiy 2018) to perform land cover semantic segmentation of L8 images.

Our multi class segmentation is based on UNet with ResNet50 backbone (which has weights trained on 2012 ILSVRC ImageNet).

In the first part of this study, this architecture was experimentally assessed through three different use cases depending on the used optimization methods: Adam (Diederik and Jimmy 2014) and two variants of Stochastic Gradient Descent (SGD).

As we know, an important part of developing a DL architecture is the selection of hyperparameters. Different methods exist for choosing such values:

1. Manual: hyperparameters are set through trial-and-error until a usable set of parameters are found.

2. Search algorithms: A grid search, or random search algorithm can be deployed. The network is then trained on multiple models by using all combinations of parameters made available in these ranges (Bergstra and Bengio, 2012).

The learning rate (LR) range (base\_lr, max\_lr) was firstly determined through trial-and-error test by observing the variations of loss value. Then two techniques (associated with SGD) were experimented: Cyclical Learning Rate (CLR) (Kenstler 2018) and Warm Restart (SGDR) (Loshchilov and Hutter 2016).

According to (Smith 2017), letting the learning rate cyclically vary between reasonable bounds (Figure 5) can increase the accuracy of the model in fewer steps and escape the saddle points more efficiently.

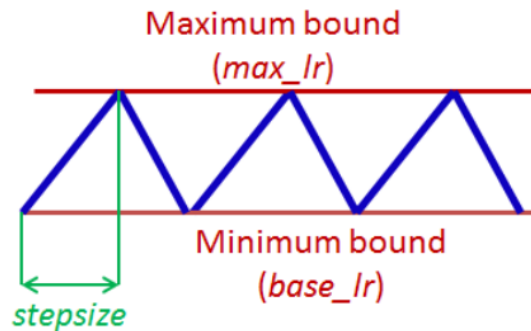


Figure 5. Cyclical learning rate (Smith 2017)

SGDR (Figure 6) is similar to CLR. It applies an aggressive annealing strategy. So, the learning rate is varied during training deep neural networks and performance is improved (Loshchilov and Hutter 2016).

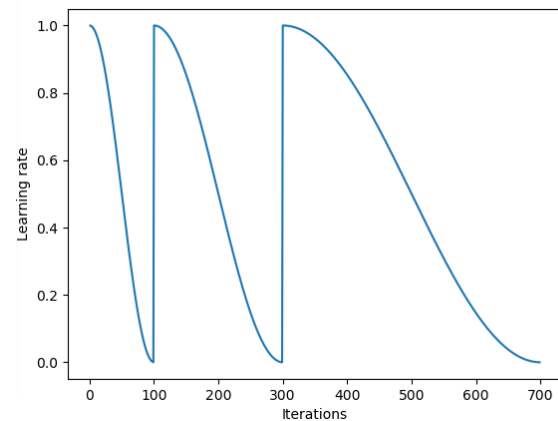


Figure 6. SGD with restart and cosine annealing

In the second part of this study, we assess (for the three adopted architectures) the impact of data augmentation. We considerably augment the initial training dataset (outside training process) combining 90 degrees rotations with top-bottom and left-right flip (Bloice, 2017) which increased the training dataset 10 times (500 images with associated ground truth).

In addition, we also assess the temporal generalization of the best model (from the three architectures) learned from the first Landsat 8 image acquired at the beginning of the agricultural cycle (Autumn period). The idea is to explore the feasibility of predicting (using the same model) the

location of irrigated areas at some specific times in the same agricultural cycle (Spring and Summer periods).

As evaluation metrics (Liu et al. 2019) for image segmentation, we use Pixel Accuracy (Pacc) (Eq. 1) and Intersection over Union (IoU) (Eq. 2):

$$P_{acc} = \frac{\sum_i n_{ii}}{\sum_i t_i} \quad (1)$$

$$IoU = \frac{1}{n_{cl}} \sum \frac{n_{ii}}{t_i + \sum_j n_{ji} - n_{ii}} \quad (2)$$

Where,

n<sub>ij</sub>: number of pixels of class i predicted correctly to belong to class j

n<sub>cl</sub>: number of classes

t<sub>i</sub>: number of pixels of class i (t<sub>i</sub> = ∑<sub>j</sub> n<sub>ij</sub>)

Our architectures were implemented based on Keras API with TensorFlow backend. All models are trained and tested using Google Colaboratory.

#### 4. RESULTS and DISCUSSIONS

##### 4.1 Generating Land Cover Maps without Data Augmentation

On the limited train dataset, we experiment three of the known DL architectures: SegNet, DenseNet and UNet. The overall accuracy obtained doesn't exceed 47%.

To improve the performance, we rely on UNet architecture with ResNet50 as backbone and used a loss based on the categorical cross entropy. For all models, we use a minibatch size of 32 images (this choice was a result of trial and error testing for four values: 8, 16, 24 and 32) and fixed learning rates between base\_lr=0.001 and max\_lr=0.01. The results for the three use cases based on the variation of the optimization method are as follow.

**Table 3** Pixel accuracy and IoU metrics on test dataset

Land Cover	ADAM		SGD_CLR		SGDR	
	Acc (Pixel)	IoU	Acc (Pixel)	IoU	Acc (Pixel)	IoU
Impervious	75%	43%	54%	32%	36%	26%
Forest	56%	39%	81%	72%	74%	67%
Water	45%	37%	6%	6%	2%	2%
Arable land	85%	73%	83%	69%	90%	72%
Irrigated land	74%	63%	78%	62%	81%	62%
Greenhouse	82%	63%	6%	6%	5%	5%
Orchard	42%	40%	18%	9%	15%	14%
<b>Mean</b>	<b>66%</b>	<b>51%</b>	<b>47%</b>	<b>37%</b>	<b>43%</b>	<b>35%</b>

With mean IoU of 51% (63% for Irrigated land class) and with less confusion among classes, Adam gives the best result (Table 3). Hereafter some

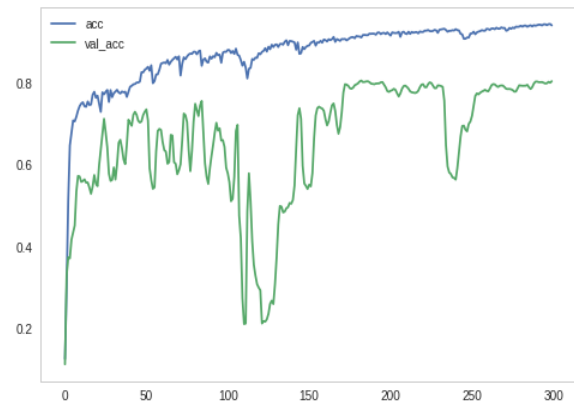


**Figure 7.** Accuracies on training and validation datasets based on 300 epochs (Adam method)

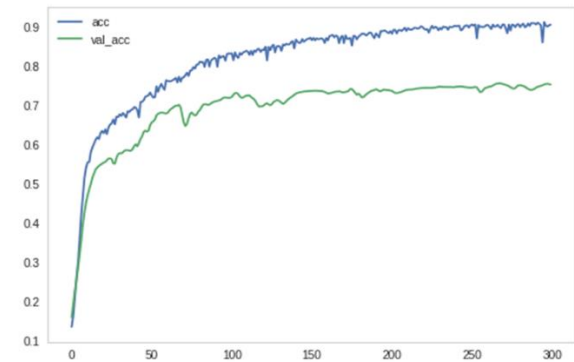


**Figure 8.** Accuracies on training and validation datasets based on 300 epochs (SGD method with CLR and Restart)

The results show a clear improvement with an overall accuracy fluctuating around 94% (76% on validation dataset for Adam method) (Figure 7). The two variants of SGD lead to relatively smooth increasing to reach 91% as overall accuracy and 72% on validation dataset (Figure 8) but with a value of loss (on validation dataset) that doesn't decrease under the value of 1.

predictions outputted on some test images (Figure 9) and the whole first image (Figure 10).

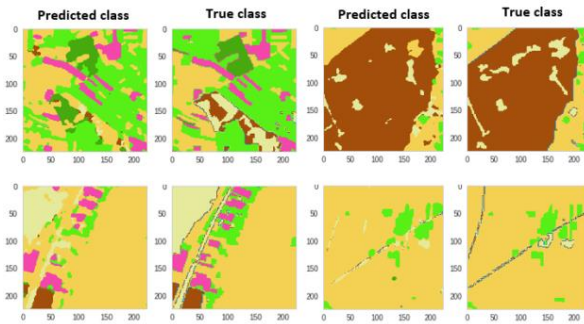


**Figure 9.** Predictions on some test images by Adam based model

From this, it can be seen that Adam based network is particularly good at predicting irrigated areas and green houses.

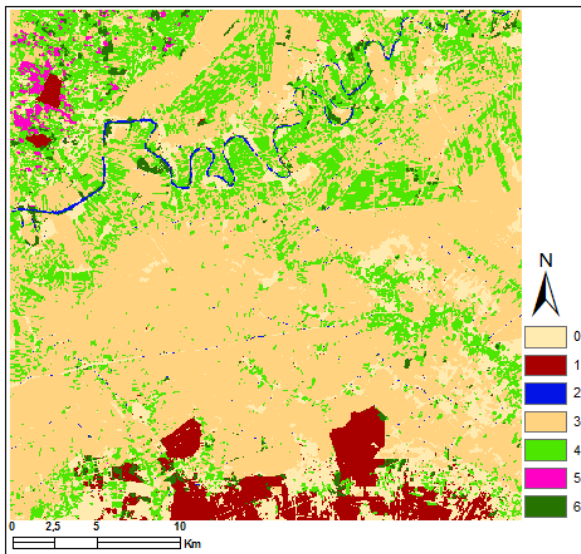


**Figure 10.** Land cover map generated by Adam based model

#### 4.2 Generating Land Cover Maps with Data Augmentation

In the deep learning field, it is commonly known that a large amount of data is required to properly train a network. Unfortunately, accessing a suitable amount of data is not possible (or time consuming) for everyone along with data ground truth information.

In this second part of the study, we experimented the same three models on the

augmented training dataset to assess the impact on performance and accuracies.

After artificially augmenting the training dataset and with less epochs (200), the overall accuracy has increased from 94% to 97% for Adam based method (Figure 11) and from 91% to 94% for SGD based methods (Figure 12). Also, the overall accuracy for the three methods on validation dataset has increased and reached respectively 92% and 91%.

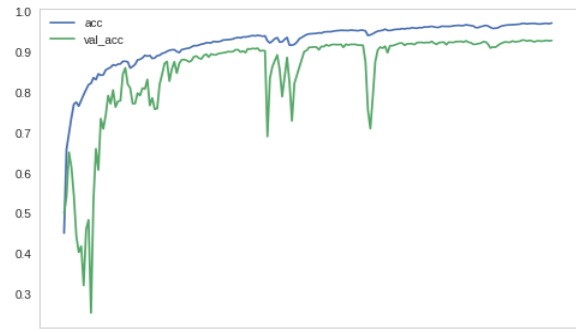


**Figure 11.** Accuracies on augmented training and validation datasets based on 200 epochs (Adam method)

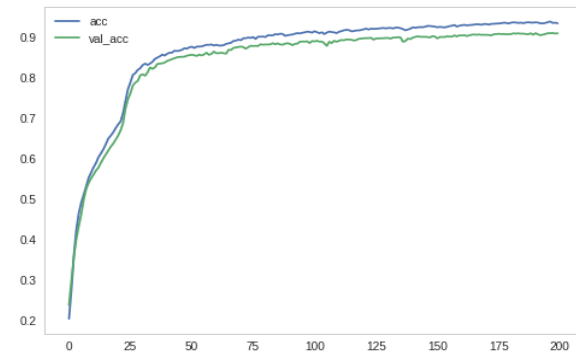


**Figure 12.** Accuracies on augmented training and validation datasets based on 200 epochs (SGD method with CLR and Restart)

All the methods (Table 4) perform well (less confusion among classes). Adam based method outperform the other methods especially for classes water and irrigated land. This latter is mapped with high degree of performance (IoU of 87%).

**Table 4** Pixel accuracy and IoU metrics on test dataset

Land Cover	ADAM		SGD_CLR		SGDR	
	Acc (Pixel)	IoU	Acc (Pixel)	IoU	Acc (Pixel)	IoU
Impervious	89%	84%	89%	74%	90%	80%
Forest	93%	87%	93%	89%	89%	86%
Water	74%	56%	49%	39%	44%	37%
Arable land	96%	91%	93%	87%	95%	87%
Irrigated land	93%	87%	91%	82%	90%	82%
Greenhouse	78%	63%	73%	63%	74%	66%
Orchard	87%	84%	96%	90%	93%	84%
<b>Mean</b>	<b>87%</b>	<b>79%</b>	<b>83%</b>	<b>75%</b>	<b>82%</b>	<b>75%</b>

Using Google Colaboratory with GPU processing capacities, it has been noticed that training and testing all models show the same speed performance.

Below, some predictions produced on some test images (Figure 13) and the first whole image (Figure 14).

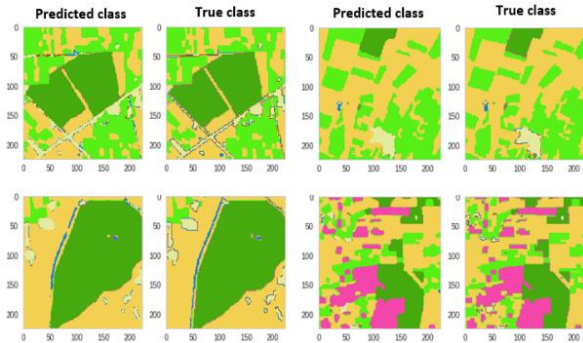


**Figure 13.** Predictions on some test images by Adam based model

### 4.3. Temporal Generalization of the Best Learned Model

The aim here is to assess how robust is the temporal generalization of the best learned model

(from the previous phase). Two new test datasets (ground truth masks) are photo interpreted based on two acquisitions corresponding to spring and summer periods in the same agricultural cycle. The results of the predictions evaluations (Table 5) are given hereafter.

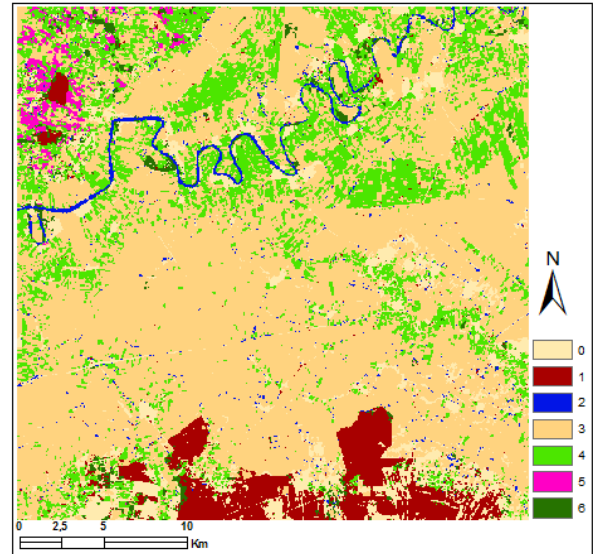


**Figure 14.** Land cover map generated by Adam based model (on augmented training dataset)

**Table 5.** Pixel accuracy and IoU metrics on test datasets for the three image acquisitions

	AGRICULTURAL CYCLE					
	AUTUMN		SPRING		SUMMER	
Land Cover	Acc (Pixel)	IoU	Acc (Pixel)	IoU	Acc (Pixel)	IoU
Impervious	89%	84%	79%	29%	88%	9%
Forest	93%	87%	65%	54%	6%	6%
Water	74%	56%	54%	23%	53%	40%
Arable land	96%	91%	58%	54%	29%	25%
Irrigated land	93%	87%	52%	37%	33%	28%
Greenhouse	78%	63%	21%	9%	5%	5%
Orchard	87%	84%	31%	8%	0%	0%
<b>Mean</b>	<b>87%</b>	<b>79%</b>	<b>51%</b>	<b>31%</b>	<b>31%</b>	<b>16%</b>

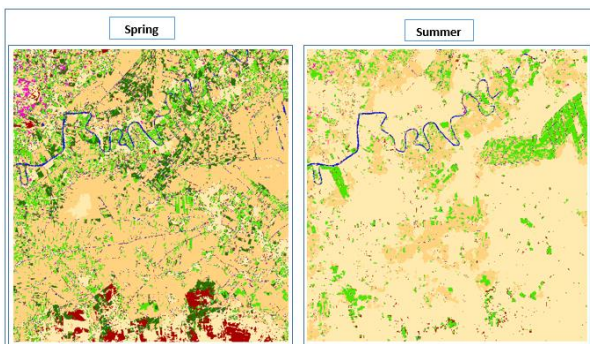


**Figure 15.** Predicted land cover maps for spring and summer L8 images

The results show low accuracies for the predictions on spring and summer L8 images (Figure 15 and 17). The main cause is the reflectance of the objects which change during the agricultural cycle. Especially for summer acquisition, more confusion

between irrigated land and orchard classes (Figure 16) and low performance for the other classes.

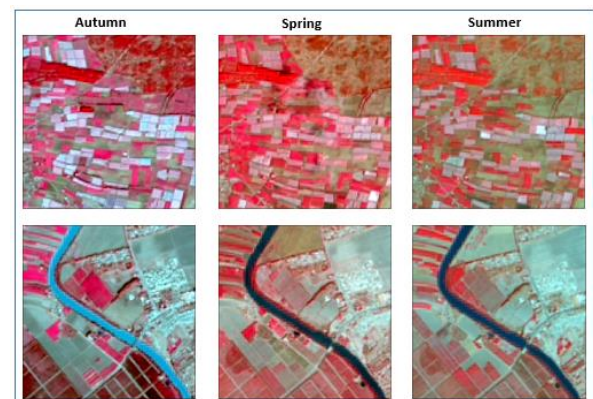


**Figure 16.** Samples of two test images acquired during different periods of the agricultural cycle

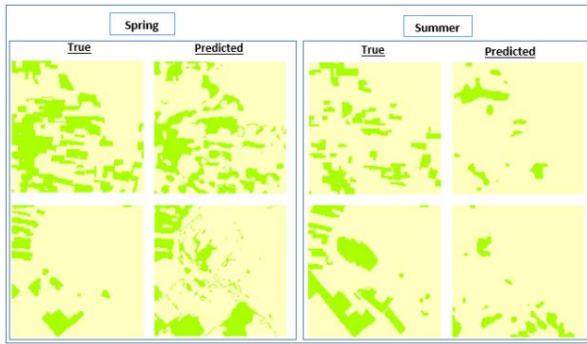


**Figure 17.** Predictions of irrigated areas (Green) on two test images

The aim of this third part experiments is to come up with a prediction model that can map irrigated areas at different times of an agricultural cycle. The reason behind is that our class of interest generally keep the same reflectance during the year. Unfortunately, 2015-2016 was a specific year marked by a severe drought in Morocco which explain the low accuracies and also the confusion among classes.

## 5. CONCLUSIONS

With the aim of irrigated areas automatic mapping from RGB Landsat 8 satellite images, we review three architectures based on UNet with ResNet50 as backbone. Initially, small dataset of 50 images with associated ground truth labels were used in training and validation.

**Table 6.** Irrigated areas mapping accuracies using the three architectures

Model	ADAM		SGD_CLR		SGDR	
	Acc (Pixel)	IoU	Acc (Pixel)	IoU	Acc (Pixel)	IoU
Without AUG	74%	63%	78%	62%	81%	62%
With AUG	93%	87%	91%	82%	90%	82%

AUG: Augmentation

Without data augmentation, Adam based model gives the best result with mean IoU of 51% (63% for Irrigated land class) (Table 6). We believe that better performances can be achieved using more data.

After artificially augmenting the training dataset, the overall accuracy has increased from 94% to 97% for Adam based model and from 91% to 94% for SGD based models. The irrigated areas are mapped with high degree of performance (IoU  $\geq$  82%). On the same area of interest and using Random Forest algorithm (Benbahria et al., 2018) we obtained less accuracy. This could confirm the relevance of using these new approaches based on deep learning architectures.

On the other hand, the temporal generalization of the best learned model to spring and summer L8 images (in the same agricultural cycle) leads to low accuracies with 37% and 28% IoUs respectively. Many enhancements can be explored to improve these results. Firstly, we can further augment the

training dataset from different season's images. Adding more spectral bands and indices into training images should also be explored.

## ACKNOWLEDMENT

This research was supported in part through computational resources of HPC-MARWAN ([www.marwan.ma/hpc](http://www.marwan.ma/hpc)) provided by the National Center for Scientific and Technical Research (CNRST) in Morocco.

Also, the authors gratefully acknowledge all persons who have made available to the scientific community the codes in the GitHubs hereafter referenced.

## REFERENCES

- Acquarelli J, Marchiori E, Buydens L M C, Tran T & van Laarhoven T (2018). Spectral-spatial classification of hyperspectral images: Three tricks and a new learning setting. *Remote Sensing*, 10(7), 1156. DOI: 10.3390/rs10071156
- Audebert N, Le Saux, B & Lefèvre S (2017). Fusion of heterogeneous data in convolutional networks for urban semantic labeling. 2017 Joint Urban Remote Sensing Event (JURSE), 1-4.
- Audebert, N, Le Saux B & Lefèvre S (2016). Semantic segmentation of earth observation data using multimodal and multi-scale deep networks. *Asian Conference on Computer Vision*. Springer, Cham, 180-196.
- Badrinarayanan V, Kendall A & Cipolla R (2017). Segnet: A deep convolutional encoder-decoder architecture for image segmentation. *IEEE transactions on pattern analysis and machine intelligence*, 39(12), 2481-2495.
- Ball J E, Anderson D T & Wei P (2018). State-of-the-art and gaps for deep learning on limited training data in remote sensing. *IGARSS 2018-2018 IEEE International Geoscience and Remote Sensing Symposium*, 4119-4122.
- Benbahria Z, Sebari I, Hajji H & Smiej M F (2018). Automatic mapping of irrigated areas in Mediterranean context using Landsat 8 time series images and random forest algorithm. *IGARSS 2018 - 2018 IEEE International Geoscience and Remote Sensing Symposium*, 7986-7989. Valencia, Spain, DOI: 10.1109/IGARSS.2018.8517810
- Bergstra J & Bengio Y (2012). Random search for hyper-parameter optimization. *Journal of Machine Learning Research*, 13, 281-305.
- Bilinski P & Prisacariu V (2018). Dense decoder shortcut connections for single-pass semantic segmentation. *Proceedings of the IEEE Conference on Computer Vision and Pattern Recognition*, 6596-6605.
- Bloice M D (2017). <https://github.com/mdbloice/Augmentor> Accessed date: January, 27th 2020

- Diederik P K & Jimmy L B (2014). Adam: A method for stochastic optimization. 3rd International Conference for Learning Representations, San Diego
- Feng W, Sui H, Huang W, Xu C & An K (2019). Water body extraction from very high-resolution remote sensing imagery using deep U-Net and a superpixel-based conditional random field model. *IEEE Geoscience and Remote Sensing Letters*, 16(4), 618-622.
- Ghazi M M, Yanikoglu B & Aptoula E (2017). Plant identification using deep neural networks via optimization of transfer learning parameters. *Neurocomputing*, 235, 228-235.
- He K, Zhang X, Ren S & Sun J (2016). Deep residual learning for image recognition. *Proceedings of the IEEE conference on computer vision and pattern recognition*, 770-778.
- Iglovikov V, Mushinskiy S & Osin V (2017). Satellite imagery feature detection using deep convolutional neural network: A kaggle competition. *Computer Vision and Pattern Recognition*.
- Jégou S, Drozdal M, Vazquez D, Romero A & Bengio Y (2017). The one hundred layers tiramisu: Fully convolutional densenets for semantic segmentation. *Proceedings of the IEEE conference on computer vision and pattern recognition workshops*, 11-19.
- Jiang R X (2017). <https://towardsdatascience.com/dstl-satellite-imagery-contest-on-kaggle-2f3ef7b8ac40> Accessed date: 1May, 2020
- Johnson B A, Tateishi R & Hoan N T (2012). Satellite image pansharpening using a hybrid approach for object-based image analysis. *ISPRS International Journal of Geo-Information*, 1(3), 228-241.
- Kenstler, B. (2018). <https://github.com/bckenstler/CLR> Accessed date: January, 27th 2020
- Khryashchev V, Ivanovsky L, Pavlov V, Ostrovskaya A & Rubtsov A (2018). Comparison of Different Convolutional Neural Network Architectures for Satellite Image Segmentation. 23rd Conference of Open Innovations Association (FRUCT), 172-179
- Lagrange A, Le Saux B, Beaupere A, Boulch A, Chan-Hon-Tong A, Herbin S, Randrianarivo H & Ferecatu M (2015). Benchmarking classification of earth-observation data: From learning explicit features to convolutional networks. *International Geoscience and Remote Sensing Symposium (IGARSS)*, 4173-4176.
- LeCun Y, Bottou L, Bengio Y & Haffner P (1998). Gradient-based learning applied to document recognition. *Proceedings of the IEEE*, 86(11), 2278-2324.
- Lin Z, Chen Y, Zhao X & Wang G (2013). Spectral-spatial classification of hyperspectral image using autoencoders. In: 2013 9th International Conference on Information, Communications & Signal Processing.
- Liu T, Abd-Elrahman A, Morton J & Wilhelm V L (2018). Comparing fully convolutional networks, random forest, support vector machine, and patch-based deep convolutional neural networks for object-based wetland mapping using images from small unmanned aircraft system. *GIScience & remote sensing*, 55(2), 243-264.
- Liu X, Deng Z & Yang Y (2019). Recent progress in semantic image segmentation. *Artificial Intelligence Review*, 52, p. 1089-1106.
- Long J, Shelhamer E & Darrell T (2015). Fully convolutional networks for semantic segmentation. *Proceedings of the IEEE Conference on Computer Vision and Pattern Recognition*, 3431-3440.
- Loshchilov I & Hutter F (2016). Sgdr: Stochastic gradient descent with warm restarts. *ICLR 2017*, 1-16
- Merdas M, Ozdogan M, Benbahria Z, Khajour L & Youssoufi E E (2015). Mapping of irrigated crops and monitoring of their evolution using satellite images. *GEO OBSERVATEUR*, N°22
- Mnih V (2013). Machine learning for aerial image labeling. PHD Thesis, University of Toronto, Canada
- Othman E, Bazi Y, Alajlan N, Alhichri H & Melgani F (2016). Using convolutional features and a sparse autoencoder for land-use scene classification. *International Journal of Remote Sensing*, 37(10), 1977-1995
- Ozdogan M, Yang Y, Allez G & Cervantes C (2010). Remote sensing of irrigated agriculture: Opportunities and challenges. *Remote Sensing*, 2, 2274-2304 DOI: 10.3390/rs2092274
- Paisitkriangkrai S, Sherrah J, Janney P & Hengel V D A (2015). Effective semantic pixel labelling with convolutional networks and conditional random fields. *Conference on Computer Vision and Pattern Recognition Workshops*, 36-43
- Pan S J & Yang Q (2010). A survey on transfer learning. *IEEE Transactions on knowledge and data engineering*, 22(10), 1345-1359.
- Panboonyuen T, Jitkajornwanich K, Lawawirojwong S, Srestasathien P & Vateekul P (2019). Semantic segmentation on remotely sensed images using an enhanced global convolutional network with channel attention and domain specific transfer learning. *Remote Sensing*, 11(1), 83.
- Papadomanolaki M, Vakalopoulou M, Zagoruyko S & Karantzalos K (2016). Benchmarking deep learning frameworks for the classification of very high resolution satellite multispectral data. *ISPRS Annals of Photogrammetry, Remote Sensing & Spatial Information Sciences*, 3(7), 83-88
- Pirotti, F. and Sunar, F. and Piragnolo, M. (2016). Benchmark of machine learning methods for classification of a Sentinel-2

- image. International Archives of the Photogrammetry, Remote Sensing & Spatial Information Sciences, 41, 335-340
- Ronneberger O, Fischer P & Brox T (2015). U-net: Convolutional networks for biomedical image segmentation. In International Conference on Medical image computing and computer-assisted intervention, 9351, 234-241. Springer, Cham.
- Sherrah J (2016). Fully convolutional networks for dense semantic labelling of high-resolution aerial imagery. Computer Vision and Pattern Recognition
- Smith L N (2017). Cyclical learning rates for training neural networks. In: 2017 IEEE Winter Conference on Applications of Computer Vision (WACV), 464-472
- Thoma M (2016). A survey of semantic segmentation. Computer Vision and Pattern Recognition
- Tuia D, Persello C & Bruzzone L (2016). Domain adaptation for the classification of remote sensing data: An overview of recent advances. IEEE geoscience and remote sensing magazine, 4(2), 41-57.
- Vooban A (2017). <https://medium.com/vooban-ai/satellite-image-segmentation-a-workflow-with-u-net-7ff992b2a56e> Accessed date 1 May 2020
- Wu Z, Shen C & Hengel A V D (2016). High-performance semantic segmentation using very deep fully convolutional networks. Computer Vision and Pattern Recognition
- Wurm M, Stark T, Zhu X X, Weigand M & Taubenböck, H (2019). Semantic segmentation of slums in satellite images using transfer learning on fully convolutional neural networks. ISPRS Journal of Photogrammetry and Remote Sensing, 150, 59-69.
- Xu Y Wu L, Xie Z & Chen Z (2018). Building extraction in very high-resolution remote sensing imagery using deep learning and guided filters. Remote Sensing, 10(1), 144. DOI: 10.3390/rs10010144
- Yakubovskiy, P. (2018). [https://github.com/qubvel/segmentation\\_models](https://github.com/qubvel/segmentation_models) Accessed date :1 May 2020
- Yang J, Zhao Y, Chan J C W & Yi C (2016). Hyperspectral image classification using two-channel deep convolutional neural network. 2016 IEEE International Geoscience and Remote Sensing Symposium (IGARSS), 5079-5082.
- Younis M C & Keedwell E (2019). Semantic segmentation on small datasets of satellite images using convolutional neural networks. Journal of Applied Remote Sensing, 13(4) DOI: 10.1117/1.JRS.13.046510
- Zhang C, Yue P, Di L & Wu Z (2018). Automatic identification of center pivot irrigation systems from landsat images using convolutional neural networks. Agriculture, 8(10), 147. DOI: 10.3390/agriculture8100147
- Zhu X X, Tuia D, Mou L, Xia G S, Zhang L, Xu F & Fraundorfer F (2017). Deep learning in remote sensing: A comprehensive review and list of resources. IEEE Geoscience and Remote Sensing Magazine, 5(4), 8-36.



© Author(s) 2021.

This work is distributed under <https://creativecommons.org/licenses/by-sa/4.0/>



## An investigation of urban development with geographical information systems: 100-year change of Sivas City, Turkey

Sefa Sarı<sup>1</sup> , Tarık Türk<sup>\*2</sup> 

<sup>1</sup>Sivas Cumhuriyet University, Engineering Faculty, Department of Geomatics Engineering, Sivas, Turkey

### Keywords

Sivas  
GIS  
Urban development  
Urbanization  
Temporal analysis

### ABSTRACT

One of the most important duties of urbanism is to meet the basic needs of people. The need for shelter takes a significant place among the basic needs of people. Urban populations, which are increasing very rapidly nowadays, have made urban development a non-negligible situation. Urban planning should be done by ensuring urban development and without losing the city identity, and a regular development strategy should be adopted according to objective criteria in order to manage the available resources correctly. In this study, the 100-year urban development of Sivas city center was examined with the Geographical Information System (GIS) by considering historic buildings and population projection, and the relationship between housing in the city in this process and complementary zoning plans was investigated.

## 1. INTRODUCTION

The need for shelter, which is the most basic need of people living in a community due to their nature, takes a significant place at every stage of history. While people used to use sheltered, safe, and high areas for shelter in historical processes, collective shelter areas have started to be formed near water resources with the transition to the settled order, and then the concept of city has emerged. Nowadays, migration movements from rural to urban areas continue at an accelerated rate. Although the world population increased by 6 times on average in the past two hundred years, urban populations increased by more than 100 times (Stalker 2000). According to the 2017 report of the United Nations Population Organization, it is estimated that the world population will be around 10 billion in 2050 and 80% of this population will live in cities (U N 2017). The population density, which occurs with the increase in urban populations, increases the social and economic needs of the society and causes resources to be consumed rapidly. As a result, the natural balance deteriorates, vegetation cover, agricultural areas, and ecological

structures are destroyed to an irreparable extent, and even the danger of extinction is faced (Özyavuz 2011). In the literature, there are various studies for the examination of urban development by remote sensing and GIS methods (Göksel and Doğru 2019; Song 2005; Sağır and Nacar 2008; Selim and Demir 2019).

İşcan and Ilgaz (2017) stated that GIS is used by municipalities to provide better services and to improve decision-making mechanisms including tax administration and city planning. Since urban development is inevitable, urban planning should be done very well, and the identity of the city, its historical and cultural values should be preserved. Furthermore, a sustainable urban zoning plan should be made by considering the socio-economic structure, demographic structure, geographical structure, cultural structure, and population density of the city (Yılmaz et al. 2007). The concept of urban development includes many parameters. The social and economic structure of the society, geographical location, topography, land use, population density, individual and social needs, the sense of belonging to the city, and political will are only some of these parameters (Erarslan and Kolay 2005). Unforeseen

### \* Corresponding Author

(sefasari58@gmail.com) ORCID ID 0000 – 0002 – 4142 – 9845  
\*(tarikurturk@gmail.com) ORCID ID 0000 – 0002 – 2671 – 7590

### Cite this article

Sarı S & Türk T (2021) An investigation of urban development with geographical information systems: 100-year change of Sivas City, Turkey. International Journal of Engineering and Geosciences– 2021; 6(1); 51-63

growth rate with industrialization and technological developments is another parameter in urban development (Kasanko et al. 2006). All parameters should be evaluated together, and low-density cities should be planned. Along with rapid urbanization and land cover changes in recent years, led to a decrease in natural habitats especially in developed and developing countries (Selim and Demir 2019).

Nowadays, since urban development progresses rapidly, rural settlements face the threat of extinction, and green areas are rapidly concreted. The densities of cities, which are rapidly becoming complicated and in which green areas are depleted, should be reduced, and planning should be done well (Haaland and Bosch 2015).

Urbanization, by its simple definition, means an increase in the population living in cities (Sağır and Nacar 2008). Urbanization in developing countries occurs in the form of population raids. However, urbanization should not be considered only in the context of population movements. Urbanization can also be defined as the transition from agricultural production to a higher level of production (Uysal et al. 2016). This transition has necessitated the gathering of all production control functions in cities and also has led to the growth and density of cities and has caused the increase in the degrees of heterogeneity and integration (Tekeli 1997). Therefore, while defining urbanization, it is also necessary to include social and economic changes that create that population movement. Considering in this way, urbanization can be defined as “a population accumulation process that results in the increase in the number of cities in parallel with industrialization and economic development, the growth of today’s cities, that creates organization, division of labor and specialization at an increasing rate in the social structure, and causes city-specific changes in human behaviors and relationships.” It is possible to list the reasons affecting urbanization as economic reasons, technological reasons, political reasons, and socio-psychological reasons (Sağır and Nacar 2008).

Good planning should be done for healthy and livable places, vehicle traffic, pedestrian traffic, living areas, natural and green areas should be planned well, and accommodation styles suitable for the topography and nature of the land should be created. The sun, which is indispensable for life, should be able to enter all houses, and life-threatening elements, such as dust, noise, and exhaust gas, should be minimized. Sunshine durations should be estimated in all buildings to be planned, and the soil policy should be developed for this purpose (Corbusier 1933). Empty places that will allow people to rest, have fun, and relax physically and mentally after intensive working hours have been concreted rapidly in recent times, and people are condemned to live among massive concrete piles of their own scales. It is indispensable for the future of cities to create areas where people can spend daily, weekly, and annual leisure time and rest. Parks and

green areas, areas of sports activities, beaches, forests, recreation and entertainment places should be placed in a certain order among the concrete piles of the city and turned into common living spaces of people (Corbusier 1933).

One of the most critical problems in the development of cities is the transportation problem. The dimensions of streets are insufficient for the speed of motor vehicles, and they cannot bear the load increasing every day. The shortness of the intersection points of roads, huge houses situated close to each other, insufficient street widths, high costs of expansion works, and insufficiency in the solution of the problem emerge as major obstacles to the development of the city (Song 2005).

The first parameter that comes to mind when talking about the city is the “City identity.” The heritage of the city is provided by the existence of that city, its development, circulation, and survival of the existing historical monuments. (Yakar and Doğan 2018) Every person wants to see the traces of the environment where he was born and raised. The sense of belonging of people who see their past is reinforced, and they see their roots in that city. At the stage of planning a city, first of all, it is necessary to protect the buildings that the city has and which have the identity of the city, to green its surroundings, and to turn it into places where people can spend time (Corbusier 1933).

As a result of storing the temporal data of a city in the GIS environment, it is possible to make temporal change analysis and future-oriented models in the city (Liu 2008). Thus, the temporal changes occurring in the cities can be introduced quickly and effectively and necessary planning strategies can be developed in line with this change. In this process, GIS provides many advantages in terms of time, cost and labor (Kızılelma et al. 2013).

In this study, temporal changes occurring in Sivas city center within 100 years were analyzed in the GIS environment using data such as zoning plan, ortho-photograph, population, and current map within the boundaries of Sivas city center.

## 2. STUDY AREA

Sivas province, which is one of the oldest settlements in Turkey’s history with an area of 28,488 km<sup>2</sup> consisting of 16 districts, is the second largest province in terms of Turkey’s territory. Upon examining Sivas settlement, which has hosted different civilizations in different periods of history, it is clearly observed that every civilization has added its own culture to the city and left a trace on the city settlement. The city, which has been integrated with its historical monuments that challenge the years among the building stocks that are constantly transforming, developing and concentrating, has gained the title of the “Sultan City” with its cultural values and rich history.

Since Sivas city is located at a point where the transportation networks of the country in the north-

south and east-west directions are knotted, it is a pass between the central and eastern Anatolian regions and is on the historic trade routes. It is possible to come across traces of history in almost every street of Sivas, which has hosted many civilizations. The structures built by civilizations to meet their shelter and social needs are monuments that have survived to the present day. The oldest settlement plans of Sivas city center that have been encountered recently are the city fortification wall map and city map of (Albert Gabriel 1934) and the city plan of Arakel Badrik 1915 (Natanyan 2008) .

The municipal boundaries of the central district of Sivas province, which is selected as the study area, have a surface area of approximately 192 km<sup>2</sup> and an average height of 1200 meters (Fig. 1).

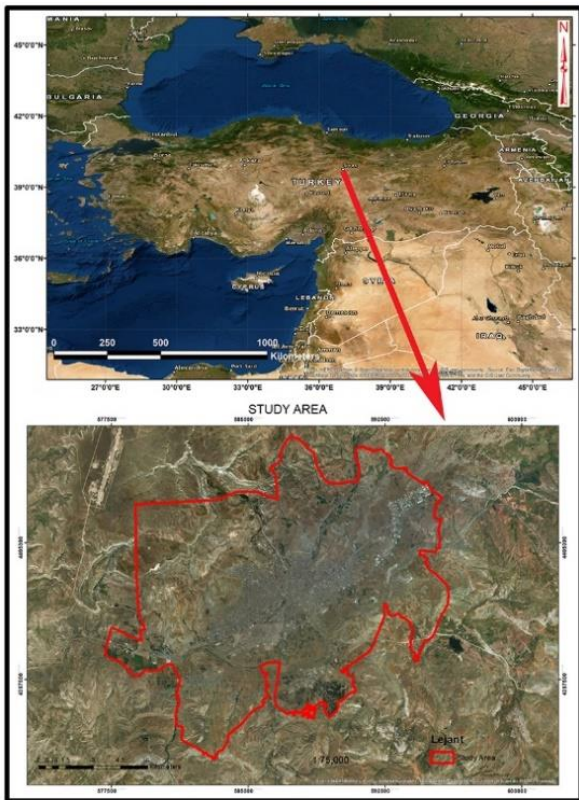


**Figure 1.** Study Area (Sivas City Center)

### 3. MATERIAL and METHODS

Within the scope of this study, different data, such as the population data, administrative boundary data, and land use of Sivas province between 1927 and 2017, the City Fortification Wall Map of Sivas city center of Albert Gabriel with the

unknown exact date and turned into a book in 1928, the City Plan of Arakel Badrik dated 1915, current maps of different years, zoning plans, and ortho-photographs, were used. The details of these data are presented in the table below (Table.1).

**Table 1.** Data used in the study

Data Name	Year	Data type
City plan (Arakel Badrik)	1915	Plan
City fortification wall map) (Albert Gabriel)	1928	Plan
Implementary development plan	1937	Plan
Aerial photos	1949	Ortho-photo
Implementary development plan	1968	Plan
Aerial photos	1975	Ortho-photo
Implementary development plan	1984	Plan
Neighborhood map	1992	Map
Base map	2007	Map
Implementary development plan	2018	Plan

The population data of Sivas province between 1927 and 2017 were obtained, and the projection of the city and village populations of the study area was examined. While the city population and the village population were balanced in the first years of the Republic (approximately 50.21% of the population lived in the city in 1935), the population of the city reached 92.45% in 2017 as a result of an increasingly continuing migration wave from villages to the city center at a present time (Fig. 2).

Various maps have been produced for the city of Sivas, and there are many studies on this issue. In this study, in addition to the map and plans produced by Albert Gabriel and reflecting the oldest accessible plans of Sivas city (Fig. 3), the city plan produced by Arakel Badrik (Fig.4) (Natanyan 2008) was also included. The circle observed in the 1915 city plan produced by Arakel Badrik covers the city's craft and trade area (Fig. 4). While these maps are available only as sheets, they were scanned and geo-referenced and transferred to the GIS environment within the scope of this study.

While the graphical method is used for coordinate transformation of sheet maps of the study area, helmert transformation method is used for the coordinate transformation of other maps. For all data considered in the study, the ITRF-96 datum was taken as reference.

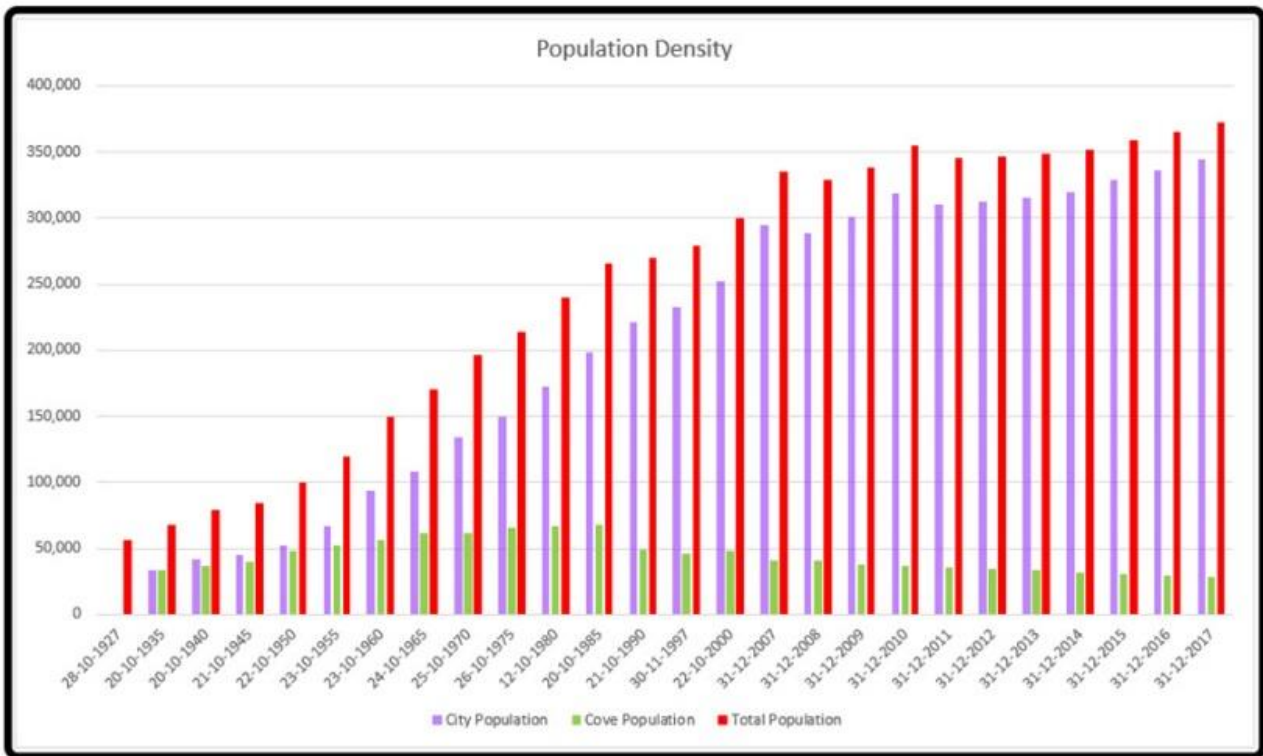


Figure 2. Population of the study area in different years

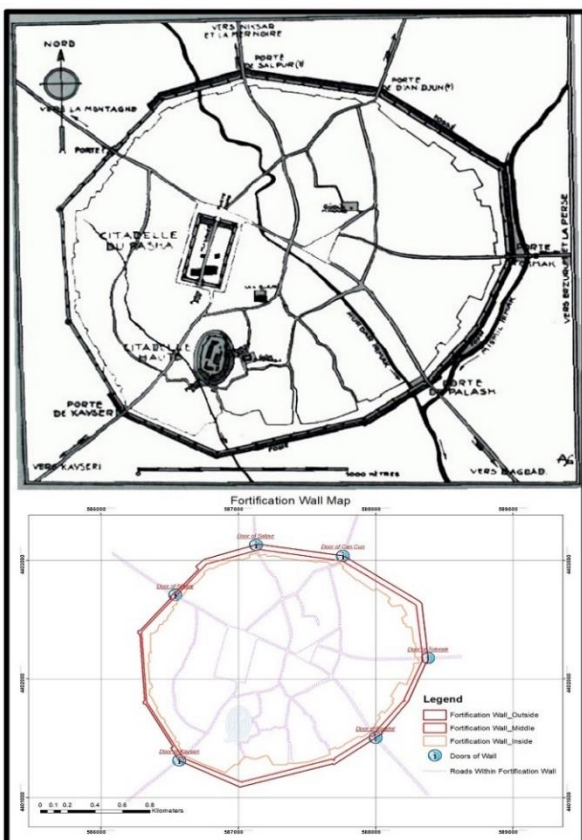
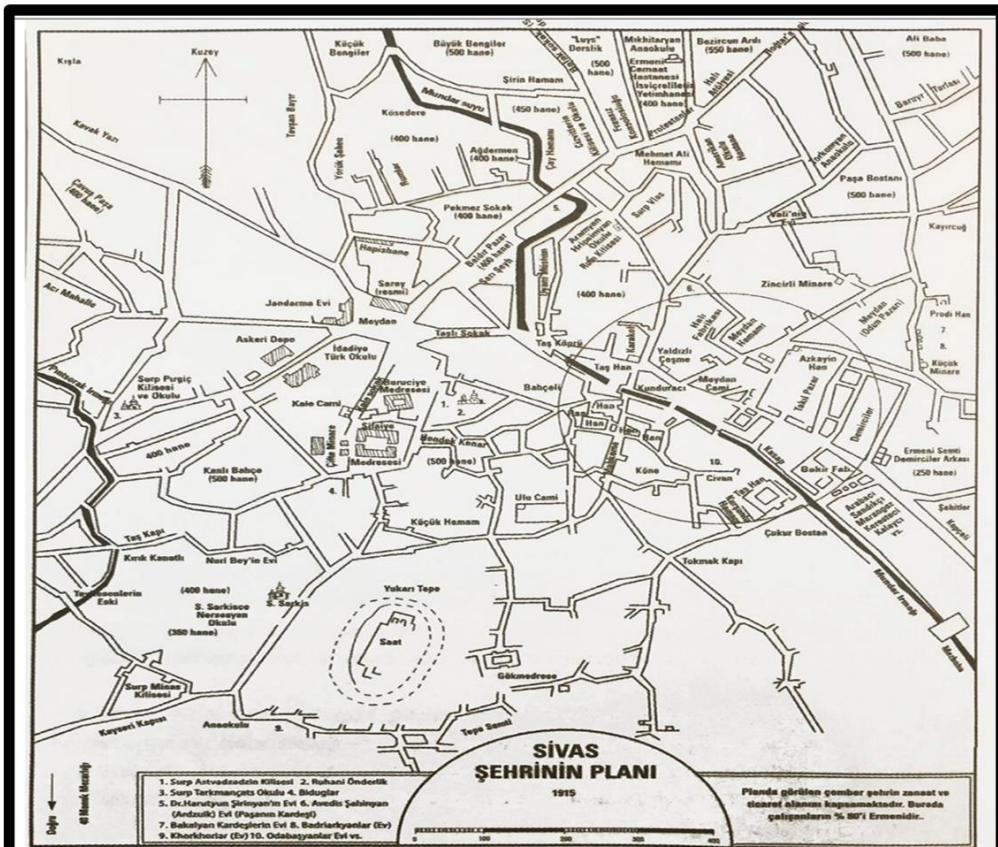


Figure 3. City Fortification Wall Map (Albert Gabriel, 1928)

The settlement direction of Sivas city center has constantly changed in the historical process. A lot of different data since 1915 were used in this study. The zoning plans and base maps for each period were digitized and overlapped. As a result of this process, settlement boundaries by years were obtained. All data were collected in a single database in the GIS environment and converted into the same coordinate system. Geographical and non-geographical data were integrated and made inquirable and analyzable (Fig. 5).

The settlement boundaries by years were divided into 100 m x 100 m grids and overlapped separately with each period. The value of 1 was assigned to the squares within the settlement boundary obtained by digitizing the zoning plan/map for each period, and the value of 0 was assigned to the squares outside the settlement boundary. Afterward, all the values were summed, and the grid value of each square was calculated. The Historic City Square (Historic Governorship City Square) was taken as a reference and divided into 8 zones, 4 main and 4 intermediate directions, and the direction information was defined. The urban development direction map of the city of Sivas was obtained by classifying according to the defined direction and grid values (Fig. 6). Here, the squares represented in green indicate the oldest settlement areas, while the areas represented in red indicate new settlement areas.



City Plan-Digital Map (Arakel Badrik-1915)

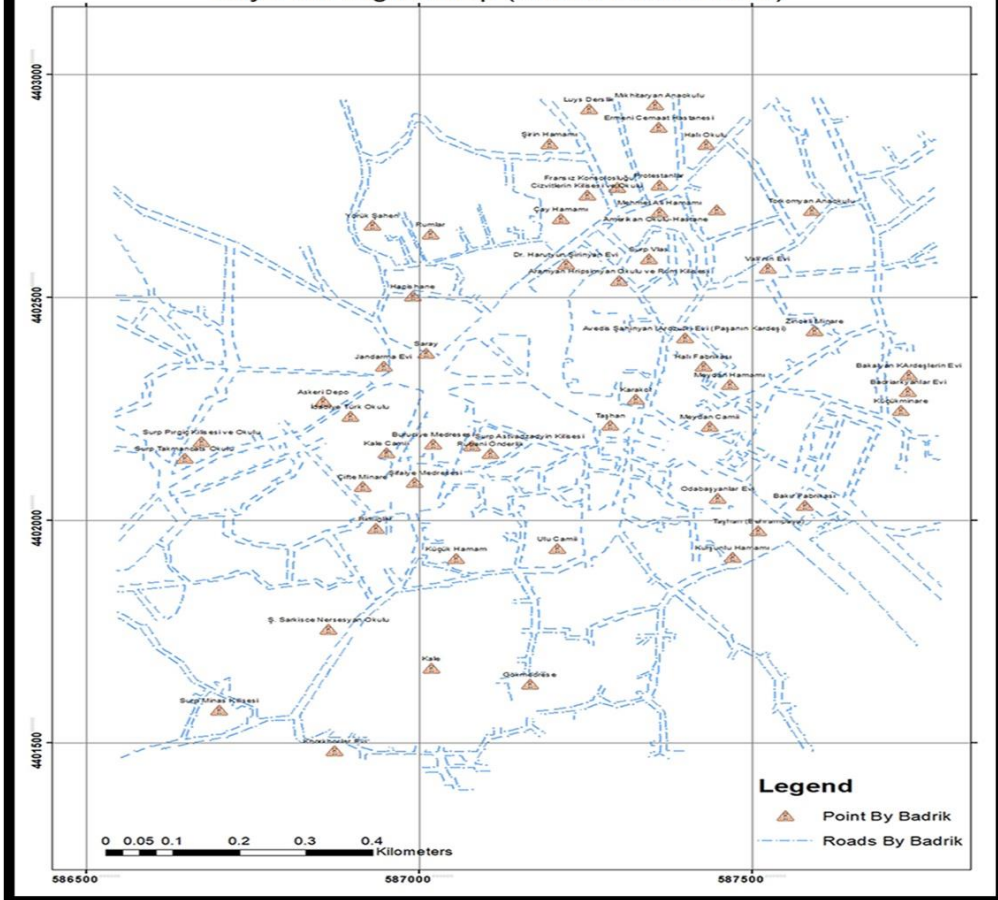


Figure 4. City Plan Map (Arakel Badrik-1915)

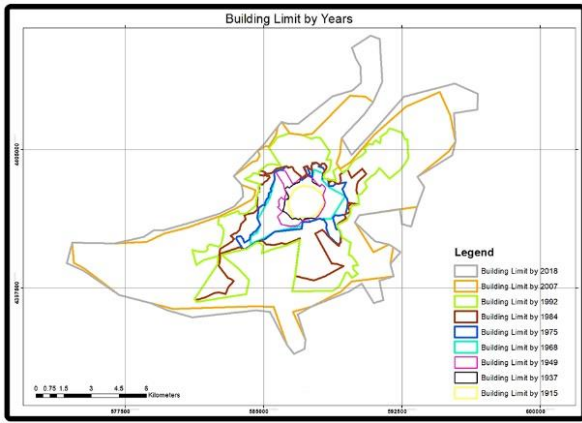


Figure 5. Settlement boundary in Sivas city by years



Figure 6. Urban development direction map of the city of Sivas

#### 4. RESULTS and DISCUSSION

Upon comparing the estimated zoning plans with the analyses conducted, it is impossible to talk about regular growth for Sivas city. The city has frequently undergone directional changes during the expansion, both under the influence of the locations selected for investments and decision-makers within historical phases (Table 2).

As the Paşabahçe power plant started production in 1934, urban development directed to the north. With the establishment of the State Railways Traction workshop in 1939, the city development directed toward the west, and with the coming of the Cement Factory into service in 1943, this orientation continued increasingly. With the establishment of Sivas Numune Hospital in 1953, the city development directed toward the north, but this development shifted to the northwest direction with the construction of the Nuri Demirağ Airport in 1966. Sidaş Spinning Factory, which was put into service in 1972, led the development in the east direction, and then the establishment of the Sivas Organized Industrial Zone in 1976 supported this development. In parallel with this period, with the coming of Sivas Cumhuriyet University, the foundations of which were laid in 1974, and the Faculty of Medicine in 1982, a very fast urbanization

trend in the south direction started, and as a result of this trend, the “Yenişehir District Mass Housing” project supported urbanization in 1987. In historical processes, public buildings, mass housing, and industrial areas have affected the direction of development of Sultan City Sivas. In addition to the fact that the city is not regular, it can be said that it expanded primarily to the south-west direction, to the north-east direction in the second place, and then to the west and south directions. The least expanding directions of the city are the north and north-west directions. The amount of changes that occurred in Sivas city in the last one hundred years is presented in detail in Table 3.

On the other hand, there are many important historic and cultural buildings in the city. While some of these structures are not available today, many of them still preserve their historical identities. The Twin Minarets Madrasah, Şifahiye Madrasah, Kale Mosque, Buruciye Madrasah, Governorship Building, Gendarmerie Building, and Congress Building in the historic city square are among the important structures that have survived until today. In addition to these, the Ulu Mosque (Grand Mosque), Taşhan, Eğri Bridge, Kurşunlu Turkish Bath, Behram Paşa Han, Meydan Turkish Bath, Güdük Minaret, Kangal Ağası Mansion, Ziya Bey Library, Kesik Bridge, Eski Paşa Turkish Bath, and Susamışlar Mansion located in various parts of the city are important buildings that shed light on the history of the Sultan city (Fig. 7, Fig. 8, Fig. 9 and Fig. 10). The geographic location and distribution of the historic buildings in Sivas are shown in Fig. 11.

Table 2. Parameters affecting urban development

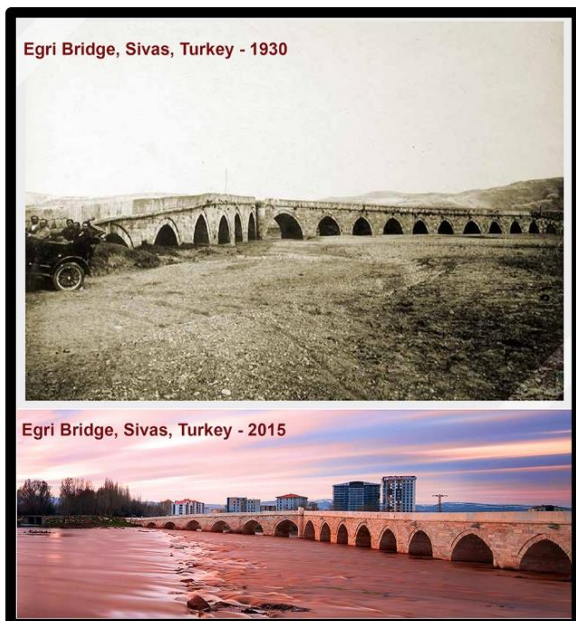
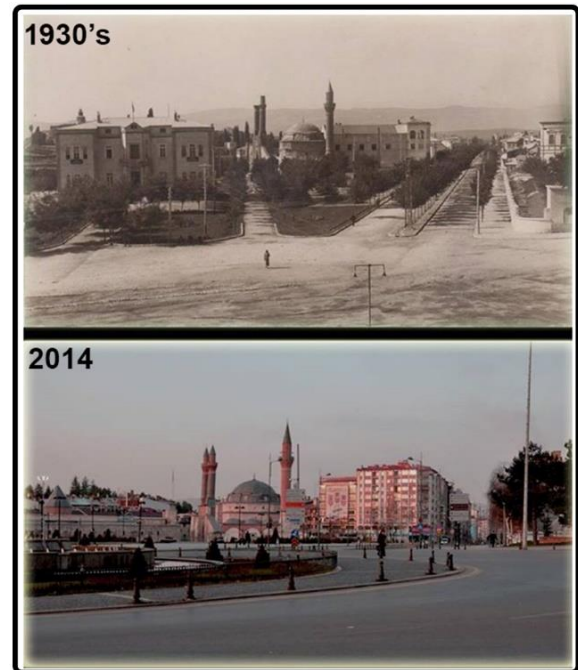
Parameter causing change	Year	Change in the city
Paşabahçe power plant	1934	The city development directed toward the North.
The state railways traction workshop	1939	The city development directed toward the east.
Cement Factory	1943	West orientation continued increasingly.
Sivas Numune Hospital	1953	The city development directed toward the North.
Nuri Demirağ Airport	1966	The city development directed toward the Northwest.
Sidaş Spinning Factory	1972	The city development directed toward the east.
Sivas Cumhuriyet University and the faculty of Medicine	1974 1982	A very fast urbanization trend in the South direction started.
Sivas Organized Industrial Zone	1976	East orientation continued increasingly.
Yenişehir District Mass Housing	1987	South orientation continued increasingly.

**Table 3.** Urban change rates in Sivas city by years

Settlement border year	Urban growth area (km <sup>2</sup> )	Urban growth rate (%)	Difference between years (km <sup>2</sup> )	Direction
1915	2.67	47.57	1.27	The north direction is weighted. Balance in all directions.
1937	3.94	37.56	1.48	Northwest and Northeast
1949	5.42	98.52	5.34	West, Southwest, Northwest, Northeast and East
1968	10.76	24.91	2.68	Southwest, southeast, Northeast, East
1975	13.44	93.45	12.56	South, Southwest and Northeast
1984	26.00	84.08	21.86	All directions except west and east
1992	47.86	145.13	69.46	Southwest and Northeast direction is weighted. Expansion in all directions.
2007	117.32	17.87	20.97	Southwest and Northeast
2018	138.29	-	-	-

Historical buildings in the city center are of great importance in terms of planning. Historical buildings supported certain housing around them according to their intended use and with this aspect, they contributed to the transformation of the city in time. These structures were sometimes used in accordance with the public service, and in others, they were used for different purposes in accordance with the flow of social life. Some of these historical buildings are introduced below.

The Eğri Bridge on the Baghdad (Silk) Road in ancient periods has provided transportation to the Sivas-Malatya road and Southeastern Anatolia until recently. The bridge, which is a Seljuk structure, is 173 m in length. It consists of two parts; one is 12 and the other one is 6. While the bridge continues in a straight way in the west direction, it was constructed from cut stones as inclined northward in the middle parts (Kültür Portalı 2019).

**Figure 7.** The Eğri Bridge (Adapted from Sivas Municipality archive)**Figure 8.** The city square of Sivas city (Adapted from Sivas Municipality archive)

There are many monuments in the Historic City Square. Information on these monuments is presented below.

The Government House was built in 1884 by Halil Rifat Paşa, the Governor of the city at that time. The first two floors of the building were built from cut stones, and the third floor was built from wood in 1913. As a result of a fire, the third floor was completely burned, and only the walls of the first and second floors were left. At the end of 2005, it regained its former appearance and function (Kültür Portalı, 2019).

The Kale Mosque was built by the Governor of Sivas, Ali Beyoğlu Mahmud Pasha, the vizier of Murad III in 1580 (Kültür Portalı 2019).

The Twin Minarets Madrasah is understood to be constructed by the İlhanlı Vizier Sahip Şemseddin Mehmet Cüveyni in 1271/1272 according to the inscription flowing in three directions just above the Crown gate. The only unique feature of the building

that has reached the present day is the magnificent front facade with the highest crown gate in Anatolia. The two minarets rising above the crown gate have become the symbol of Sivas. It is one of the most monumental madrasahs constructed in Anatolia and is also known as Dârü'l-hadis. It is still in good condition and open to visitors (Kültür Portalı 2019).

The Buruciye Madrasah is among the most famous structures in Sivas and Anatolia with its magnificent crown gate that has remained intact. The madrasah built in the period of the Seljuq Sultan Kaykhusraw III in 1271 was built by Muzaffer Burucerdî from Burucerd near Hamedan (Iran) to teach physics, chemistry, and astronomy. The structure, the architecture of which is not clear, has the madrasah plan with the most proper symmetry in Anatolia. Nowadays, it is used by Sivas Provincial Office of Mufti for various educational activities (Kültür Portalı 2019).

The Şifaiye Madrasah (Sivas Darüşşifa) is one of the most important madrasahs where patients were treated during the Seljuk Period and medical training was also provided. The part that has reached nowadays is the largest şifahane (hospital) of Anatolia. It was built by Izzeddin Keykavus I in 1217-1218. There are sun and moon symbols on the crown gate and reliefs in the form of a female and male head in the main iwan. After Izzettin Keykâvus I was buried here in 1220, the southern iwan was turned into a tomb (Kültür Portalı, 2019).

The Gendarmerie Building was built in 1908 as the Gendarmerie Office in the time of the Governor Vali Reşit Akif Pasha. The plan of the Gendarmerie Building extending in the west and north directions is in the form of "L." The corner where both arms meet is the center of gravity of the building. At this corner, the building was arranged as three floors. It is still used as a social facility (Kültür Portalı, 2019).

The Congress Building was built by the Governor of Sivas Mehmet Memduh Bey in 1892 as the Sivas High School, and the building served first as a high school during the Ottoman period and then as a sultani (lyceum) for long years. The Sivas Congress was held in this building on the 4th of September during the National Struggle Period, and the foundations of the Republic of Turkey were laid here. The founder of the Republic of Turkey, Gazi Mustafa Kemal ATATÜRK, and his friends were guests in this building for 108 days between 2 September–18 December 1919, and the building served as the "National Struggle Headquarters" during the most difficult days for the Turkish people. The school, which served as the Non-commissioned Officer School for a short time after the congress activities, was used as the "Sivas High School" from the first years of the Republic until the 1970s, and then as the "Congress High School" until 1981, and its ownership was transferred to the Ministry of Culture in 1984. After the repair, it started to serve on 19 December 1990 under the name of "Atatürk Congress and Ethnography Museum." It is still used as a museum (Kültür Portalı, 2019).

The Ulu Mosque (The Grand Mosque) is one of the oldest mosques in Anatolia. In the history of architecture in Anatolia, the mosque is an essential structure in the development of the idea of interior space. It is one of the rare examples of the Kufa-type mosque class that enters the courtyard from three directions and has a flat roof and a rectangular plan. It was built during a period when the idea of the dome had not developed yet. According to some scientists, it is also considered to be a work of the Danismendi period. Although the Danismendians were connected to the Seljuks in 1178, the structures built under their names date back to the end of the century. It is possible to count the Ulu Mosque (the Grand Mosque) of Sivas among the important works of the Danismendi period. According to the inscription that was revealed during the repair in 1955, it is understood that Kul Ahi was made to build it by Kızılarslan bin İbrahim during the period of Kutbettin Melikşah in 1196-1197 (Kültür Portalı 2019).

The building, called the Kurşunlu Turkish Bath since it was built by pouring lead into the iron connections on the main walls, was built in 1576 by Behram Pasha as a double Turkish bath from cut stones. There are separate sections for women and men in this structure, which bears the characteristics of classical Turkish baths of the Ottoman Period. It still serves as a Turkish bath (Kültür Portalı 2019).

All of the above-mentioned historic buildings can be inquired and analyzed within the GIS-based system presented within the scope of this study. On the other hand, many historic buildings indicated on the City Fortification Wall Map produced by Albert Gabriel approximately 100 years ago for Sivas city and on the City Plan Map produced by Arakel Badrik (Natanyan 2008) are still preserved nowadays and used effectively. On the contrary, six gates, through which it was possible to enter the city settlement center of that period, were marked on the city fortification wall map by Albert Gabriel. The gate names indicated on the map continue to exist as the location name nowadays. There are craftsmen who deal with handicrafts even today in the circle shown as the craft and trade area of the city in the city plan drawn by Arakel Badrik in 1915. While Sivas city center has continued its development for 100 years, it has also continued to be a city that bears the traces of history. Therefore, it is known as a city of culture and history.

While the oldest zoning plan of Sivas city center was created in 1937 in the historical archives of the Republic, the first orthophoto was produced in 1949. Within the scope of this study, data obtained from various archives between 1915 and 2018 were divided into 9 main periods and the growth direction in each period and its relationship with other periods were investigated. As a result, it has been observed that the investments specified in Table.2 directly affect the direction of development found in Table.3 and the residential areas in the immediate vicinity of the built public buildings are developing rapidly.

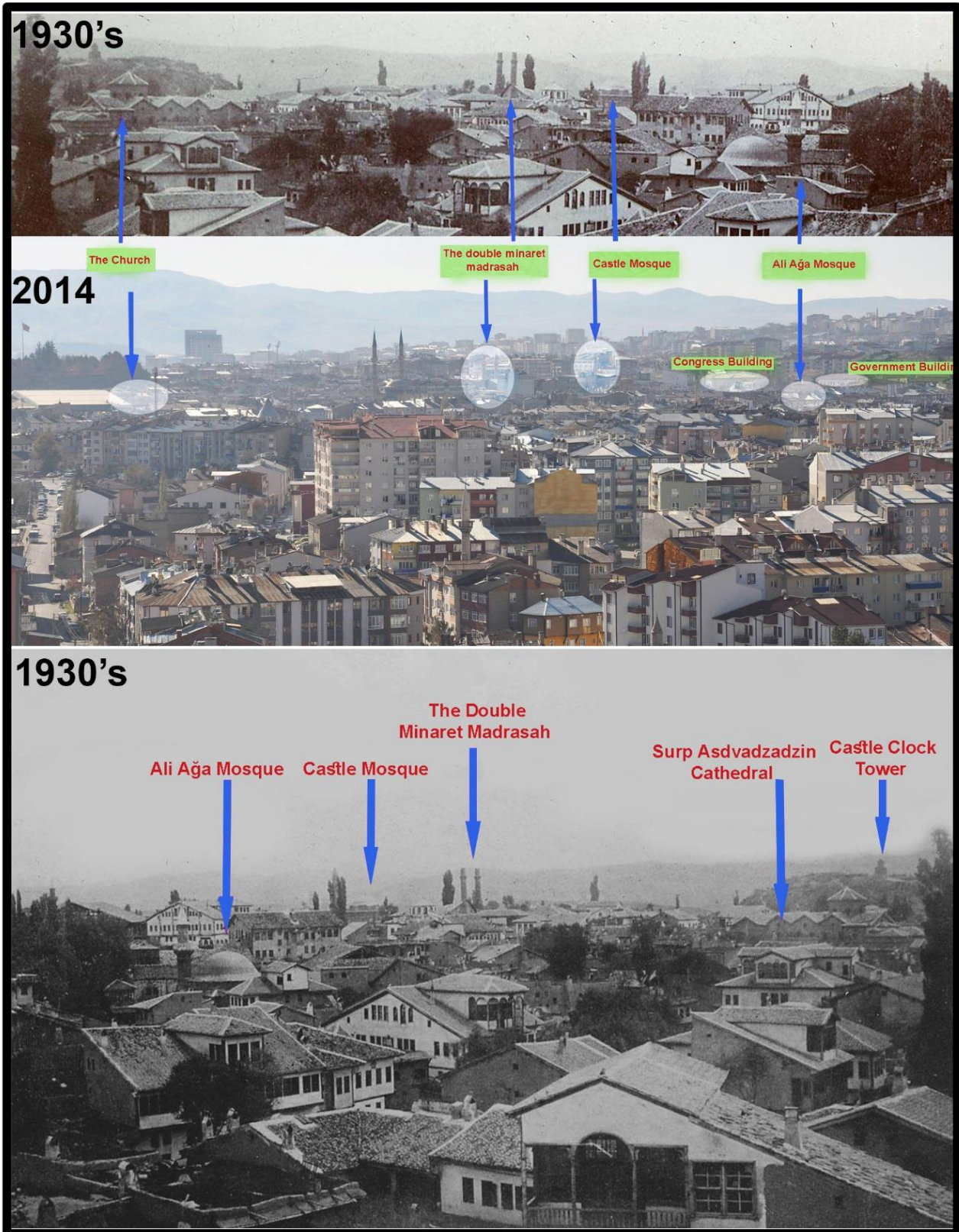


Figure 9. The appearance of some historic buildings at different dates (Adapted from Sivas Municipality archive)

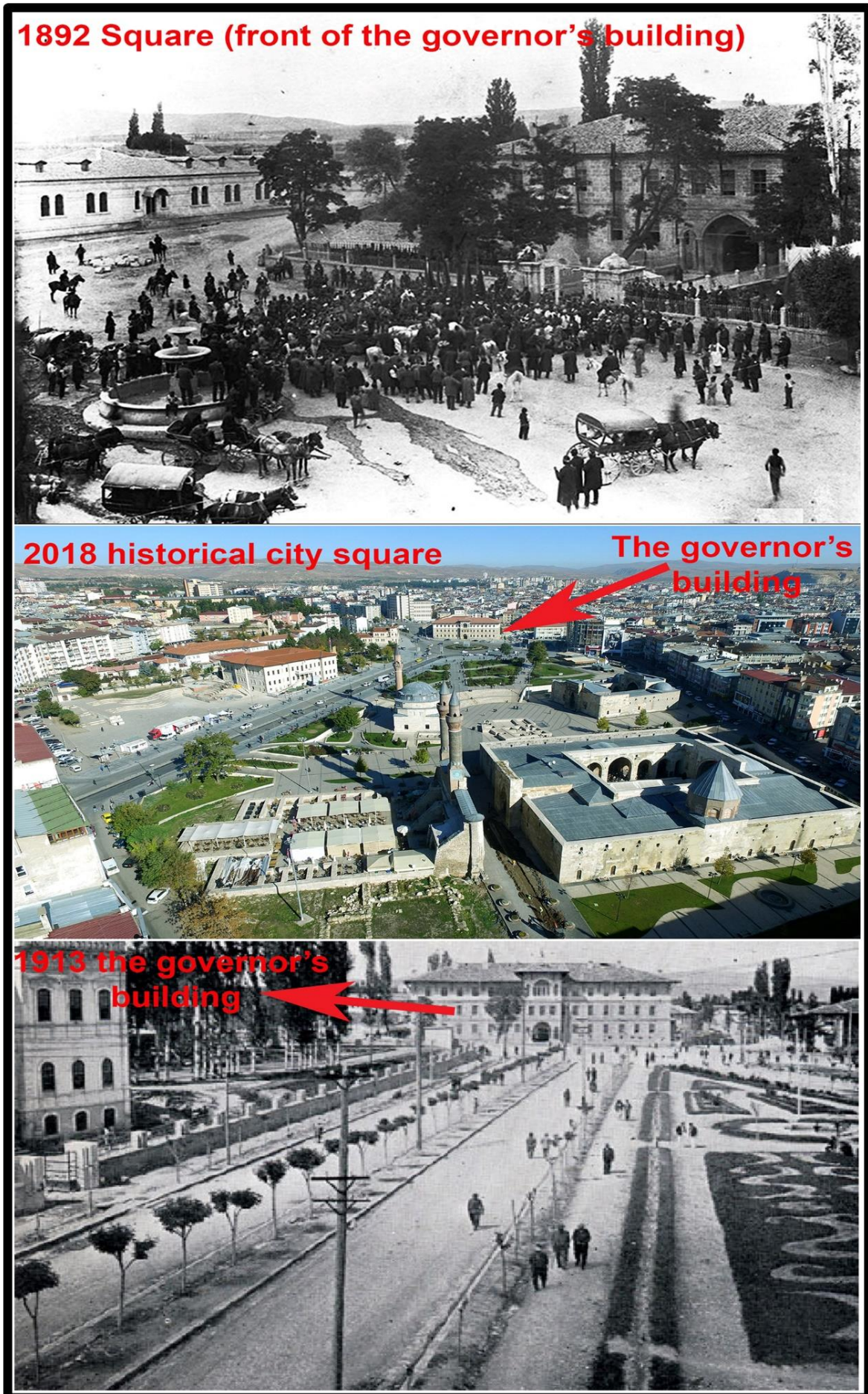
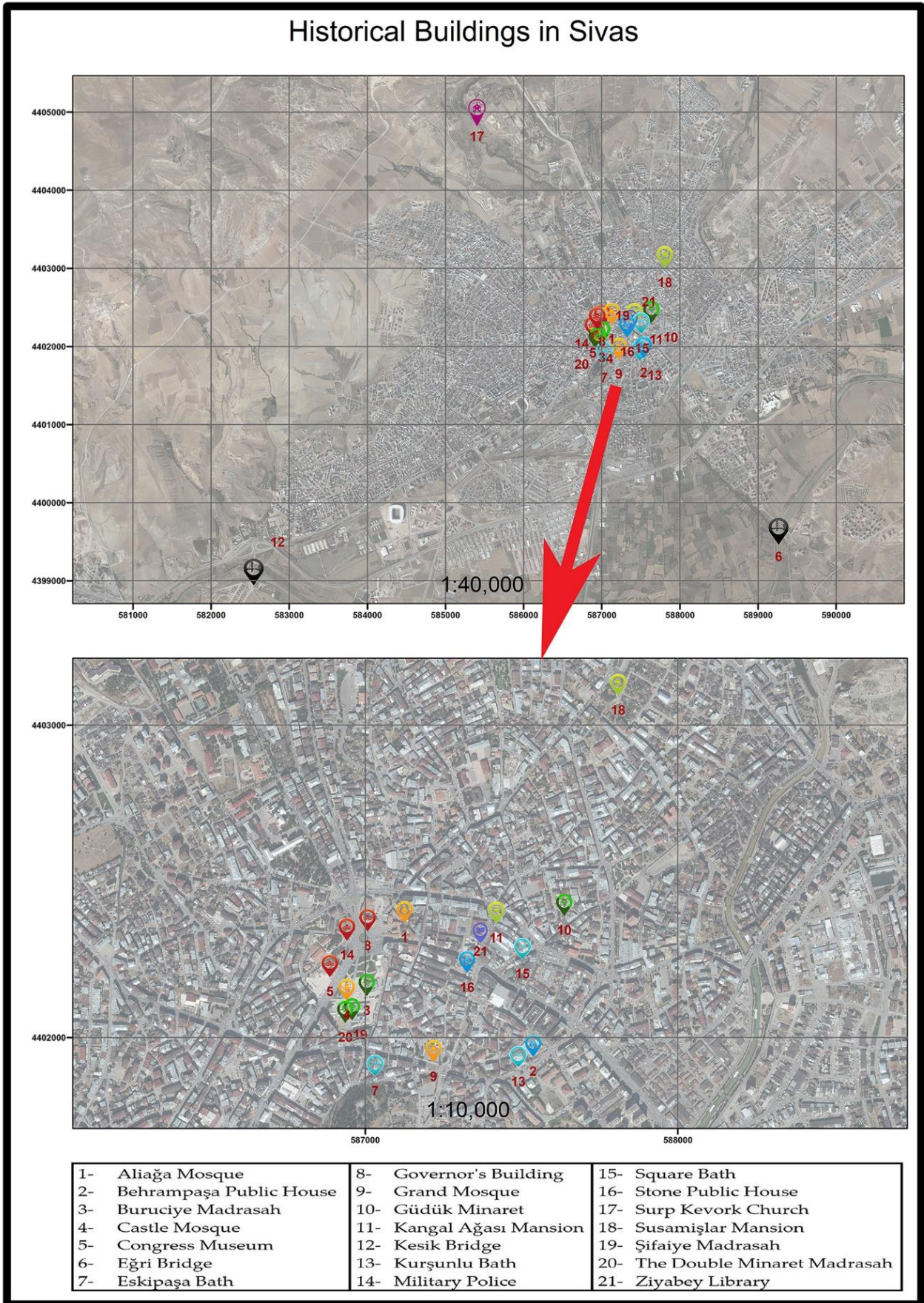


Figure 10. The historic city square (Adapted from Sivas Municipality archive)



**Figure 11.** The geographical location and distribution of historic buildings in Sivas

## 5. CONCLUSION

Urban information systems are indispensable for decision-makers in managing a city. In this process, GIS is used as an effective tool to create scenarios, make analyses, and make predictions about the future during the planning of the city by conducting interdisciplinary studies. Planning that is performed independently of GIS is very likely to fail.

Sivas is a significant center that has witnessed many critical times in history. Therefore, in the plans to be made, the city identity should be protected, historic buildings should be taken into consideration, if possible, green belts should be created by opening the surroundings of buildings, and the surroundings of buildings without the possibility for opening should be arranged in accordance with the texture of the building to be protected. The city skyline should be calculated well, and sunshine durations should be predicted. To this end, soil policies should be created. The connection, apart from the intersection points of intercity transit roads and urban roads, should be disconnected, and areas to be afforested should be planned in accordance with the microclimate of the city.

One of the most important phenomena ignored by the city administration bodies is disaster scenarios. Natural disasters can cause significant destruction; one natural disaster can trigger another one. Therefore, the crisis management plan of the city should be created, and how and in what areas the vital needs will be met for people to be able to continue their lives in case of natural disasters should be planned well.

Sivas city is an important center of Anatolia due to its location. The findings obtained within the scope of this study demonstrate that the city is not expanding in a regular direction. Due to these findings, planning decisions should be revised, and the future planning of the city should be performed by conducting multidisciplinary studies.

## ACKNOWLEDMENT

The authors would like to thank Sivas Municipality for providing the data needed in this study.

## REFERENCES

- Corbusier L (1933). La charte d'Athènes. Translation Book: March 2009, Translator: Dr. Ayda Yörükan, Yapı Kredi Publication.
- Erarslan A & Kolay İ A (2005). The ubaid and uruk phases of the proto-urban period of urbanisation process of the east and southeast anatolia regions (5000-3100 B.C.). *itüdergisi/b sosyal bilimler*, 2, 1, 80-86. (in Turkish)
- Gabriel A (1934). *Monuments Turcs D'Anatolie*, 2, 138 pages, Paris (in French)
- Göksel Ç & Dođru A Ö (2019). Analyzing the urbanization in the protection area of the Bosphorus. *International Journal of Engineering and Geosciences (IJEG)*, 4(2), 52-57. DOI: 10.26833/ijeg.446912
- Haaland C & Bosch C K (2015). Challenges and strategies for urban green-space planning in cities undergoing densification: A review. *Urban Forestry & Urban Greening*, 14(4), 760-771. DOI: 10.1016/j.ufug.2015.07.009
- İşcan F. and İlğaz A. (2017). Analysis of geographic/urban information system web presentations of local governments in Turkey. *International Journal of Engineering and Geosciences (IJEG)*, 2(3), 75-83. DOI: 10.26833/ijeg.317088
- Kasanko M, Barredo J I, Lavalle C, McCormick N, Demicheli L, Sagris V & Brezger A (2006). Are European cities becoming dispersed? A comparative analysis of 15 European urban areas. *Landscape and Urban Planning* 77, 111-130.
- Kızılelma Y, Karabulut M, Gürbüz M, Topuz M & Ceylan E (2013). An analysis of temporal changes of Nigde city and surrounding areas using remote sensing and GIS. *Journal of World of Turks*, 5(3), 21-34. (in Turkish)
- Kültür Portalı.. (2019). <https://www.kulturportali.gov.tr/arama/sivas> Accessed date: 17.02.2020
- Liu Y (2008). *Modeling urban development geographical information systems and cellular automata*. CRC Press, Taylor & Francis Group. 1. Edition. ISBN: 978-1-4200-5989-2
- Natanyan B (2008). *Sivas 1877. Bir zamanlar* Yayıncılık. İstanbul. ISBN 9756158074.
- Özyavuz, M. (2011). Examination of temporal changes of Tekirdağ city center with remote sensing. *Journal of Tekirdag Agricultural Faculty*, 8(1), 65-73. (in Turkish)
- Sağır N & Nacar F (2008). Determination of Urban Development with GIS in Osmaniye, one of our new provinces. 2. Remote Sensing and GIS Symposium, Kayseri (in Turkish)
- Selim S & Demir N (2019). Detection of ecological networks and connectivity with analyzing their effects on sustainable urban development. *International Journal of Engineering and Geosciences (IJEG)*, 4(2), 63-70. DOI: 10.26833/ijeg.443114
- Song Y (2005). Smart growth and urban development pattern: A comparative study. *International Regional Science Review*, 28(2), 239-265. DOI: 10.1177/0160017604273854
- Stalker P (2000). *Handbook of the World*. Oxford University Press. New York. ISBN: 978-0192800930
- Tekeli, I. (1997). *Urbanization, Ezcacıbaşı Art Encyclopedia*, 2, P.P. 993-996, Hürriyet Ofset (in Turkish)
- U N (2017). <https://www.unfpa.org/swop-2017> Accessed date: 17.02.2020

Uysal M M, Uysal M & Uysal C (2016). Monitoring urban growth using Sleuth model. 6.Uzaktan Algılama ve CBS Sempozyumu (UZAL-CBS), Adana, 66-75. (in Turkish)  
Yakar M & Doğan Y (2018). GIS and three-dimensional for cultural heritages.

International Journal of Engineering and Geosciences (IJEG), 3(2), 50-55.  
Yılmaz H., Reis S. and Atasoy M. (2007). Determination of Urban Development Process of New Provinces with GIS in Turkey: A Case Study in Aksaray Province. KTÜ. TMMOB National GIS Congress, Trabzon. (in Turkish)



© Author(s) 2021.

This work is distributed under <https://creativecommons.org/licenses/by-sa/4.0/>

***IJEG***  
***Volume 6 - Issue 1***

**ARTICLES**

**\*\* INVESTIGATION OF THE EFFECT OF URBANIZATION ON LAND SURFACE TEMPERATURE  
EXAMPLE OF BURSA**

Beyzanur Yamak, ZekeriyaYagci, Burhan Baha Bilgilioglu, Resul Comert 1

---

**\*\* AN INVESTIGATION OF THE PERFORMANCES OF POLARIMETRIC TARGET DECOMPOSITIONS  
USING GB-SAR IMAGING**

Sevket Demirci, Caner Ozdemir 9

---

**\*\* AUTOMATIC EXTRACTION OF TREES BY USING MULTIPLE RETURN PROPERTIES OF THE LIDAR  
POINT CLOUD**

Samed Ozdemir, Zeynep Akbulut, Fevzi Karsli, Hayrettin Acar 20

---

**\*\* DEVELOPING A MOBILE GIS APPLICATION RELATED TO THE COLLECTION OF LAND DATA IN  
SOIL MAPPING STUDIES**

Fatih Iscan, Erkan Guler 27

---

**\*\* INTELLIGENT MAPPING OF IRRIGATED AREAS FROM LANDSAT 8 IMAGES USING TRANSFER  
LEARNING**

Zouhair Benbahria , Imane Sebari, Hicham Hajji, Mohamed Faouzi Smiej 41

---

**\*\* AN INVESTIGATION OF URBAN DEVELOPMENT WITH GEOGRAPHICAL INFORMATION  
SYSTEMS: 100-YEAR CHANGE OF SIVAS CITY, TURKEY**

Sefa Sari, Tarık Türk 51

---